AD-A047 057 TEXAS UNIV AT AUSTIN DEPT OF MECHANICAL ENGINEERING F/G 13/7
A BASIS FOR NUMERICAL MODELING OF FLUID AMPLIFIERS
FEB 76 HEALEY, A. NICHOLSON, J. 162P
UNCLASSIFIED CONTRACT NO. DA-ARO-D-31-124-73-G115 ARO 10927.5-E N/L

1 OF 2
AD A047057

ARO 10927.5-E

# THE UNIVERSITY OF TEXAS AT AUSTIN

(12)

AD A047052

DISTRIBUTION STATEMENT A
Approved for public release;
Distribution Unlimited

## DEPARTMENT OF MECHANICAL ENGINEERING

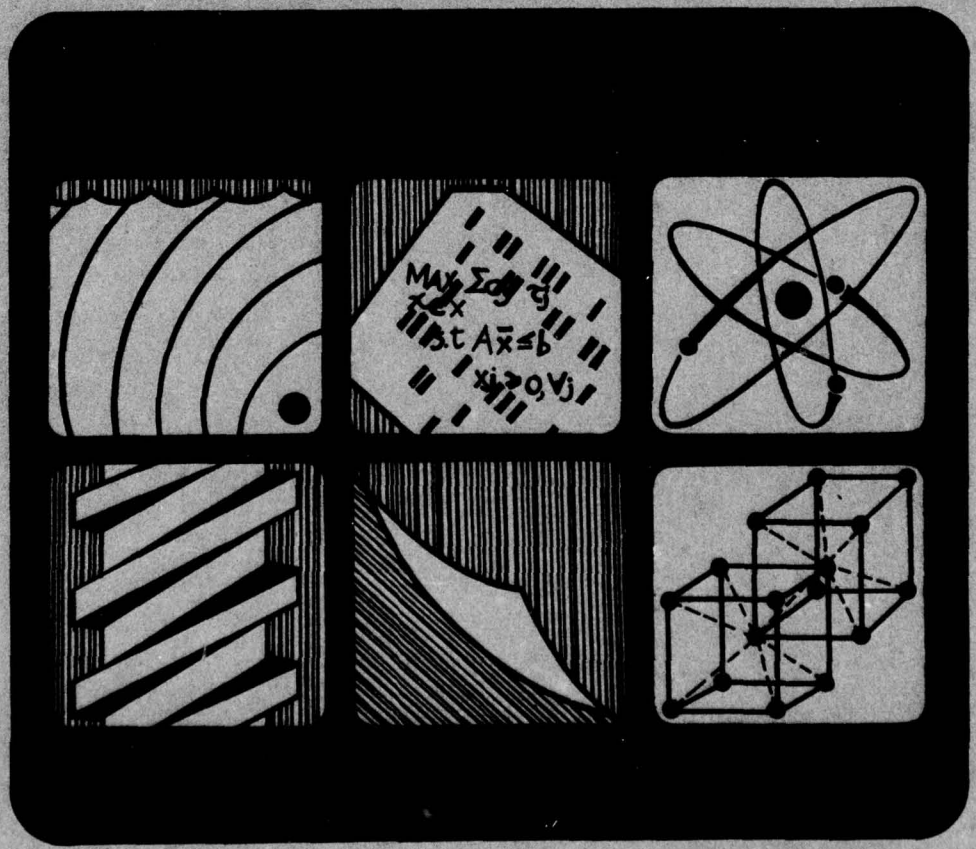

# A BASIS FOR NUMERICAL MODELING OF FLUID AMPLIFIERS

FINAL REPORT

Anthony J. Healey
James A. Nicholson

February 1976

U. S. ARMY RESEARCH OFFICE-DURHAM

Grant No. DA-ARO-D-31-124-73-G115

The University of Texas at Austin

Austin, Texas

Approved for Public Release: Distribution Unlimited

The findings of this report are not to be construed as an official Department of the Army position, unless so designated by other authorized documents.

Security Classification

**DOCUMENT CONTROL DATA - R & D**

*(Security classification of title, body of abstract and indexing annotation must be entered when the overall report is classified)*

| 1. ORIGINATING ACTIVITY (Corporate author) | 2a. REPORT SECURITY CLASSIFICATION |
|---|---|
| The University of Texas<br>Mechanical Engineering Department | 2b. GROUP |

3. REPORT TITLE

A Basis for Numerical Modeling of Fluid Amplifiers

4. DESCRIPTIVE NOTES (Type of report and inclusive dates)

Final Report 1973-1976

5. AUTHOR(S) (First name, middle initial, last name)

Anthony J. Healey
James A. Nicholson

| 6. REPORT DATE | 7a. TOTAL NO. OF PAGES | 7b. NO. OF REFS |
|---|---|---|
| February 1976 | 144 | 30 |

| 8a. CONTRACT OR GRANT NO. | 9a. ORIGINATOR'S REPORT NUMBER(S) |
|---|---|
| DA-ARO-D-31-124-73-G115 | |
| b. PROJECT NO. | |
| c. | 9b. OTHER REPORT NO(S) (Any other numbers that may be assigned this report) |
| d. | |

10. DISTRIBUTION STATEMENT

Distribution of this document is unlimited.

| 11. SUPPLEMENTARY NOTES | 12. SPONSORING MILITARY ACTIVITY |
|---|---|
| | |

13. ABSTRACT

Laminar fluid flow in a simplified fluidic amplifier is analyzed using finite difference numerical techniques. Numerical solutions to the two dimensional incompressible Navier-Stokes equations are obtained in terms of stream function and vorticity. These solutions are presented as contour plots of lines of constant stream function. The effect of various flow parameters, such as Reynolds number, outlet port loading, and deflection of the power jet are examined. Finite difference solutions are also obtained for the pressure distribution. The problems associated with obtaining accurate numerical pressure solutions are discussed in detail. In particular, the problems associated with an inconsistent formulation of this Neumann problem are described. A large-scale laminar flow amplifier was designed and constructed so that the geometry matched that of the numerical simulation. Dye was injected into water flowing in the amplifier and streamline photographs were obtained. Good agreement existed between the photographs and the numerically predicted streamlines. Extensions of the model aimed at producing a working tool for use in design of fluidic amplifiers are suggested.

DD FORM 1 NOV 68 1473 REPLACES DD FORM 1473, 1 JAN 64, WHICH IS OBSOLETE FOR ARMY USE.

Security Classification

| 14. KEY WORDS | LINK A | | LINK B | | LINK C | |
|---|---|---|---|---|---|---|
| | ROLE | WT | ROLE | WT | ROLE | WT |
| Numerical Methods | | | | | | |
| Laminar Flow | | | | | | |
| Fluid Flow | | | | | | |
| Fluid Amplifiers | | | | | | |
| Simulation | | | | | | |
| Jet | | | | | | |
| Internal Flow | | | | | | |

## ACKNOWLEDGEMENTS

The authors wish to thank Dr. W. Oberkampf of the Department of Mechanical Engineering at the University of Texas for his work and advice on the numerical solution procedures. We also wish to thank Mr. James Murray and Dr. Charles Harmon for their long and patient cooperation with us in the preparation of this document and for their support of this research program under Grant No. DA-ARO-D-31-124-73-G115.

## ABSTRACT

Laminar fluid flow in a simplified fluidic amplifier is analyzed using finite difference numerical techniques. Numerical solutions to the two dimensional incompressible Navier-Stokes equations are obtained in terms of stream function and vorticity. These solutions are presented as contour plots of lines of constant stream function. The effect of various flow parameters, such as Reynolds number, outlet port loading, and deflection of the power jet are examined. Finite difference solutions are also obtained for the pressure distribution. The problems associated with obtaining accurate numerical pressure solutions are discussed in detail. In particular, the problems associated with an inconsistent formulation of this Neumann problem are described. A large-scale laminar flow amplifier was designed and constructed so that the geometry matched that of the numerical simulation. Dye was injected into water flowing in the amplifier and streamline photographs were obtained. Good agreement existed between the photographs and the numerically predicted streamlines. Extensions of the model aimed at producing a working tool for use in design of fluidic amplifiers are suggested.

## EXECUTIVE SUMMARY

The basic components of a beam deflection fluid jet amplifier are a power jet which issues from a nozzle and impinges on symmetrically placed recovery passages, and control passages which act on the side of the power jet so as to give the resulting stream a lateral deflection relative to the line of symmetry. The recent Fluidic State of the Art Symposium* provides excellent background for the reader who is unfamiliar with the field.

### Static Output Characteristics

Resulting from early work under this contract it was found that when a power jet impinges on a single receiver passage, the recovery pressure and flow at the output port of the receiver could be calculated only when receiver loading allowed significant through flow of fluid. A method involving the use of moving "cowl-streamlines" with a lumped control volume model assuming inviscid flow in the control volume region was proposed as an improved and viable way to predict output performance.

This work was later extended to the case of a jet interacting with multiple receivers and by careful selection of the location of the cowl-streamlines, again it was possible to predict the output recovery in the receiver system. Although a wide range of jet flow Reynolds Numbers and receiver geometries were not investigated, the predictive power of the model was adequate (less than 10% error) for the cases considered.

### Amplifier Jet-Vent Dynamics

Moving to the dynamics of a complete amplifier, early studies had shown that the bandwidth of a beam-deflection amplifier was limited by the

* Fluidic State of the Art Symposium--Harry Diamond Laboratories, September 1974.

inertia of the side vent fluid. One of the unknown quantities in the development of theoretical models for predicting bandwidth was the coefficient relating to the division of the power jet in the side vent areas to main jet deflection.

This coefficient depends on output loading and receiver configuration. Thus utilizing the work of the early studies on recovery and spillover characteristics, a lumped system dynamic model including jet transport delay effects was formulated. The results of the work showed an almost quadratic reduction in bandwidth as the side vent lengths were increased but only compared accurately with experimentally measured bandwidths for short side vents. Higher frequency resonances were seen and were attributed to jet lateral dynamic modes in which the apparent signal transmission speed in a turbulent jet was found to travel at nearly one-fourth of the power jet nozzle flow velocity.

Numerical Models for Laminar Interaction Regions

Finally, to investigate the feasibility of using new efficient numerical codes for the solution of the laminar flow field equations, a study was undertaken of a non-vented amplifier without control jet action. The equations of laminar, two dimensional, incompressible flow were solved using finite difference methods. The solutions for distribution of stream function values showed good agreement with experimentally observed flow patterns.

Numerical methods were compared for calculating internal pressure distributions with asymmetric loading at the receiver ports so that output port pressure-flow characteristics could be predicted. The accuracy of the pressure distribution simulation was not satisfactory and indicated that problems can

arise because of the need to solve a Poisson type differential equation with Neumann boundary conditions. An inconsistency in the equations can be found under some conditions and numerical errors can reduce the final accuracy in the predicted pressure-flow relationships at the amplifier ports.

The details of the numerical modeling research are presented in this final technical report.

## DEGREES AWARDED WITH SUPPORT OR PARTIAL SUPPORT UNDER THE CONTRACT

### Master's Degrees

Mr. W. J. Reynolds. "Static Output Characteristics of a Beam Deflection Fluid Amplifier", M.S. thesis, The University of Texas at Austin, December, 1972.

Mr. E. M. Shipp, "Vent Length Effects on a Proportional Fluid Amplifier." M.S. thesis, The University of Texas at Austin, August, 1973.

Mr. S. Craig, "An Analytical-Empirical Approach to Signal Recovery in Fluid Amplifier Receivers" M.S. thesis, The University of Texas at Austin, May, 1974.

Mr. J. S. Corbin, "Linear Transients in Pneumatic Transmission Systems Using State Variable Methods", M.S. thesis, The University of Texas at Austin, May, 1975.

### Doctoral Degrees

Mr. J. A. Nicholson, "A Basis for Numerical Modelling of Fluid Amplifiers", Ph.D. dissertation, The University of Texas at Austin, December, 1975.

## LISTING OF PAPERS PUBLISHED AND REPORTS ISSUED

Reports:

"Vent Length Effects on a Proportional Fluid Amplifier" Technical Report, September, 1973.

"A Basis for Computer Modelling of Internal Flows in Laminar Fluid Amplifiers" Technical Report, September, 1973.

"An Analytical-Empirical Approach to Signal Recovery in Fluid Amplifier Receivers", Technical Report, May, 1974.

Papers

Healey, A. J. "Experimental Study of Spillover Flow from a Single Fluid Amplifier Receiver" A.S.M.E. Paper No. 73-WA/FLCS-6 Presented at the 1973 Winter Annual Meeting. Also published in Fluidics Quarterly v. n. pp.

Healey, A. J., "Jet Deflection Proportional Amplifier" Fluidic State of the Art Symposium U.S. Harry Diamond Laboratories, Vol. I pp 269-351 1974.

Nicholson, J. A., Oberkampf, W. O., Healey, A. J., "Numerical Simulation of Internal Laminar Flows in Fluid Amplifiers"

Proceedings of the International Colloquium on Field Simulation, Polytechnic of Central London, London, September, 1974, pp

Healey, A. J. "Pressure-Flow Characteristics of a Single Fluid Amplifier Receiver with Offset, Bounded Jet" Trans. A.S.M.E., Journal of Dynamic Systems, Measurement and Control v. n. June, 1973, p

TABLE OF CONTENTS


| | | Page |
|---|---|---|
| ACKNOWLEDGEMENTS | | |
| ABSTRACT | | |
| EXECUTIVE SUMMARY | | |
| DEGREES | | |
| PUBLICATIONS | | |
| TABLE OF CONTENTS | | |
| LIST OF TABLES | | |
| LIST OF FIGURES | | |
| I. | INTRODUCTION | 1 |
| | A. Beam Deflection Proportional Amplifiers and Characteristic Curves | 2 |
| | B. General Aims of the Study | 8 |
| | C. Method of Approach | 9 |
| II. | DEVELOPMENT OF THE NUMERICAL MODEL | 10 |
| | A. Continuum Equations | 10 |
| | B. Boundary Conditions | 17 |
| | C. Finite Difference Solution for the Flow Field | 21 |
| | D. Method of Solution for the Pressure Field | 35 |
| III. | EXPERIMENTAL APPARATUS AND PROCEDURE | 48 |
| | A. Overview | 48 |
| | B. Model | 49 |
| | C. Fluid Supply System | 56 |
| | D. Instrumentation | 58 |

Page

E. Photographic Equipment . . . . . 64

F. Comments on Experimental Procedure . . . . . 65

G. Sample Result . . . . . 66

IV. DISCUSSION OF RESULTS . . . . . 68

A. Flow Field Results for the Undeflected Jet . . . . . 68

B. Flow Field Results for the Deflected Jet . . . . . 89

C. Pressure Field Results . . . . . 91

D. Discussion of Accuracy of Pressure Solutions . . . . 95

E. Characteristic Design Curves . . . . . 109

F. Edgetone Oscillations . . . . . 112

G. Discussion of the Numerical Model . . . . . 116

V. SUMMARY, CONCLUSIONS AND RECOMMENDATIONS . . . . . 126

A. Summary . . . . . 126

B. Conclusions . . . . . 129

C. Recommendations . . . . . 131

APPENDIX . . . . . 134

BIBLIOGRAPHY . . . . . 144

VITA

LIST OF TABLES


| Table | | Page |
|---|---|---|
| 2.1 | Non-Dimensional Variables . . . . . | 12 |
| 4.1 | Stream Function Values . . . . . | 69 |
| 4.2 | Pressure Solution Details . . . . . | 98 |
| A.1 | Difference Expressions for $\delta P/\delta x$, $\delta P/\delta y$, and $s_{i,j}$ . . . | 135 |

LIST OF FIGURES


| Figure | | Page |
|---|---|---|
| 1.1 | Typical Vented Beam Deflection Amplifier | 3 |
| 1.2 | Typical Input Characteristic Curve | 6 |
| 1.3 | Typical Single-Sided Pressure Gain Characteristic Curve | 6 |
| 1.4 | Typical Differential Pressure Gain Characteristic Curve | 7 |
| 1.5 | Typical Output Characteristic Curve | 7 |
| 2.1 | Amplifier Geometry | 16 |
| 2.2 | Amplifier Inlet Geometry | 19 |
| 2.3 | Grid Notation | 27 |
| 2.4 | Grid Configurations for Concave Corners and Receiver Walls | 39 |
| 3.1 | Experimental Equipment | 50 |
| 3.2 | Plan View of Experimental Model | 51 |
| 3.3 | Details of Experimental Equipment | 55 |
| 3.4 | Flow Meter Calibration Curves | 60 |
| 3.5 | Typical Flow Visualization | 67 |
| 4.1 | Stream Function Distribution Re = 1 $Q_1 = 0.5\ Q_s$ $\phi = 0°$ | 69 |
| 4.2 | The Effect of Reynolds Number on the Flow Field | 71 |
| 4.3 | Predicted Velocity Profiles in the Cavity Region | 74 |
| 4.4 | Centerline Velocity Decay | 76 |
| 4.5 | Comparison of Numerical and Experimental Flows Re = 100 $Q_1 = 0.5\ Q_s$ $\phi = 0°$ | 78 |
| 4.6 | Individual Streamlines for Re = 100 | 79 |

| Figure | | Page |
|---|---|---|
| 4.7 | Comparison of Numerical and Experimental Flows Re = 20 $Q_1 = 0.5\ Q_s$ $\phi = 0°$ | 81 |
| 4.8 | Flow Fields with Unequal Outflows | 83 |
| 4.9 | Comparison of Numerical and Experimental Flows Re = 100 $Q_1 = 1.0\ Q_s$ $\phi = 0°$ | 85 |
| 4.10 | Comparison Between Symmetric and Blocked Flows with Re = 100 | 87 |
| 4.11 | Deflected Flows with Re = 100 | 90 |
| 4.12 | Pressure Results | 92 |
| 4.13 | Pressure Results | 94 |
| 4.14 | Pressure Results for Deflected Flows | 96 |
| 4.15 | Typical Control Volume for Integral Pressure Calculations | 100 |
| 4.16 | Comparison of Compensated and Non-Compensated Pressure Solutions | 107 |
| 4.17 | Outlet Characteristic Curve | 111 |
| 4.18 | Edgetone Oscillation | 113 |
| 4.19 | Effect of Grid Spacing on Flow Solutions | 117 |
| 4.20 | Effect of Various Boundary Conditions on Flow Solutions | 119 |

# CHAPTER I

## INTRODUCTION

The proportional amplifier is one of the basic components of many fluidic systems. Since the early 1960's a great deal of work has been done modifying and optimizing the design of such amplifiers, understanding the fluid mechanics involved, and developing techniques for the use of amplifiers in control circuits.

As with most engineering components fluidic devices have both advantages and disadvantages [10,16]. One important advantage is the ability of properly designed fluidic systems to function in harsh environments, especially in comparison to electronic systems designed to perform similar functions. Often having no moving mechanical parts, fluidic devices are resistant to failure due to mechanical shock or vibration. They can be designed with low cost to withstand high temperatures or high radiation fields.

Unfortunately, there are attendant disadvantages. Relatively low speed of operation compared to electronics results from both the relatively slow acoustic propagation speed in the fluid and the time required for fluid movement. The tendency of fluid flows to become unstable generates turbulent fields. This turbulence gives rise to high noise content in the sensing and control signals. Also, amplifier gains and input impedances are low compared to corresponding electronic devices.

Perhaps a more subtle problem facing the development of fluidics is the lack of a completely adequate model for predicting the performance of components. The characteristics and usefulness of all fluidic devices depend on the interaction of one or more fluid jets. Most modeling techniques to date have relied on assumptions of flow conditions for these confined jets and have met with success only in specific cases. The search for a more general way of modeling the internal fluid flow interactions in fluid amplifiers has been the motivation for this work.

## A. Beam Deflection Proportional Amplifiers and Characteristic Curves

Consider in particular a beam deflection proportional amplifier. Although the fluid mechanics involved in such a device are complex, the basic idea is very simple. A typical amplifier is shown in Fig. 1.1. The differential signal which is to be amplified, either a pressure or a flow, is established as an input between the control ports.

A high energy supply jet (typically having ten times the stagnation pressure level of the control flows) enters the amplifier through the power nozzle. It is deflected by the differential pressure and momentum of the control flows. This main flow continues across the amplifier cavity at some angle to the cavity centerline and impinges on the receivers. The vents, receivers, and center dump collect varying amounts of flow and energy depending on the degree of deflection of the power jet. Thus, a differential

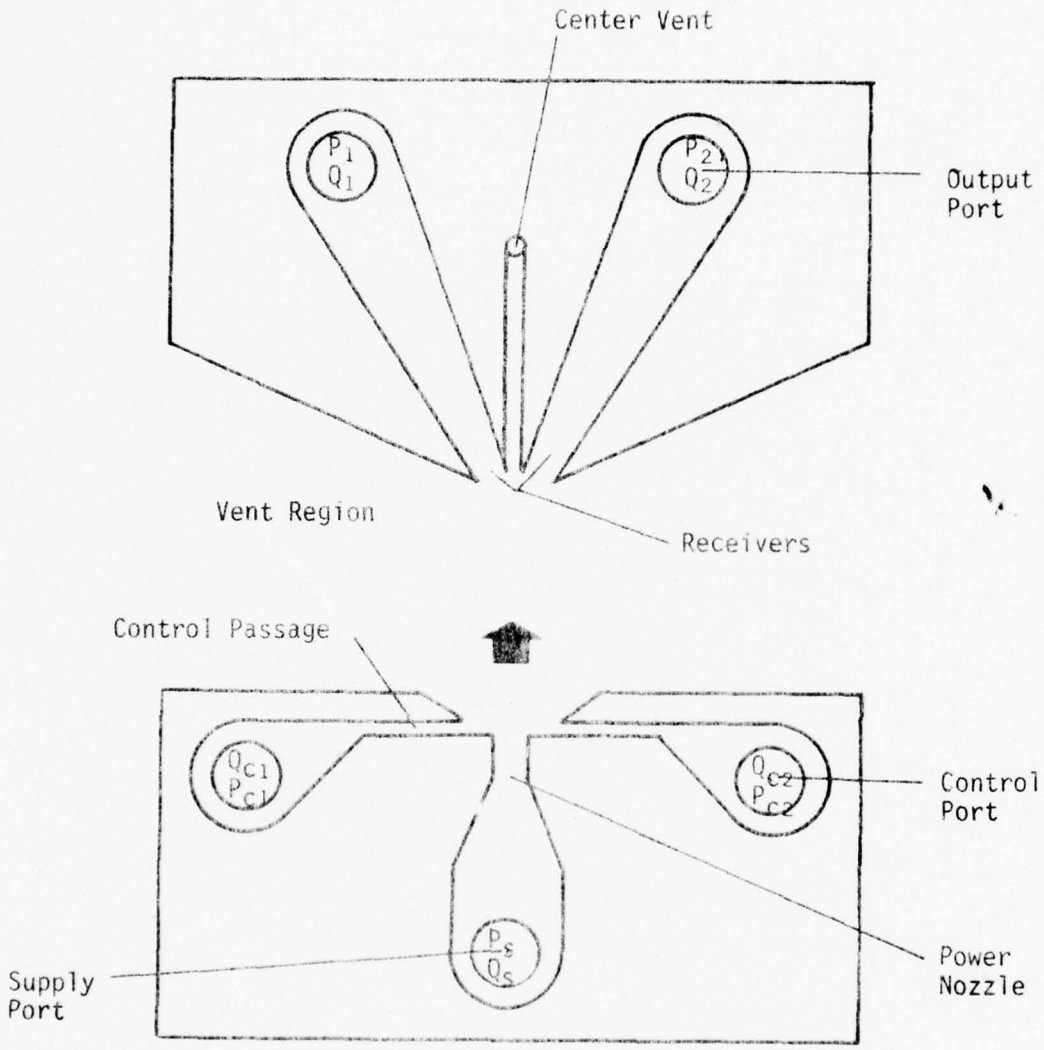


Figure 1.1. Typical Vented Beam Deflection Amplifier

pressure is produced at the receiver outlets. This differential is directly related to the control pressure differential but of larger magnitude; that is, the original differential signal has been amplified.

A large variety of fluid flow phenomena are involved in this process. Consider the main jet as it flows across the amplifier. To begin with, the jet flow can be either laminar or turbulent. As the jet leaves the power nozzle a velocity profile begins to develop due to the viscous or turbulent shear on the flow. Quickly this profile is modified by interaction with the control flows. Further, the geometry in the control region will effect the developing profile. Of particular interest are the positioning of the control nozzles and the amplifier aspect ratio, which is the ratio of the power nozzle width to the amplifier depth. Once in the cavity region the jet is acted on by shear forces and by the recirculation flow from the amplifier vents. As it impinges on the receivers the jet profile is destroyed by stagnation against the wall and by division of the flow between the receivers, vents, and center dump. This flow division is extremely important but little understood.

The staging and design of beam deflection amplifier circuits are described in detail by Belsterling [3]. This procedure will not be described here except to point out that it is necessary to know the "characteristic" curves of a given amplifier. These curves graphically describe how the amplifier will respond to various

control pressure differentials and what the relationship is between both the control flows and pressures and the output flows and pressures.

For example, a typical static input characteristic curve for one control port of an amplifier is shown in Fig. 1.2. A similar curve would exist for the other port. The curve relates the flow through the control port to the pressure at the port.

The influence of the control pressure differential on the receiver output pressures is commonly shown in one of two ways. The output pressure for one of the receivers can be plotted as a function of the control pressure differential, as in Fig. 1.3. Alternatively, the pressure differential at the receivers can be shown as a function of the control pressure differential, as in Fig. 1.4.

The output characteristics for the amplifier are typically plotted as shown in Fig. 1.5. Here the flow in one receiver is plotted as a function of the output pressure of that receiver. Separate curves are given for various values of the control pressure differential. All of the above characteristic curves are obtained experimentally as explained by Belsterling [3].

While the particular amplifier shown in Fig. 1.1 is vented, other amplifiers are also used in which the side vents are closed. This eliminates the need for a separate drain to handle the vent flows. Naturally, non-vented amplifiers are only used when the loading at the receivers allows continuous through flow. Otherwise the flow in the power jet would be stopped.

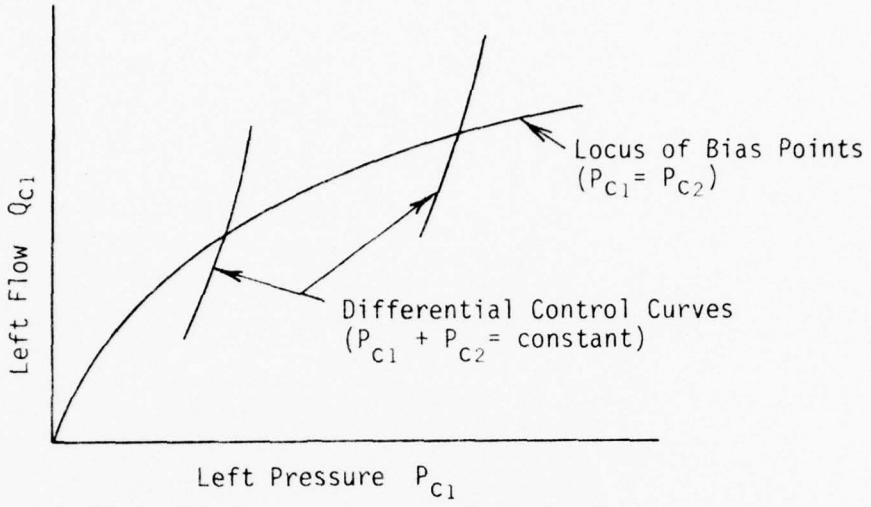


Figure 1.2. Typical Input Characteristic Curve

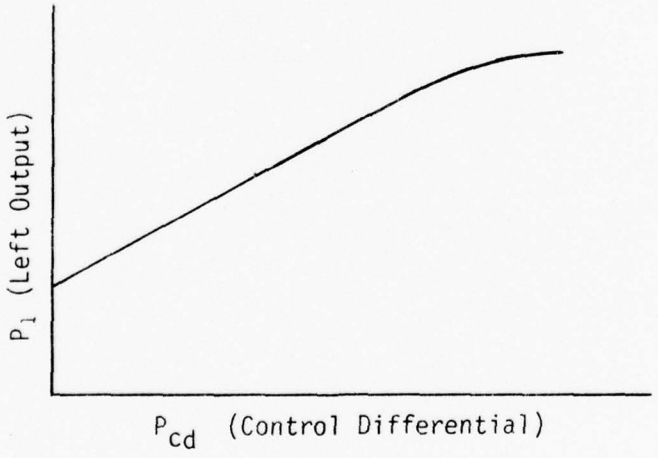


Figure 1.3. Typical Single-sided Pressure Gain Characteristic Curve

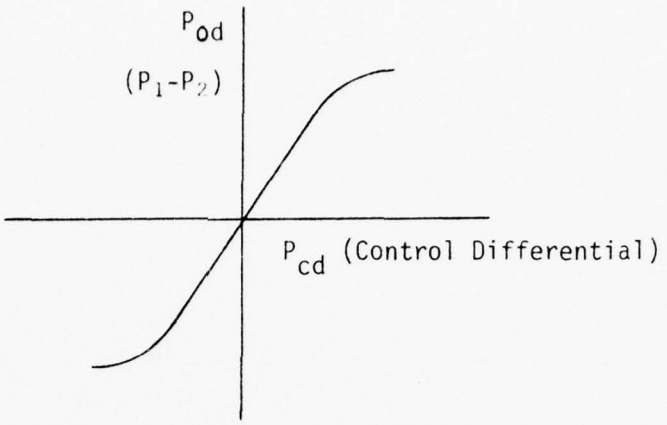


Figure 1.4. Typical Differential Pressure Gain Characteristic Curve

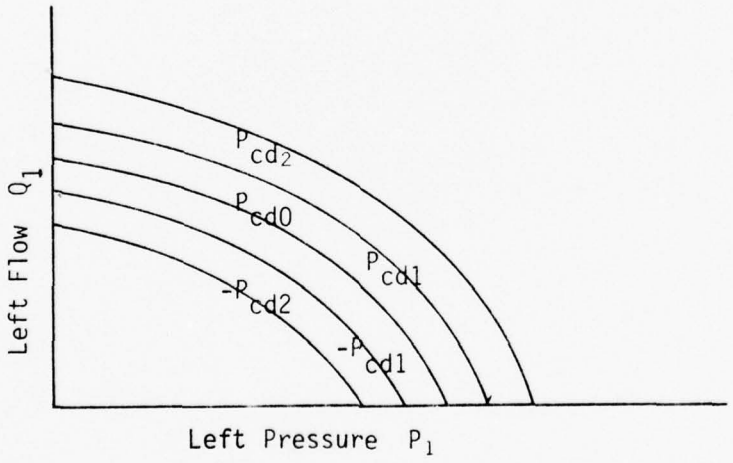


Figure 1.5. Typical Output Characteristic Curve

B. General Aims of the Study

Optimization of design and performance characteristics has been accomplished in the past by trial and error experimental processes coupled with some assistance from limited theoretical models. These models have employed control volume analyses [11]. The major drawback with these models is the assumptions which must be made as to velocity and pressure distributions within the internal field of flow.

The aim of this study was to examine the problems and investigate the feasibility of using finite difference techniques for predicting the internal flow and performance characteristics of a simplified beam deflection amplifier. With these techniques many of the assumptions of the control volume analyses can be avoided.

The choice of the particular amplifier to be modeled was governed by several considerations. Because of the improved signal to noise ratios in laminar amplifiers [13], a laminar flow device was chosen for the study. Also, in order to keep the scope of the investigation within bounds, a simplified device was chosen which resembles a non-vented amplifier having no control passages. The reason for eliminating control passage effects at this stage was to concentrate on the interactions between the power-jet, the receivers, and the side circulation regions of the device. The effects of jet deflection were modeled here by a simple angular deflection of the power jet relative to the device centerline. It was felt that

control flow effects could be included later. Finally, a high aspect ratio has been chosen for the amplifier in this investigation. While this may not be the best situation practically for fluid amplifiers, it does allow the assumption for now of a two dimensional flow field. Extensions of the work to three dimensional flow could be made in principle.

C. Method of Approach

The study divides into three major parts. First, the stream function and vorticity transport equations are solved using finite difference techniques. Basically the model assumes that the amplifier flow is a laminar, two dimensional, incompressible, viscous flow. Second, based on the calculated flows finite difference solutions are obtained for the pressure distribution in the amplifier. Finally, experimental flow visualizations are obtained through dye injection into water flowing in a large scale laminar amplifier model. These visualizations provide qualitative experimental comparisons for evaluation of the numerically predicted flow patterns.

# C H A P T E R  I I

## DEVELOPMENT OF THE NUMERICAL MODEL

This chapter begins with presentation of the governing set of partial differential equations for the fluid flow being considered. These continuum equations divide naturally into two separate, but related, systems of finite difference equations; i.e. the flow field equations and the pressure field equations. Since analytical solutions for these problems are not feasible, numerical solutions using finite difference techniques were sought. Appropriate differencing, boundary conditions, method of solution, and convergence criterion will be presented for both systems. In addition, for the pressure equation the problem of inconsistency will be examined.

### A. Continuum Equations

The physical process being modeled is that of a viscous fluid moving through a confined flow region. Since Mach numbers are small, the flow can be assumed incompressible and with the restriction to suitably low flow velocities the assumption of laminar flow in all regions may be made. Further, it is assumed that the fluid properties are invariant and that body forces are negligible. Finally, it is assumed that a two dimensional model will give a reasonable representation of the physical process.

Under these assumptions the motion of the fluid is described by the following form of the Navier-Stokes and continuity equations [25]. In terms of the Cartesian coordinates x and y and time t, these equations are

$$\frac{\partial u}{\partial t} + u\frac{\partial u}{\partial x} + v\frac{\partial u}{\partial y} = -\frac{1}{\rho}\frac{\partial P}{\partial x} + \nu\left(\frac{\partial^2 u}{\partial x^2} + \frac{\partial^2 u}{\partial y^2}\right) \tag{2.1}$$

$$\frac{\partial v}{\partial t} + u\frac{\partial v}{\partial x} + v\frac{\partial v}{\partial y} = -\frac{1}{\rho}\frac{\partial P}{\partial y} + \nu\left(\frac{\partial^2 v}{\partial x^2} + \frac{\partial^2 v}{\partial y^2}\right) \tag{2.2}$$

$$\frac{\partial u}{\partial x} + \frac{\partial v}{\partial y} = 0 \tag{2.3}$$

where u and v are the x and y velocities, respectively, P is the pressure, and $\rho$ and $\nu$ are the fluid properties density and kinematic viscosity, respectively.

In order to simplify Eqs.(2.1), (2.2), and (2.3) for our purposes here, it is convenient to make a change of variables and to eliminate the pressure from the resulting set of equations. In addition, throughout this work the variables will be nondimensionalized using the average inflow velocity U, the width b of the inlet, and/or the quantity $\rho U^2$ (see Table 2.1). The variable transformation introduces the variables stream function $\psi$ and vorticity $\zeta$ which are defined by the relations

$$\zeta = \frac{\partial u}{\partial y} - \frac{\partial v}{\partial x} \tag{2.4}$$

and

$$u = \frac{\partial \psi}{\partial y}, \qquad v = -\frac{\partial \psi}{\partial x}. \tag{2.5}$$

Table 2.1. Non-Dimensional Variables

| Dimensional Variable | Dimensionless Ratio |
|---|---|
| $\hat{u}$ | $u = \hat{u}/U$ |
| $\hat{v}$ | $v = \hat{v}/U$ |
| $\hat{x}$ | $x = \hat{x}/b$ |
| $\hat{y}$ | $y = \hat{y}/b$ |
| $\hat{P}$ | $P = \hat{P}/\rho U^2$ |
| $\hat{\zeta}$ | $\zeta = \hat{\zeta}/(U/b)$ |
| $\hat{\psi}$ | $\psi = \hat{\psi}/(Ub)$ |

Finally, the pressure is eliminated by differentiating Eq.(2.1) with respect to y and Eq.(2.2) with respect to x. Upon subtraction of the two resulting equations the derivatives of pressure cancel and the vorticity transport equation is obtained. One can rearrange this equation into conservative form [20] and obtain

$$\frac{\partial \zeta}{\partial t} = - \frac{\partial (u\zeta)}{\partial x} - \frac{\partial (v\zeta)}{\partial y} + \frac{1}{Re} \left[ \frac{\partial^2 \zeta}{\partial x^2} + \frac{\partial^2 \zeta}{\partial y^2} \right] \tag{2.6}$$

(advection terms) (diffusion terms)

$$\zeta = \frac{\partial^2 \psi}{\partial x^2} + \frac{\partial^2 \psi}{\partial y^2} \tag{2.7}$$

where the Reynolds number, Re, is $Ub/\nu$.

With application of suitable boundary conditions this system of coupled partial differential equations defines the flow field. Solution for the flow field using these equations is simplified compared to use of the original set because the pressure terms have been eliminated.

When a pressure field solution is desired, it must be reconstructed from the flow field solution. Pressure distributions can be obtained by solution of a Poisson type partial differential equation which is also derived from Eq.(2.1) and Eq.(2.2) [20]. Differentiating Eq.(2.1) with respect to x, differentiating Eq.(2.2) with respect to y, adding, eliminating terms through use of continuity, and transforming variables results in the elliptic equation

$$\frac{\partial^2 p}{\partial x^2} + \frac{\partial^2 p}{\partial y^2} = 2\left[\frac{\partial^2 \psi}{\partial x^2}\frac{\partial^2 \psi}{\partial y^2} - \left(\frac{\partial^2 \psi}{\partial x \partial y}\right)^2\right] \tag{2.8}$$

It should be emphasized that, although the equations are separate, the pressure field equation is dependent on having a solution for the flow field. This dependency is reflected both in the derivatives on the right-hand side of Eq.(2.8) and in the boundary conditions for Eq.(2.8), which will be presented shortly.

Solution of Eq.(2.8) with appropriate boundary conditions provides the pressure distribution over the entire region of interest. Alternatively, the pressure at particular points in a region can be obtained by integration of the total derivative of pressure along a given path [18]. If the pressure is known at point A, then at point B

$$P_B = P_A + \int_A^B \left( \frac{\partial P}{\partial x} dx + \frac{\partial P}{\partial y} dy \right) \quad . \tag{2.9}$$

The necessary pressure gradients are obtained from the flow field solution, through expressions similar to Eqs.(2.1) and (2.2), again illustrating the dependence of the pressure field on the flow field. This approach to the pressure problem is popular, for example, in lift and drag calculations for a surface where only the pressure values on the surface itself are needed [14,28].

Although both approaches for obtaining pressure values would give identical results in the continuum, they could have significant differences in the discrete case. These will be discussed more fully later in this chapter.

Solution of Eqs.(2.6), (2.7), and (2.8) will model the flow through any geometry when subjected to appropriate boundary conditions. However, with simplification of the boundary conditions and ease of programming in mind, the geometry to be considered was modified from that of Fig. 1.1. Modifications include the following:

a. The control nozzle and control ports have been omitted. Their effect on the inlet jet is modeled as a specified deflection, $\phi$, of the jet. The addition of control jet action into the model would be complex with regard to the programming involved, but does appear to be theoretically straightforward.

b. The amplifier considered is non-vented, as opposed to the vented amplifier of Fig. 1.1. This is realistic in the sense that non-vented amplifiers have use as flow dividers and flow signal amplifiers. However, it would greatly expand the usefulness of the model if a method for handling the vent flows could be devised. Such a method is not theoretically available at the present since it must allow for unknown flow rates, velocity profiles, and flow reversals.

c. A square cavity region is considered. This is solely to simplify the programming as sloping walls could be handled if desired.

d. The center vent is omitted. Addition of the center vent would be possible if a flow rate could be somehow established. A fully developed velocity profile corresponding to this flow rate could then be assumed.

e. The receivers are at a 45° angle to the amplifier centerline. As in (c) above, this is for programming convenience only.

The resulting geometry is shown in Fig. 2.1, where all lengths are non-dimensional and have arbitrarily selected magnitudes. The coordinate system is fixed such that the origin is at the lower left corner of the cavity region, and such that the y-axis is parallel to the amplifier centerline. The flow enters through the

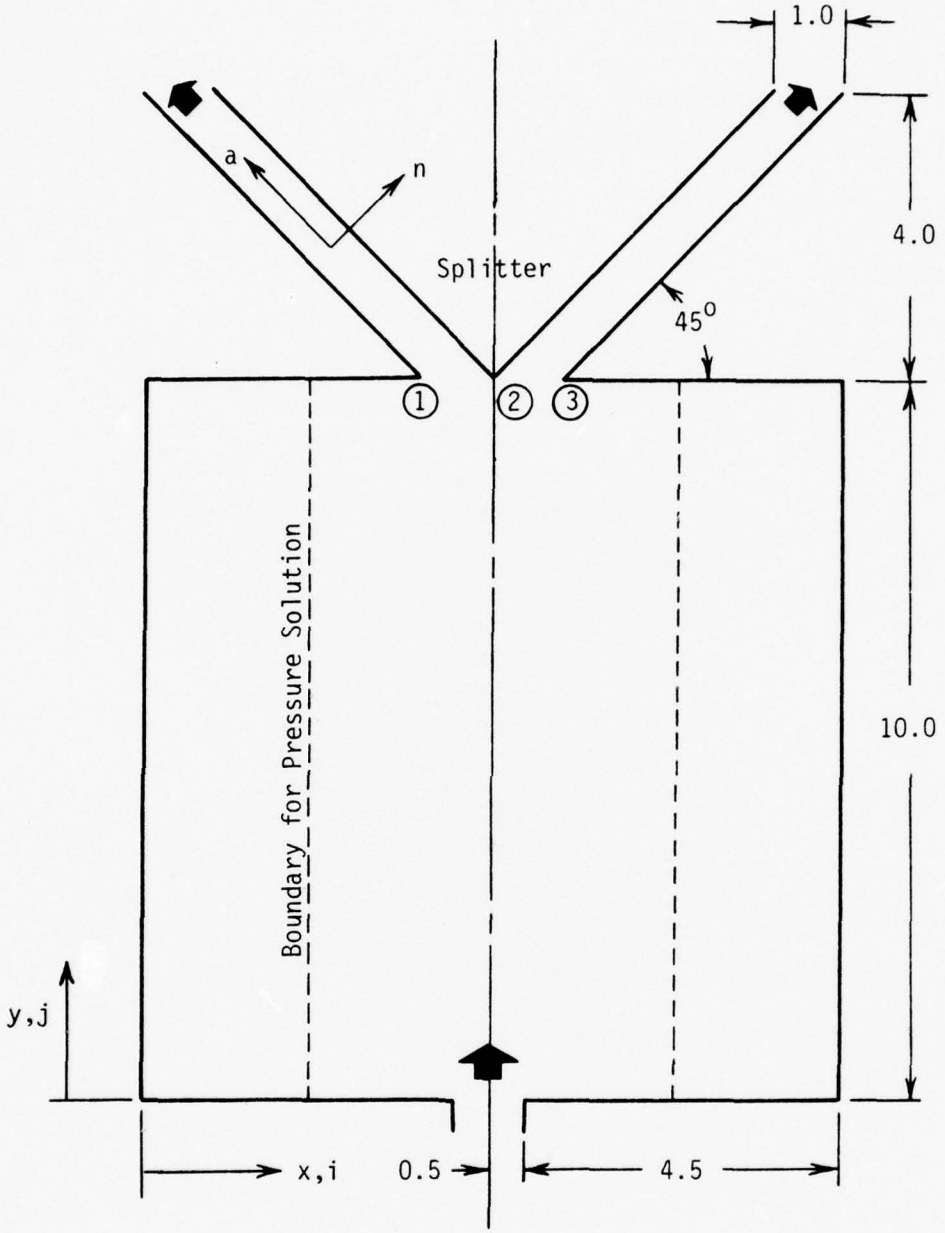


Figure 2.1. Amplifier Geometry
All Lengths Are Non-dimensional

single port at the bottom of Fig. 2.1, crosses the cavity region, and exits through the two receivers.

B. Boundary Conditions

For the geometry of Fig. 2.1, all boundaries are either walls or lines on which something is known about the velocity profile and flow rate. Continuum boundary conditions for these cases are as follows.

At the solid walls there exists a no slip condition. Setting u and v to zero in Eq.(2.5) the no slip condition implies a constant $\psi$ on each wall. It is assumed that the left wall of the amplifier has $\psi = 0$, where the reference value 0 was arbitrarily chosen. As noted earlier the flow variables are non-dimensionalized with respect to the average inflow velocity and the supply port width. Due to this choice of non-dimensionalizing variables, the right wall has $\psi = -1.0$.

The remaining solid surface is that positioned between the two receivers, which will be referred to as the splitter. The value given to $\psi$ on the splitter will be used to model different loadings on the receivers. As in all flow situations the flow through the receivers is proportional to the pressure drop down the receiver. Thus, changing the flow by changing $\psi$ on the splitter will model a different pressure condition at the outlet, given that the amplifier inlet conditions remain the same. Then for a given inlet condition a characteristic curve of receiver flow versus pressure, as in

Fig. 1.5, can be obtained by varying the flow rate in the receivers and recording the resulting pressures.

The new outlet pressure is not known until after the flow solution is obtained. Thus, the model will not accept a receiver outlet pressure as a boundary condition. This is a result of the required boundary conditions on the pressure equation.

At the inlet a fully developed parabolic velocity profile is assumed. It is necessary, however, to apply this condition in such a way that the inlet jet can have an initial specified deflection, $\phi$. This deflection is to partially model the effect of the control jets on the power jet. Although the control jets would have other effects on the flow field, their main purpose is to deflect the power jet. As pointed out earlier, this deflection is the physical mechanism which allows amplification in a fluidic amplifier. As such it is important to incorporate the deflection into the numerical model.

Consider the inlet configuration shown in Fig. 2.2. With n measured perpendicular to left wall of the inlet, a parabolic velocity profile leads to a stream function distribution of

$$\psi(n) = 2\left(\frac{n}{w}\right)^3 - 3\left(\frac{n}{w}\right)^2 \qquad (2.10a)$$

Since it is desired that $\psi$ vary from 0 to -1 across the inlet, the value of w decreases as $\phi$ increases in magnitude, but the inlet width in the x direction remains constant at a value of 1.

Under a coordinate transformation from the (n,a) to the (x,y) coordinate system, the values of $\psi$, $\zeta$, and $\partial\psi/\partial x$ remain invariant.

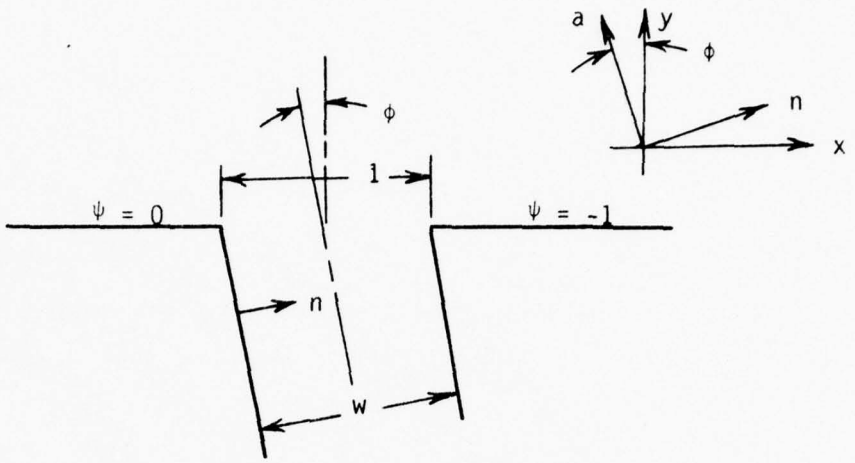


Figure 2.2. Amplifier Inlet Geometry

Only the value of $\partial\psi/\partial y$, or the u velocity, changes. Since $\partial\psi/\partial y$ was the only variable that changed with deflection, it was selected as one of the boundary conditions on the inlet flow. The vorticity distribution compatible with a parabolic velocity profile, which is derived from Eq.(2.10a), was selected as the other boundary condition. These two boundary conditions are

$$\frac{\partial\psi}{\partial y} = -6 \tan\phi \left[(x - x_0)^2 + (x - x_0)\right] \qquad (2.10b)$$

$$\zeta = 12 (x - x_0) - 6 \quad . \qquad (2.10c)$$

At the receiver outlets the flow has a developed profile, but the restriction of a parabolic profile is not imposed [20]. This assumption yields boundary conditions of the form

$$\frac{\partial\zeta}{\partial a} = 0 \qquad (2.11a)$$

$$\frac{\partial \psi}{\partial a} = 0 \tag{2.11b}$$

where the coordinate axis "a" is parallel to the receiver centerline.

Switching from the flow field boundary conditions to consideration of the pressure problem, the vorticity and stream function equations were derived in such a way that the pressure was eliminated. It follows that boundary conditions for the pressure equation must be compatible with Eqs.(2.1) through (2.3). The result is gradient boundary conditions for the pressure equation, which are given by

$$\begin{aligned} \frac{\partial P}{\partial x} &= \frac{1}{Re}\frac{\partial \zeta}{\partial y} - \frac{\partial \psi}{\partial y}\frac{\partial^2 \psi}{\partial x \partial y} + \frac{\partial \psi}{\partial x}\frac{\partial^2 \psi}{\partial y^2} \\ \frac{\partial P}{\partial y} &= -\frac{1}{Re}\frac{\partial \zeta}{\partial x} + \frac{\partial \psi}{\partial y}\frac{\partial^2 \psi}{\partial x^2} - \frac{\partial \psi}{\partial x}\frac{\partial^2 \psi}{\partial x \partial y} \quad . \end{aligned} \tag{2.12}$$

An elliptic partial differential equation, such as Eq.(2.8), which is subject to gradient boundary conditions on all boundaries, such as those given by Eq.(2.12), is commonly referred to as a Neumann problem. For this type of problem to have a solution a further constraint, known as a consistency equation, must be met [8,15,29]. This equation gives a unique relationship between the gradients of the dependent variable on the boundary and the forcing function of the partial differential equation. For the pressure problem this relationship is

$$\oint_{\text{Boundary}} \frac{\partial P}{\partial n}\, ds = \iint_{\text{Region}} 2\left[\frac{\partial^2 \psi}{\partial x^2}\frac{\partial^2 \psi}{\partial y^2} - \left(\frac{\partial^2 \psi}{\partial x \partial y}\right)^2\right] dx dy \tag{2.13}$$

where n is the outward directed normal from the boundary and s is tangential to the boundary.

A solution to Eq.(2.8) which meets the gradient boundary conditions given by Eq.(2.12) is not a unique solution to that system of equations since any solution plus a constant is also a solution [8]. A solution is made unique when it is also desired that there be a fixed value for pressure at some point within the boundaries. In effect, this particular value can be used to fix the constant referred to above.

## C. Finite Difference Solution for the Flow Field

As in any finite difference solution to a partial differential equation, the general procedure here is to discretize the vorticity transport and stream function equations to establish a system of algebraic equations. These algebraic equations can be solved for the values of $\psi$, $\zeta$, u, and v at all points on the finite difference grid.

The grid under consideration spans the region bounded by the amplifier boundaries shown in Fig. 2.1. The region is divided such that in the x direction there are $I_{max}$ grid points separated by a distance $\Delta x$. Similarly, in the y direction there are $J_{max}$ grid points separated by a distance $\Delta y$. $I_{max}$ and $J_{max}$ were chosen to produce a grid with $\Delta x = \Delta y = \Delta$, although this is not necessary. The notation used to distinguish a variable value at a given point is

$$\theta_{ij} = \theta \{(i - 1)\, \Delta x, (j - 1)\, \Delta y\} \tag{2.14}$$

where $\theta$ is an arbitrary variable, $1 \leq i \leq I_{max}$, and $1 \leq j \leq J_{max}$.

The system of algebraic equations obtained from the difference equations for stream function and vorticity are solved using alternating direction implicit (ADI) methods. The methods are based on the work of Peaceman and Rachford [17] and of Douglas [7]. Such methods are widely used in finite difference work. Descriptions of the method can be found in many books on finite difference methods, including those by Roache [20], Mitchell [15], Young [29], and Young and Gregory [30]. Solutions of viscous flow problems using ADI methods are discussed by Roache and examples are found in papers by Pearson [18], Briley [6], and Richards and Chavez [19]. A major reason for the use of ADI methods is that the splitting of directions produces systems of equations with tridiagonal coefficient matrices, for which solutions can be obtained very efficiently. Another reason for its use is its excellent stability characteristics. On parabolic equations this stability allows ADI methods to use much larger computational time steps than explicit methods. Thus, ADI methods use less computer time to reach a steady state solution. Also, the convergence rate of the method is good in solution of the elliptic stream function equation when a sequence of iteration parameters, a $\rho$-sequence, is used.

Along with selection of a solution technique, a differencing scheme was finally selected for Eqs.(2.6) and (2.7). Difficulties

with stability at higher Reynolds numbers led to the use of various initial differencing schemes on the nonlinear terms of the vorticity equation. In particular, second-order accurate, centered differencing for the advection terms was tried and abandoned in favor of the more stable, first-order accurate, first upwind differencing [20]. This method proved to have convergence problems at regions where velocity reversals occurred and was replaced by second upwind differencing [20]. Although different in algebraic form, this difference scheme can be shown to be the same as that used by Runchal, Wolfshtein and Spalding [23].

Centered differencing is used on the diffusion terms. The resulting difference equations for use with ADI in solving the vorticity transport equation are

x-sweep:

$$\frac{\zeta_{ij}^{n+\frac{1}{2}} - \zeta_{ij}^{n}}{\Delta t/2} = - \frac{[u_R\zeta_{RX} - u_L\zeta_{LX}]^{n+\frac{1}{2}}}{\Delta x} - \frac{[v_R\zeta_{RY} - v_L\zeta_{LY}]^{n}}{\Delta y}$$

$$+ \frac{1}{Re\Delta x^2}[\zeta_{i+1,j} + \zeta_{i-1,j} - 2\zeta_{ij}]^{n+\frac{1}{2}} \qquad (2.15a)$$

$$+ \frac{1}{Re\Delta y^2}[\zeta_{i,j+1} + \zeta_{i,j-1} - 2\zeta_{ij}]^{n}$$

y-sweep:

$$\frac{\zeta_{i,j}^{n+1} - \zeta_{ij}^{n+\frac{1}{2}}}{\Delta t/2} = -\frac{[u_R\zeta_{RX} - u_L\zeta_{LX}]^{n+\frac{1}{2}}}{\Delta x} - \frac{[v_R\zeta_{RY} - v_L\zeta_{LY}]^{n+1}}{\Delta y}$$

$$+ \frac{1}{Re\Delta x^2}[\zeta_{i+1,j} + \zeta_{i-1,j} - 2\zeta_{ij}]^{n+\frac{1}{2}} \qquad (2.15b)$$

$$+ \frac{1}{Re\Delta y^2}[\zeta_{i,j+1} + \zeta_{i,j-1} - 2\zeta_{ij}]^{n+1}$$

where

$$u_R = \tfrac{1}{2}(u_{i+1,j} + u_{i,j}) \qquad v_R = \tfrac{1}{2}(v_{i,j+1} + v_{i,j})$$

$$u_L = \tfrac{1}{2}(u_{i-1,j} + u_{i,j}) \qquad v_L = \tfrac{1}{2}(v_{i,j} + v_{i,j-1})$$

and

$$\zeta_{RX} = \begin{cases} \zeta_{i,j} & u_R > 0 \\ \zeta_{i+1,j} & u_R < 0 \end{cases} \qquad \zeta_{RY} = \begin{cases} \zeta_{i,j} & v_R > 0 \\ \zeta_{i,j+1} & v_R < 0 \end{cases}$$

$$\zeta_{LX} = \begin{cases} \zeta_{i-1,j} & u_L > 0 \\ \zeta_{i,j} & u_L < 0 \end{cases} \qquad \zeta_{LY} = \begin{cases} \zeta_{i,j-1} & v_L > 0 \\ \zeta_{i,j} & v_L < 0 \end{cases}$$

With the linear stream function equation second-order accurate, centered differencing was used on both second derivatives. The resulting difference equations for use with ADI are

x-sweep:

$$\psi_{i+1,j}^{k+\frac{1}{2}} - (2 + \rho_\ell)\, \psi_{ij}^{k+\frac{1}{2}} + \psi_{i-1,j}^{k+\frac{1}{2}}$$

$$= - [\psi_{i,j+1}^{k} - (2 + \rho_\ell)\, \psi_{ij}^{k} + \psi_{i,j-1}^{k}] - \Delta x^2 \zeta_{ij} \qquad (2.16a)$$

y-sweep:

$$\psi_{i,j+1}^{k+1} - (2 + \rho_\ell)\, \psi_{ij}^{k+1} + \psi_{i,j-1}^{k+1}$$

$$= - [\psi_{i+1,j}^{k+\frac{1}{2}} - (2 + \rho_\ell)\, \psi_{ij}^{k+\frac{1}{2}} + \psi_{i-1,j}^{k+\frac{1}{2}}] - \Delta y^2 \zeta_{ij} \qquad (2.16b)$$

where

$k$ = iteration index

$k+\frac{1}{2}$ = intermediate computation step

$\rho_\ell$ = iteration parameter, $1 \leq \ell \leq m$ .

The optimum sequence of iteration parameters $\rho_\ell$ is not known for the problem being considered. However, a sequence based on the Wachspress parameters [29] worked quite well. For purposes of evaluating this sequence the region of interest was taken as the largest square in the complete amplifier. This corresponds to the cavity region and is a square spanned by a grid of $I_{max}$ by $I_{max}$ points. The Wachspress parameters are given by

$$\rho_\ell = \beta\, (\alpha/\beta)^{\frac{\ell-1}{m-1}}, \qquad m \geq 2, \quad \ell = 1, 2, \ldots, m \qquad (2.16c)$$

where $\alpha$ and $\beta$ can be estimated by

$$\alpha = 4 \sin^2 \frac{\pi}{2 I_{max}} \tag{2.16d}$$

$$\beta = 4 \cos^2 \frac{\pi}{2 I_{max}} \tag{2.16e}$$

and m is the smallest integer such that

$$(0.414)^{2m} \leq \alpha/\beta \quad . \tag{2.16f}$$

For $I_{max} = 41$, this resulted in

$$m = 4$$

and

$$\rho_{\ell} = 3.9939 \, (0.001469)^{\frac{\ell-1}{3}} , \qquad \ell = 1, 2, 3, 4 \tag{2.16g}$$

Equations (2.15) and (2.16) will provide the necessary algebraic equations at all points in the interior of the grid. However, at the boundaries they would require information from points outside of the grid. Here the information contained in the continuum boundary conditions is used to form the necessary discrete equations.

On the solid walls the discrete values of $\psi$ are simply the continuum values of $\psi$. Then, for nodes on the walls

$$\psi_{i,j} = \begin{cases} 0.0, & \text{left wall} \\ \psi_{splitter}, & \text{splitter} \\ -1.0, & \text{right wall} \end{cases} \tag{2.17}$$

Two separate equations are used for the boundary values of vorticity on the walls, one in the cavity region and one in the

receivers. Both are derived using the no slip wall condition. For the cavity region the derivation involves approximating $\psi$ with a four point, cubic, LaGrangian interpolating polynomial. This can be differentiated twice and, using the velocity on the wall and the definition of vorticity, evaluated at the wall. The result is a second-order accurate approximation for $\zeta$ on the wall [6].

For example, consider the wall point shown in Fig. 2.3.

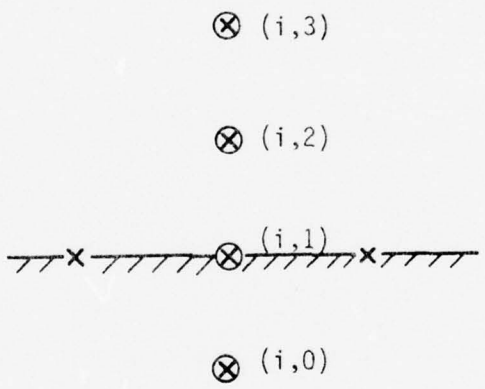


Figure 2.3. Grid Notation

For these points

$$\psi(y) = \frac{1}{6\Delta y^3}\left[-(y-y_1)(y-y_2)(y-y_3)\,\psi_{i,0}\right.$$
$$+ 3(y-y_0)(y-y_2)(y-y_3)\,\psi_{i,1} \qquad (2.18a)$$
$$- 3(y-y_0)(y-y_1)(y-y_3)\,\psi_{i,2}$$
$$\left.+ (y-y_0)(y-y_1)(y-y_2)\,\psi_{i,3}\right]$$

where $y_j$ denotes y at the point (i,j). Differentiating this once and evaluating on the wall gives

$$u_{i,1} = \frac{\partial \psi}{\partial y}\bigg|_{i,1} = 0 = \frac{1}{\Delta y}\left(-2\psi_{i,0} - 3\psi_{i,1} + 6\psi_{i,2} - \psi_{i,3}\right) . \tag{2.18b}$$

Differentiating again and evaluating at the wall gives

$$\frac{\partial^2 \psi}{\partial y^2}\bigg|_{i,1} = \frac{1}{\Delta y^2}\left(\psi_{i,0} - 2\psi_{i,1} + \psi_{i,2}\right) . \tag{2.18c}$$

Since $\psi$ is constant on the wall

$$\zeta_{i,1} = \frac{\partial^2 \psi}{\partial y^2}\bigg|_{i,1} . \tag{2.18d}$$

Eliminating $\psi_{i,0}$ from Eqs.(2.18b) and (2.18c) and substituting with Eq.(2.18d),

$$\zeta_{i,1} = \frac{1}{2\Delta y^2}\left(-7\psi_{i,1} + 8\psi_{i,2} - \psi_{i,3}\right) . \tag{2.18e}$$

As recommended by Briley [6], to increase stability the velocity at the point adjacent to the wall is also evaluated from Eq.(2.18a). The point (i,2) in Fig. 2.3 is such a point. Its u-velocity is given by

$$u_{i,2} = \frac{1}{4\Delta y}\left(-5\psi_{i,1} + 4\psi_{i,2} + \psi_{i,3}\right) . \tag{2.18f}$$

The values of $\zeta$ on the sloping walls of the receivers can be derived using two Taylor series expansions for $\psi$ at a wall node. For

example, consider the left wall of the left receiver. About a point (i,j) on the wall

$$\psi_{i+1,j} = \psi_{i,j} + \frac{\partial\psi}{\partial x}\bigg|_{i,j} \Delta x + \tfrac{1}{2}\Delta x^2 \frac{\partial^2\psi}{\partial x^2}\bigg|_{i,j} + O(\Delta x^3) \quad (2.19a)$$

$$\psi_{i,j+1} = \psi_{i,j} + \frac{\partial\psi}{\partial y}\bigg|_{i,j} \Delta y + \tfrac{1}{2}\Delta y^2 \frac{\partial^2\psi}{\partial y^2}\bigg|_{i,j} + O(\Delta y^3) . \quad (2.19b)$$

Due to the no slip condition the first derivatives are zero and can be eliminated. Further simplification is achieved by replacing $\Delta x$ and $\Delta y$ with $\Delta$ and adding the two equations. Rearranging and using Eq.(2.7), the expression for vorticity is

$$\zeta_{i,j} = \frac{2}{\Delta^2} (\psi_{i+1,j} + \psi_{i,j+1} - 2\psi_{ij}) + O(\Delta) \quad . \quad (2.19c)$$

Similar expressions hold for $\zeta_{i,j}$ on the other receiver walls.

In the inlet the vorticity boundary condition is given by the discrete analog of Eq.(2.10c), which is

$$\zeta_{i,1} = 12 \left((i-1)\,\Delta x - x_0\right) - 6 \quad . \quad (2.20)$$

The boundary condition on $\psi$ in the inlet is derived from a Taylor series expansion for $\psi$ about a point in the inlet, that is

$$\psi_{i,2} = \psi_{i,1} + \Delta y \frac{\partial\psi}{\partial y}\bigg|_{i,1} + \frac{\Delta y^2}{2} \frac{\partial^2\psi}{\partial y^2}\bigg|_{i,1} + O(\Delta y^3) . \quad (2.21a)$$

The first derivative in this expression is obtained from Eq.(2.10b). An expression for the second derivative is obtained from Eq.(2.7), where $\zeta_{i,1}$ is known and $\partial^2\psi/\partial x^2$ can be evaluated using centered

differences. Substituting into Eq.(2.21a) the resulting expression is

$$\psi_{i,1} = \tfrac{1}{4}\,(2\psi_{i,2} - 12\Delta y \tan\phi\,\{(i\Delta x - \Delta x - x_0)^2 + i\Delta x - \Delta x - x_0\} - \Delta^2\zeta_{i,1} + \psi_{i+1,1} + \psi_{i-1,1}) + O(\Delta y^2) \tag{2.21b}$$

which would be second-order accurate due to the differencing of $\partial^2\psi/\partial x^2$.

At the receiver outlets one-sided difference expressions were used for the first derivatives in Eq.(2.11). For the two receivers this resulted in four expressions:

Left receiver,

$$\begin{aligned} \zeta_{i,j} &= \zeta_{i+1,j-1} \\ \psi_{i,j} &= \psi_{i+1,j-1} \end{aligned} \tag{2.22}$$

Right receiver,

$$\begin{aligned} \zeta_{i,j} &= \zeta_{i-1,j-1} \\ \psi_{i,j} &= \psi_{i-1,j-1} \end{aligned} \tag{2.22}$$

Special care was given to the values of vorticity at the sharp corners in the amplifier geometry. At those six corners which are concave there is no problem, since these points never enter into the calculations. However, at the convex corners of the receiver inlets the proper value of $\zeta$ to use was in question. Following Roache's

recommendations [20], the procedure being used is to allow $\zeta$ to be discontinuous at these points. If the value of $\zeta$ is needed for calculations dealing with mesh points inside the receivers, $\zeta$ is defined as in Eq.(2.19c). If the flow outside the receiver in the main amplifier cavity region is being considered, $\zeta$ is defined as in Eq.(2.18e).

At the receiver outlets one corner point enters the calculations. However, its value is defined by considering the point to have an extension of the wall beyond it. Thus $\zeta$ at this point is evaluated as in Eq.(2.22).

At the corners of the amplifier inlet the value of vorticity is again discontinuous. The two choices considered for defining this value were either to base it on the values of $\psi$ in the adjacent flow field, as in Eq.(2.19c), or to include it as part of the inlet profile, as in Eq.(2.20). Based on the comparison of numerical and experimental results, vorticity for these two points was defined as in Eq.(2.20).

Using an implicit method on the vorticity equation can produce a problem with the boundary conditions. The solution for the n+1 time step requires boundary values which are not available [20], since they also need to be at the n+1 level. Further, using lagged boundary conditions, i.e. using boundary conditions based on information at the $n^{th}$ time level, has been shown to be numerically destabilizing [20]. The procedure chosen to resolve this problem is to:

a. Extrapolate using past values of $\zeta_w$ for an estimate of $\zeta_w^{n+1}$. Here the subscript w denotes a wall value.

b. Extrapolate using past values of $u_{i,j}$ and $v_{i,j}$ for an estimate of $u_{i,j}^{n+1}$ and $v_{i,j}^{n+1}$.

c. Calculate new values of $\zeta_{i,j}^{n+1}$.

d. Calculate new values of $\psi_{i,j}^{n+1}$.

e. Calculate new estimates for $u_{i,j}^{n+1}$, $v_{i,j}^{n+1}$ and $\zeta_w^{n+1}$ using $\psi_{i,j}^{n+1}$.

f. Compute the change in wall vorticity.

g. If convergence occurs, as will be discussed later, go to the next time step. If not, go back through (c) to (g) until convergence is achieved or until a prescribed number of iterations have been completed.

This procedure is suggested by Roache and is similar to that used by Briley [6].

It is also possible with the above iteration scheme to set a variable time step based on the numbers of iterations for convergence of the previous time step [6]. This allows the solution to use a time step which is, in a sense, numerically optimal.

There are three convergence criteria involved in this solution technique. These are convergence of the overall flow field, convergence of the boundary values of vorticity at each time step, and convergence of the stream function at each time step. The overall solution is considered converged when the normalized, relative change in vorticity over a time step is less than some $\varepsilon$ for each

point in the mesh. That is, the solution is converged when for all points

$$\left|\zeta^{n+1} - \zeta^{n}\right| < \left[\frac{1}{NP}\sum_{i=1}^{I_{max}}\sum_{j=1}^{J_{max}}\left|\zeta_{i,j}\right|\right] \times \left[\frac{\Delta t}{\Delta t_{ref}}\right] \times \varepsilon \qquad (2.23)$$

where

NP = number of points in the flow field

$\Delta t_{ref}$ = reference time step.

A typical value for $\varepsilon$ is 0.001.

The convergence criteria on the boundary values of vorticity and on the stream function are interrelated and designed so that they become more stringent as the overall solution converges. As the flow field solution approaches steady state the change in vorticity across a time step, $\left|\zeta_w^{n+1} - \zeta_w^{n}\right|$, becomes smaller. Therefore, the allowed change between estimates of $\zeta_w^{n+1}$ must be reduced. To implement this check on convergence, the criterion used is that at each wall point

$$\left|\zeta_w^{q+1} - \zeta_w^{q}\right| \leq \frac{F_1}{LCP}\sum\left|\zeta_w^{n+1} - \zeta_w^{n}\right| \equiv WZTEST \qquad (2.24)$$

where

q = an iteration counter

LCP = number of boundary points

$F_1$ = constant factor, typically 0.5.

This criterion prevents unnecessary computational labor at early solution times but guarantees that convergence will always be sufficiently stringent.

Also, since wall vorticity is calculated from stream function values at adjacent grid points, Eqs.(2.19c) and (2.18e), the stream function convergence must be related to the criterion for wall vorticity convergence. Upon acceptable convergence of the stream function the allowed magnitude of change, $\left|\psi_{i,j}^{k+1} - \psi_{i,j}^{k}\right|$, must be less than the magnitude of change, WZTEST, allowed for the wall vorticity. As an example, consider the following. If the convergence on $\psi$ were such that $\left|\psi_{ij}^{k+1} - \psi_{ij}^{k}\right| \approx 0.001$, then the variation in $\zeta_w$ in Eq.(2.19c) due solely to lack of convergence of $\psi$ would be on the order of $0.002/\Delta x^2$. This could easily be greater than the allowed change in $\zeta_w$. To prevent such an occurrence the stream function at each grid point is converged to

$$\left|\psi_{ij}^{k+1} - \psi_{ij}^{k}\right| \leq F_2 \times \text{WZTEST} \tag{2.25}$$

where $F_2$ is a constant factor, typically 0.005.

This completes the discussion of the discrete solution technique for the flow field. In summary the solution sequence is:

a. Assume an initial distribution for $\psi_{i,j}^{n}$, $\zeta_{i,j}^{n}$, the necessary boundary conditions, and velocities.
b. Calculate $\zeta^{n+1}$ using ADI.
c. Calculate $\psi^{n+1}$ using ADI.
d. Calculate new boundary conditions for $\zeta^{n+1}$.
e. Iterate on (b) through (d) until convergence criterion on $\zeta_w^{n+1}$ is satisfied.

f. Check overall convergence of $\zeta_{i,j}$. Stop if solution converged.

g. Update the time step index, varying the time step if desired.

h. Extrapolate for $u_{i,j}^{n+1}$ and $v_{i,j}^{n+1}$ velocity components and $\zeta_w^{n+1}$ values.

i. Return to (b).

D. Method of Solution for the Pressure Field

As pointed out earlier, two separate approaches could be taken in solving for the necessary pressure values. The method involving integration along a path, Eq.(2.9), has at least one possibly serious disadvantage. *Since the static pressure is a point function and not* a path function, integration between points A and B on two separate paths should produce the same value for the pressure at B. However, as Roache [20] points out this could be very difficult to achieve numerically. In obtaining the pressure gradients to be integrated, error would be introduced by the numerical differentiation necessary to evaluate Eq.(2.12). Error would also be introduced by the numerical integration of the resulting values.

Because of these problems, Roache recommends the solution of Eq.(2.8) for the desired pressure field. That approach was adopted, partially on this recommendation and partially because solution of Eq.(2.8) was anticipated to be straightforward. Except for the change in boundary conditions this is the same type of system which

governs the stream function, Eq.(2.7). However, solution of the pressure system has proven to be considerably more difficult, due both to the gradient boundary conditions and to the evaluation of the forcing function. In particular, the calculations are complicated by a failure of the system to satisfy the discrete analog of Eq.(2.13), the consistency equation.

As for the flow field, a set of simultaneous algebraic equations must be established from the discrete analog to Eq.(2.8). This set is of the form

$$\underline{A}\,\underline{P} = \underline{S}$$

where if

N is the number of unknown pressure values,

then

$\underline{P}$ is a (N x 1) vector of the pressures $P_{ij}$,
$\underline{A}$ is a (N x N) matrix of difference coefficients, and
$\underline{S}$ is a (N x 1) vector containing values for the right-hand side of Eq.(2.8) and for the gradient boundary conditions.

As a check on the differencing techniques used, Eq.(2.26) must reflect the fact that the Neumann problem of Eqs.(2.8) and (2.12) has no unique solution. However, because a unique solution may be found in terms of one given pressure value at one point in the field, it has to follow that $\underline{A}$ in Eq.(2.26) is singular and of rank N-1.

Expanding this idea, consider each column of $\underline{A}$, denoted as $\underline{a}_m$, as a vector in an N-space. Define an additional vector $\underline{c}$ ,

$$\underline{c}^T = [c_1, c_2, c_3, \ldots, c_m, \ldots, c_N] \; . \tag{2.27}$$

If a $\underline{c}$ can be found which is mutually orthogonal to each $\underline{a}_m$, then there has to be at least one linear dependency in the set of vectors $\underline{a}_m$. (Only N vectors in an N-space can be mutually orthogonal.) Further, such a vector will also be orthogonal to the $\underline{S}$ vector. If it is assumed that there is only one linear dependence in the set $\underline{a}_m$, it can be concluded that $\underline{A}$ is of rank (N-1). Thus, the differencing technique used would retain the characteristics of the Neumann problem.

Practically, for a proper difference formulation of the Neumann problem, a matrix $\underline{C}$ can be found by inspection such that

$$\underline{C}_{(N\times N)} = \text{diag}\,(c_1, c_2, c_3, \ldots, c_m, \ldots, c_N) \tag{2.28}$$

Note that due to the definition of $\underline{c}$ the columns of the product $\underline{CA}$ will sum to zero and the elements of the vector $\underline{CS}$ will sum to zero. This second summation is, in fact, equivalent to a numerical evaluation of Eq.(2.13) with the proper choice of integration formulas. This summation will be referred to as the discrete analog of the consistency equation. The above information provides a method for evaluating and developing the necessary difference equations.

In particular, the summation of elements in the columns of $\underline{CA}$ is a check on the implementation of boundary conditions. If not properly implemented, the summations cannot all be made equal to zero.

With this in mind, difference approximations were derived for the interior and boundary grid points. For interior grid points the

standard five point centered difference approximation was used to difference Eq.(2.8), that is

$$P_{i,j} = \tfrac{1}{4}\,(P_{i+1,j} + P_{i-1,j} + P_{i,j+1} + P_{i,j-1} - \Delta^2 s_{i,j}) \tag{2.29}$$

where

$$s_{i,j} = 2\left[\left.\frac{\delta^2\psi}{\delta x^2}\right|_{i,j}\left.\frac{\delta^2\psi}{\delta y^2}\right|_{i,j} - \left(\left.\frac{\delta^2\psi}{\delta x\delta y}\right|_{i,j}\right)^2\right]$$

At non-corner points of the cavity boundary, the discrete boundary equation is similar to Eq.(2.21b) and is derived in the same manner. For instance, on the lower cavity boundary

$$P_{i,1} = \tfrac{1}{4}\left[2P_{i,2} + P_{i+1,1} + P_{i-1,1} - 2\left.\frac{\delta P}{\delta y}\right|_{i,1}\Delta - \Delta^2 s_{i,j}\right] \tag{2.30}$$

with $\left.\frac{\delta P}{\delta y}\right|_{i,1}$ obtained by differencing Eq.(2.12).

The difference equation is similar for the four concave corner points on the boundary in the cavity region and for the non-corner points on the receiver walls. As shown in Fig. 2.4, in both cases only two adjoining grid points are available to form the needed difference approximation.

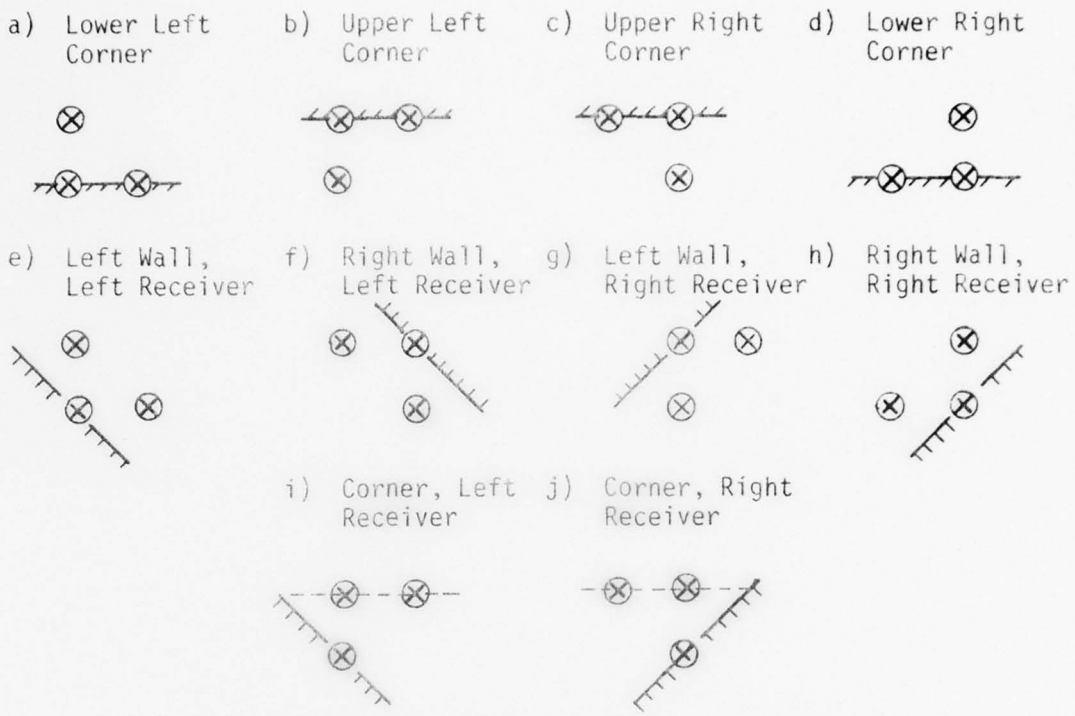


Figure 2.4. Grid Configurations for Concave Corners and Receiver Walls

Let the point being considered be (i,j). Let the adjoining point in the x-direction have coordinates (i',j), where i' = i±1. Similarly, let the adjoining point in the y-direction be at (i,j'), where j' = j±1. Define ID as (i' - i)$\Delta$x and JD as (j' - j)$\Delta$y. Then, using Taylor series expansions

$$P_{i',j} = P_{i,j} + ID \left.\frac{\partial P}{\partial x}\right|_{i,j} + \frac{\Delta x^2}{2} \frac{\partial^2 P}{\partial x^2} + O(\Delta x^3) \qquad (2.31a)$$

$$P_{i,j'} = P_{i,j} + JD \left.\frac{\partial P}{\partial y}\right|_{i,j} + \frac{\Delta y^2}{2} \frac{\partial^2 P}{\partial y^2} + O(\Delta y^3) \; . \qquad (2.31b)$$

Adding and using Eq.(2.8) to introduce $s_{i,j}$,

$$P_{i,j} = \tfrac{1}{2}\left( P_{i',j} + P_{i,j'} - ID \left.\frac{\partial P}{\partial x}\right|_{i,j} - JD \left.\frac{\partial P}{\partial y}\right|_{i,j} - \frac{\Delta^2}{2} s_{i,j} \right) + O(\Delta^3) \quad . \tag{2.31c}$$

At the inlets and outlets to the receivers the difference formulas had to be matched with the surrounding difference patterns in order to insure the singularity of $\underline{A}$. As pointed out, the criterion for this was the summation of the columns of $\underline{CA}$. The equations were derived by considering the derivatives of pressure discontinuous, writing Taylor series, and summing these series in such a way that the criterion was met. The derivation for the point of the splitter, point 2 on Fig. 2.1, will be presented. The other derivations are similar and only the results will be presented. At the splitter point

$$P_{i-1,j} = P_{i,j} - \Delta x \left.\frac{\partial P}{\partial x}\right|_{-} + O(\Delta x^2) \tag{2.32a}$$

$$P_{i,j-1} = P_{i,j} - \Delta y \left.\frac{\partial P}{\partial y}\right|_{-} + O(\Delta y^2) \tag{2.32b}$$

$$P_{i+1,j} = P_{i,j} + \Delta x \left.\frac{\partial P}{\partial x}\right|_{+} + O(\Delta x^2) \quad . \tag{2.32c}$$

The subscripts on the derivatives denote the coordinate direction in which the discrete derivative is evaluated. If "-", then variables at points to the left or points below (i,j) are used in the derivative evaluation. If "+", the variables to the right or above (i,j) are used. Adding the above equations

$$P_{i,j} = \tfrac{1}{3}\left(P_{i-1,j} + P_{i,j-1} + P_{i+1,j} + \Delta x \left.\frac{\partial P}{\partial x}\right|_{-} + \Delta y \left.\frac{\partial P}{\partial y}\right|_{-} - \Delta x \left.\frac{\partial P}{\partial x}\right|_{+}\right) + O(\Delta x^2) \quad . \tag{2.32d}$$

For points 1 and 3 on Fig. 2.1, the results are

For 1:
$$P_{i,j} = \frac{1}{3.5}\left[\tfrac{1}{2}P_{i-1,j} + P_{i+1,j} + P_{i,j+1} + P_{i,j-1} + \frac{\Delta}{2}\left.\frac{\partial P}{\partial x}\right|_{-} - \Delta \left.\frac{\partial P}{\partial x}\right|_{+} - \Delta \left.\frac{\partial P}{\partial y}\right|_{+} + \Delta \left.\frac{\partial P}{\partial y}\right|_{-}\right] \tag{2.33}$$

For 3:
$$P_{i,j} = \frac{1}{3.5}\left[\tfrac{1}{2}P_{i+1,j} + P_{i-1,j} + P_{i,j+1} + P_{i,j-1} - \frac{\Delta}{2}\left.\frac{\partial P}{\partial x}\right|_{+} + \Delta \left.\frac{\partial P}{\partial x}\right|_{-} - \Delta \left.\frac{\partial P}{\partial y}\right|_{+} + \Delta \left.\frac{\partial P}{\partial y}\right|_{-}\right] \tag{2.34}$$

As illustrated in Fig. 2.4, the grid points on the acute angle corners of the receiver outlets are omitted. Both corners of each receiver are then differenced as in Eq.(2.29c). The remaining outlet points were differenced as

$$P_{i,j} = \tfrac{1}{3}\left(P_{i,j-1} + P_{i+1,j} + P_{i-1,j} + \Delta \left.\frac{\partial P}{\partial y}\right|_{-}\right) + O(\Delta y^2) \quad . \tag{2.35}$$

The system of algebraic equations formed from the above difference equations could be solved with either ADI or point successive over-relaxation, SOR [20,29]. SOR was chosen because of its simplicity and the ease with which it can be applied and because the speed of convergence was not of prime importance. For this problem the SOR algorithm can be written as

$$P_{i,j}^{k+1} = (1 - \omega_0)\, P_{i,j}^{k} + \omega_0 P_{i,j}^{*} \quad . \tag{2.36}$$

Here $\omega_0$ is the relaxation factor, k is the iteration index, and $P_{i,j}^{*}$ is the value of $P_{i,j}$ given by the appropriate equation from the group of Eqs.(2.27) through (2.33).

In general there exists an optimum value $\omega_0$ of the factor $\omega$, $1 \leq \omega_0 \leq 2$. However, for the Neumann problem on a non-rectangular grid there is no analytic expression for this value. To estimate $\omega_0$ the procedure adopted was to calculate $\omega_0$ for use with Poisson's equation and Dirchilet boundary conditions. As discussed by Roache [20] a value slightly larger than this was then used for $\omega_0$. For a 41 x 57 grid the $\omega_0$ chosen was 1.9.

The evaluation of $s_{i,j}$, $(\delta P/\delta y)\big|_{i,j}$ and $(\delta P/\delta x)\big|_{i,j}$ remains to be discussed. These values must be obtained through numerical differentiation of the discrete flow field solutions. The complete set of difference equations is presented in Table A.1 of the Appendix. There are, however, several general comments that need to be made.

The numerical differentiation is complicated by the need for one sided differencing on solid walls and away from discontinuities

in vorticity. This problem is helped somewhat by narrowing the region of interest. The pressure field of interest is that near the jet as it issues from the inlet, flows across the cavity, and flows down the receivers. Since the pressure gradients, and thus the boundary conditions, can be evaluated at any point and since there is no need for the pressure values in the cavity side regions, only the central half of the cavity region is included in the pressure solution. This results in the new boundaries shown by the dotted lines in Fig. 2.1. Besides reducing the total number of SOR calculations, this allows the use of central differencing for both $s_{i,j}$ and $(\partial P/\partial y)\big|_{i,j}$ on the new boundaries.

The second comment concerns the evaluation of derivatives in the receivers. In this region of relatively high gradients normal to the wall there are relatively few grid points. Thus, in the normal discrete x-y grid system the values of $s_{i,j}$ are noticeably inaccurate. For example, towards the end of the receivers the flow becomes fully developed. For this case, $s_{i,j}$ should be zero. This result was not obtained with differencing in the normal coordinate system. For this reason a transformation of coordinates was made in each receiver such that the new system had one axis parallel to the centerline of the receiver. Such a coordinate system is shown in the left receiver of Fig. 2.1. This transformation introduced discrete derivatives in the axial direction. These derivatives go to zero as is required. For instance,

$$s_{i,j} = 2\left[\left.\frac{\delta^2\psi}{\delta x^2}\right|_{i,j}\left.\frac{\delta^2\psi}{\delta y^2}\right|_{i,j} - \left(\left.\frac{\delta^2\psi}{\delta x\delta y}\right|_{i,j}\right)^2\right]$$

$$= 2\left[\left.\frac{\delta^2\psi}{\delta a^2}\right|_{i,j}\left(\zeta_{i,j} - \left.\frac{\delta^2\psi}{\delta a^2}\right|_{i,j}\right) - \left(\left.\frac{\delta^2\psi}{\delta a\delta n}\right|_{i,j}\right)^2\right] \qquad (2.37)$$

Since the streamlines become parallel to the walls at the end of the receivers, the $\psi$ values do not change in the axial direction. Therefore, $\delta\psi/\delta a$ and $\delta^2\psi/\delta a^2$ go to zero and $s_{i,j}$ goes to zero.

The third comment, and certainly the most important, is that no difference scheme was found that would produce values for the gradients and the forcing functions, $s_{ij}$, that would satisfy the discrete consistency equation. A discussion of what this means physically, what the effects on the numerical solution are, and possible causes will be reserved for later. At this point a method for compensating for the inconsistency difficulty will be presented.

It was noted during the study that for inconsistent formulations, i.e. those for which the elements of $\underline{CS}$ did not sum to zero, the SOR algorithm would converge to values for which $\nabla^2 P|_{i,j} \neq s_{i,j}$. For every point the solution was in error by the same amount, s', where $s' = \nabla^2 P|_{i,j} - s_{i,j}$. Further, the value of the numerical integral of s' over the region was equal to the summation of the elements of $\underline{CS}$, that is, to the inconsistency. Therefore, weighting the contribution of each point by its contribution to the numerical

integral and knowing the total inconsistency, s' is a calculable quantity.

The method for compensating for inconsistency is based on this calculation of s'. After evaluation of the boundary gradients and $s_{i,j}$ the inconsistency is calculated. From the inconsistency, s' is determined. This value is then combined with each $s_{i,j}$ in such a way, meaning either added or subtracted, that the inconsistency is forced to zero.

This compensation is not proposed as a correction for inconsistency or as a completely satisfactory solution to the problem. It is simply a means of eliminating some of the obviously incorrect results produced by inconsistency. There are several noticeable effects of inconsistency which will be discussed in detail later. Briefly an inconsistent formulation results in solutions which

a. Do not have the gradients specified by the boundary conditions.

b. Do not produce the specified forcing function.

c. Do not converge to symmetric pressure fields for symmetric flow fields.

Although not necessarily producing more accurate solutions, the inconsistency compensation does alleviate these problems.

Solution of the pressure equation subject to all gradient boundary conditions defines a unique surface shape. Therefore, the important characteristic of the discrete solution is convergence to

this shape, not to some unique set of pressure values. The following procedure was used to check for this characteristic:

a. Select one point in the grid as a reference point, say (g,h), and select some reference value of pressure for this point, say 1.0.

b. Determine the deviation of $P_{g,h}$ from its reference value.

c. Translate the entire surface by adding the deviation to each $P_{i,j}$. $P_{g,h}$ then equals the reference value.

d. Calculate new values of $P_{i,j}$ using SOR and allowing $P_{g,h}$ to change. Then translate the new pressure surface. Now $P^{k+1}_{g,h} - P^{k}_{g,h} = 0$.

e. Determine the largest deviation between $P^{k+1}_{i,j}$ and $P^{k}_{i,j}$, i.e. $\left|P^{k+1}_{i,j} - P^{k}_{i,j}\right|_{max}$. As the surface shape converges this deviation will approach zero.

f. Terminate the calculations when

$$\left|P^{k+1}_{i,j} - P^{k}_{i,j}\right|_{max} < \varepsilon \qquad (2.38)$$

where $\varepsilon$ is a fixed number, typically $10^{-6}$.

The above procedure is similar to that proposed by Fanning and Mueller [8].

This completes the discussion of the solution technique for the pressure field. In summary the solution sequence is:

a. Calculate $s_{i,j}$, the necessary gradient boundary conditions, and compensate for inconsistency.

b. Assume an initial distribution for pressure.

c. Translate the $P^{k}_{i,j}$ values.

d. Calculate $P^{k+1}_{i,j}$ using SOR. Note that new values of $P^{k+1}_{i,j}$ on the boundary are also calculated.

e. Translate the $P^{k+1}_{i,j}$ values.

f. Check for convergence of the surface. Stop if solution converged.

g. Store $P^{k+1}_{i,j}$ in $P^{k}_{i,j}$ array and return to (d).

# C H A P T E R  I I I

## EXPERIMENTAL APPARATUS AND PROCEDURE

This chapter discusses the objective, equipment, and procedures for the experimental portion of this study. This includes a detailed description of the design and construction of the experimental model itself and of the associated fluid supply system. Also included in this chapter is a discussion of the instrumentation, dye injection techniques, and the photographic techniques which were used for the flow visualization.

### A. Overview

The purpose of the experimentation was to provide data for verifying the numerical simulations. Basically, a model was designed and constructed such that the flow in the horizontal midplane is a laminar, essentially two dimensional flow and is bounded by the geometry shown in Fig. 2.1. Streamline patterns were produced by injecting dye into this midplane. These patterns can be qualitatively compared to the numerically predicted streamline patterns for the same flow conditions. This flow visualization is used as qualitative verification of the predicated flow fields.

Because of practical complexity in constructing a model to allow deflection of the power jet, only the symmetric undeflected

case was studied experimentally. It is felt that pattern verification in this case, which can include asymmetric loading, would be sufficient.

Specific design requirements of the model and experimental apparatus were as follows:

a. The geometry of the test section must be identical to that of Fig. 2.1. Model walls must be transparent to permit flow visualization.

b. The flow in the test section must be laminar and free of small amplitude disturbances.

c. Inlet and outlet flow rates must be adjustable and must be measured.

d. Dye must be injected so as to illustrate the flow patterns but not disturb the flow.

e. Photographic equipment and lighting must be provided for recording the flow patterns.

These design requirements led to the experimental apparatus shown in Fig. 3.1. This apparatus can be divided into the model, the fluid supply system, instrumentation, and photographic equipment.

## B. Model

The model designed to meet these requirements is fairly simple in design but was rather difficult to construct. A plan view is shown in Fig. 3.2. The walls, cover plate and base plate were made of clear plexiglass. Use of plexiglass provided smooth surfaces

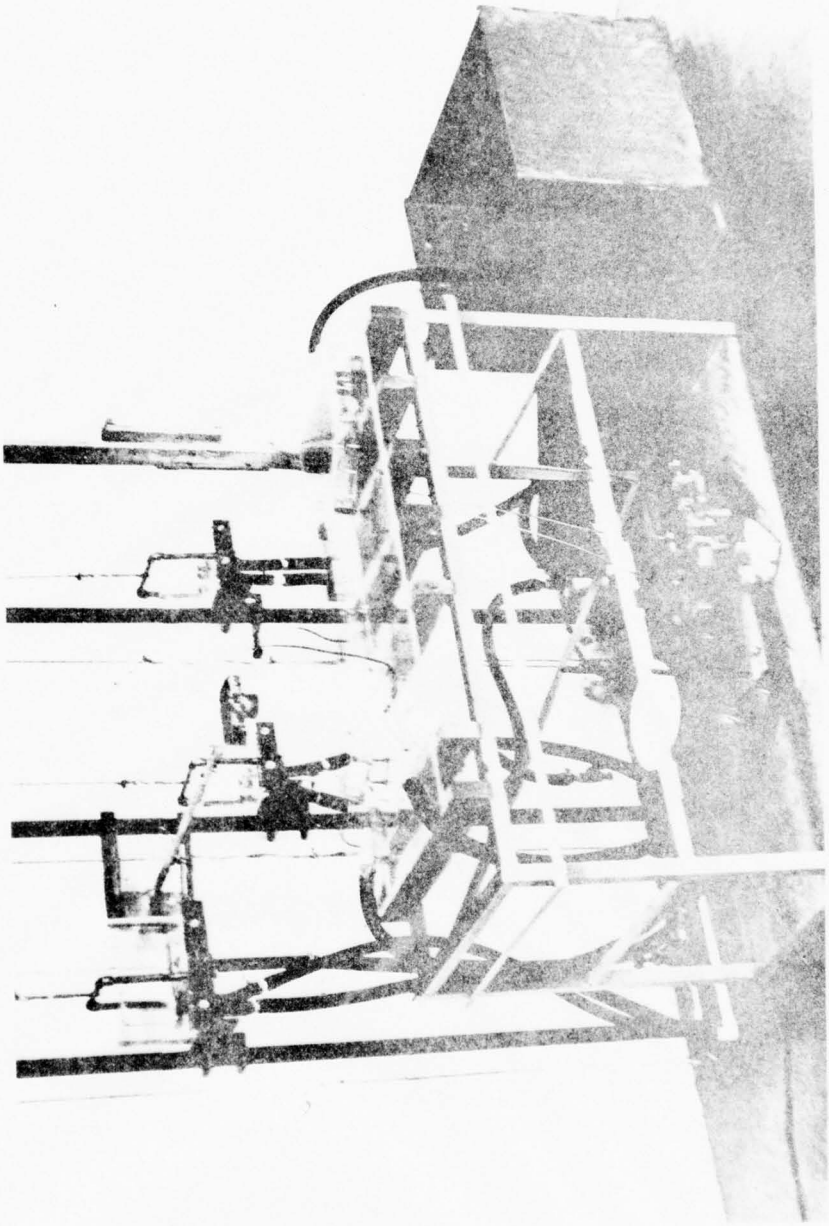

Figure 3.1. Experimental Equipment

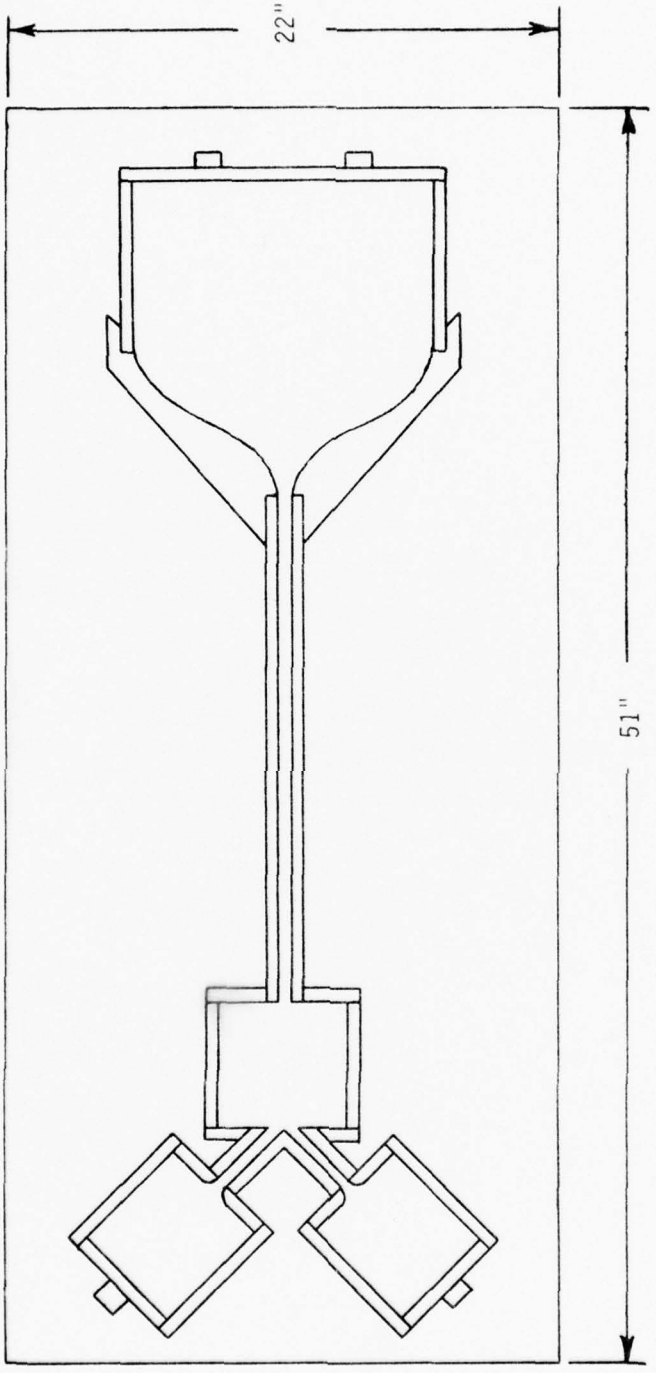


Figure 3.2. Plan View of Experimental Model

which helped minimize flow disturbances. Each wall section was made separately and then joined to form the model. This allowed the desired shape to be obtained and also allows for construction of differing geometries in future experimentation.

The joints between mating plexiglass sections had to be liquid tight and, in addition, it was desired that it be possible to disassemble the model. Thus, a permanent chemical bond of the plexiglass was not possible. Instead, satisfactory joints were formed by

a. Machining all mating surfaces with an end mill to form flat, square surfaces. This also resulted in adherence to the specified dimensions.

b. Drilling and tapping the walls and cover plates to allow for joining with nylon machine screws. Use of these screws was limited somewhat in the test section since it was desired to allow for future changes in the geometry of that section.

c. Both joining and sealing all mating surfaces with silicone rubber sealer.

The cover plate was ¼" plexiglass plate. Each wall section was of ½" plexiglass plate and was 2" in height. With this height and an inlet width, b, of ½" the aspect ratio is four to one. Selection of this aspect ratio and height was based on examination of the results presented by Han [9]. According to Han, for this aspect

ratio the flow in the midplane of the inlet would be nearly two-dimensional.

The nature of the cavity flow was unknown before testing. Testing has shown that the jet flow in the central cavity region remains largely two-dimensional. However, three-dimensional effects were visible in the test section under certain conditions. In particular, the following cases were observed.

a. In the recirculation regions dye initially on the midplane might move in the vertical direction at points where two flow patterns intersected. For example, such a point occurred for low Reynold number cases where the main recirculation flow intersected the main jet flow.

b. In the boundary layers in the splitter region the flow became three dimensional. Although visible in some cases, this boundary layer migration near the splitter edge had little effect on the centerline flow.

c. Some combination of heating from the lighting for the photographs and positioning of the storage reservoirs caused a distinct vertical bow in the main jet flow. The exact cause of this bow was not determined. By minimal use of the lighting and by maintaining the reservoirs at least several inches above the model, the problem was avoided altogether.

The base plate was a 22" x 51" rectangular plate of ½" plexiglass. Due to the leakage problem it was necessary to mount this

plate on a flat solid base. As shown in Fig. 3.1, the base plate and model rest on an angle iron table frame. Across the top of this frame were placed a series of 2" x 4" boards, with each board resting on its 2" edge. These were planed flat before installation and shimmed on mounting to produce a flat base. The plexiglass base plate was mounted on this base.

The model itself consisted of a screen section, converging nozzle section, inlet section, test section, and two outlet sections. The flow entered the screen section through two ¾" holes in the plexiglass end plate. The screen section was 12" wide by 6¾" long and contained 5 wire mesh screens, as shown in Fig. 3.3b. Three of these screens were of 30 x 40 mesh brass screen and two were of 40 x 60 mesh brass screen. Each screen was cold soldered on a 2" x 12" rectangular frame made of brass brazing rod. Each end of this frame was supported in a slot machined in the plexiglass side walls. The purpose of the screens was to damp out disturbances and thus produce a very low turbulence inflow.

Disturbances were further damped by a smooth acceleration through a highly converging nozzle, as shown in Fig. 3.2 and Fig. 3.3b. This nozzle was formed by two sine curves machined in plexiglass blocks. The flow area changed continuously from 12 inches by 2 inches to ½ inch by 2 inches, a 24 to 1 nozzle ratio.

The converging nozzle was followed by a ½ inch wide inlet channel. This section had a length of 20 inches. According to Han's calculations [9], this length would provide fully developed

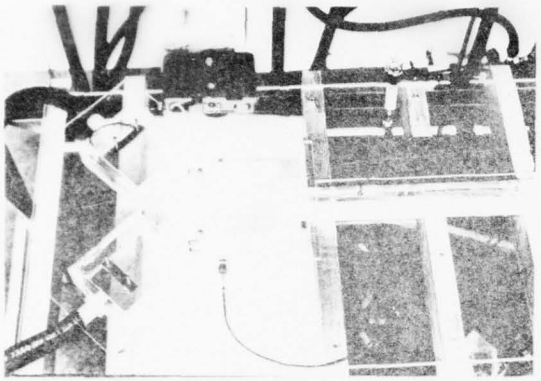

a) Test Section Region of Model

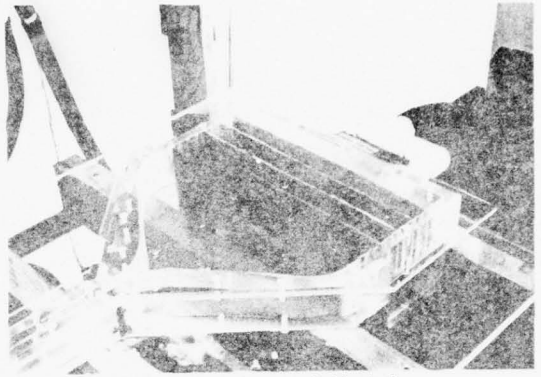

b) Inlet Region of Model

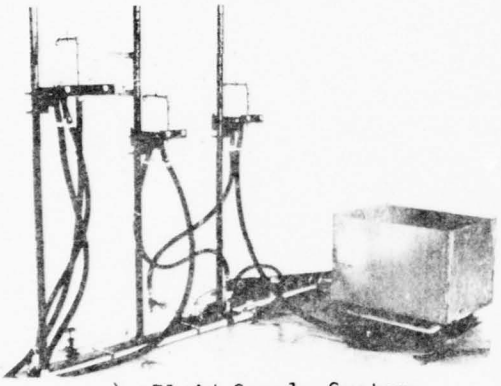

c) Fluid Supply System

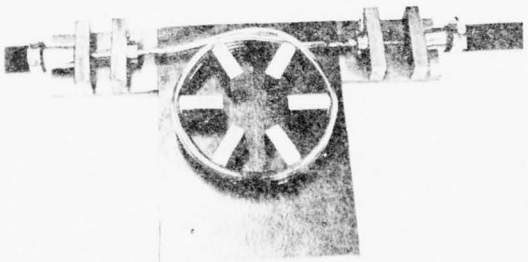

d) Flow Meter

Figure 3.3. Details of Experimental Equipment

profiles at the inlet to the test section. These inlet profiles were expected to be fully developed for Reynolds numbers up to approximately 500.

The test section was in the exact shape of the region modeled in the computer simulation and is visible in Fig. 3.3a. The cavity region was a 5 inch square. The receiver outlets were rounded to provide a smooth transition into a relatively large outlet section ($4\frac{23}{64}$ inches by 5 inches). This configuration minimized the downstream effects on the receiver outlet flow. The flow left each outlet section through a $\frac{3}{4}$ inch diameter hole positioned in the center of the wall opposite each receiver outlet.

Provisions were made on the model for the mounting of dye injection fittings, which will be described later, and air bleed fittings. Except as noted later, these fittings were mounted in holes drilled in the cover plate. The bleed holes were positioned at corner points in the test and outlet sections and were used to remove air trapped under the cover plate when filling the model with fluid.

## C. Fluid Supply System

Flow to and from the model was controlled through movement of a system of reservoirs. The actual flow through the model depends on the height, or pressure, differential between the feed reservoir and the two outlet reservoirs. This pressure differential was changed by vertical movement of one or more of the reservoirs. The overall arrangement is shown in Fig. 3.3c.

The feed reservoir, the larger reservoir on the left in Fig. 3.3c, had a second purpose. It served to shield the flow to the model from disturbances created by the pump which forced the fluid to the level of the feed reservoir. The feed reservoir acted as a stilling chamber.

All three reservoirs were rectangular boxes made of ½ inch and ¼ inch plexiglass. The plexiglass sides and base were milled and fastened together with nylon machine screws. All joints were then sealed through use of ethylene dichloride to form a chemical bond between mating plexiglass ports. All three reservoirs were divided into two compartments by a vertical wall, or wier. One compartment in each reservoir drained back to the storage reservoir and on typical runs was nearly empty.

In the feed reservoir the main compartment had two ports. The flow from the supply pump entered through one port and left through the other port to flow to the model. Excess fluid from the supply pump flowed over the wier and back to the storage reservoir. The head, or level, in the reservoir was thus fixed at the level of the top of the wier.

The reservoirs were supported by the guide bracket, cable, and pipe arrangement shown in Fig. 3.3c. The pipe frame was of 1¼ inch diameter standard steel pipe. One end of each pipe was flanged to the floor and the other end is flanged to a section of 4 inch steel channel. The frame was further supported by sections of ¾ inch pipe which connect the vertical 1¼ inch pipe to the room wall.

The guide brackets slid vertically on the 1¼ inch pipe and served to position the reservoirs in the horizontal plane. The weight of the reservoirs and guide brackets was supported by 3/16 inch plastic coated tiller cable, which is visible in Fig. 3.1. Each of these cables ran from the guide bracket and reservoir through the upper channel, over two rollers mounted in the channel, and down the other side of the 1¼ inch pipe. At the floor the cable makes a 180° turn through a cable pulley and was clamped to itself with a cable clamp. Loosening of this clamp allowed coarse adjustment of reservoir height. Fine adjustment was provided by a turnbuckle which was mounted between the tiller cable and the reservoir guide bracket. One full turn of this turnbuckle moved the reservoir vertically approximately 0.1 inches.

Flow between the reservoirs, model, pump, and storage reservoirs is through 1 inch Gates heater hose where the line must be flexible and through 1 inch PVC pipe where a solid line was acceptable. The fluid was pumped from the storage reservoir to the feed reservoir by a Model DH11 Eastern Industries centrifugal pump.

## D. Instrumentation

The measurement of the flow rate was complicated by the small flow rates involved. It was decided to construct a flow section across which the pressure drop could be easily measured and correlated with the flow rate. The resulting design is shown in Fig. 3.3d. The design consisted of two brass nozzles connected by a length of ¼

inch I.D. tygon tubing. The tubing length was set to yield a suitable pressure drop for the flow range expected. The pressure drop was measured on a manometer board having a range of 1 to 12 inches of water.

Calibration for a given fluid and length of tubing was accomplished easily. The meter was connected in a line between the feed reservoir and one of the outlet reservoirs. These reservoirs were then adjusted to produce different flow rates. Each flow rate produced a different pressure drop, which was recorded along with the flow rate. To determine the flow rate, the flow from the outlet reservoir to the storage reservoir was diverted for a measured period of time and collected in a pail. The collected fluid was weighed on a balance beam scale, which measured in increments of 0.01 lb. The time period was measured with a stopwatch, which measured in increments of 0.01 minutes. The weight flow rate was then calculated by dividing the fluid weight by the measured time. Typical runs were for five to ten minutes and collected between 2 and 6 pounds of fluid. Calibration curves for the flow meters used are shown on Fig. 3.4. These curves are for water at approximately 73°F. During the experiments the temperature varied slightly from this temperature (±3°F), but the effect of this variation on the flow rates measured would be small and was ignored.

Two flow meters were used to obtain the inlet and one of the outlet flows. The other outlet flow was taken as the difference between these two measured flows.

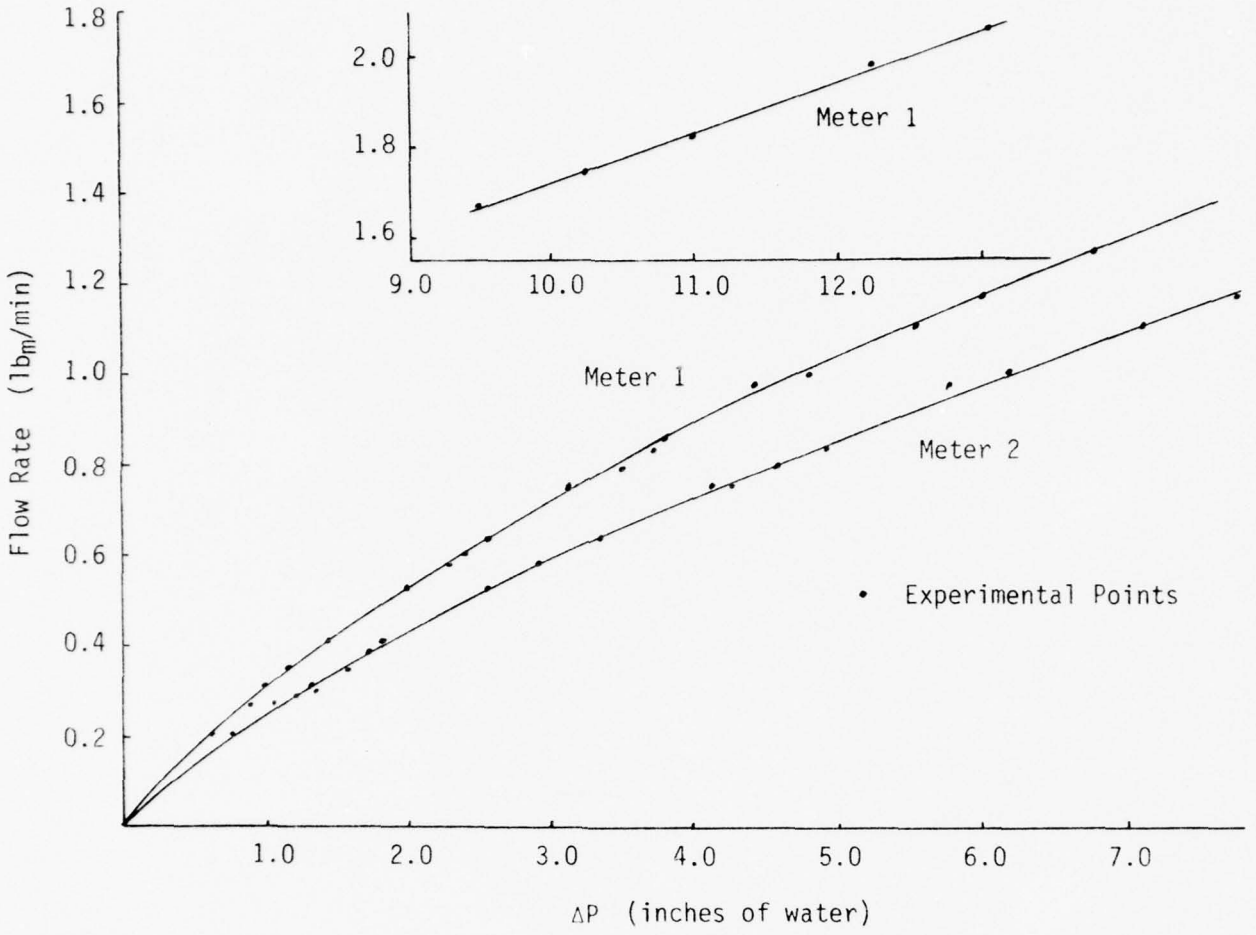


Figure 3.4. Flow Meter Calibration Curves

Once the flow rate was determined it had to be related to the inlet Reynolds number used in the computer solutions. The average velocity in the inlet channel, $U_{3\text{-}D}$, is given by the volumetric flow rate, Q, divided by the channel area, $A_c$. From Han's calculations [9], the centerline velocity, $u_0$, for a channel with an aspect ratio of four is

$$\frac{u_0}{U_{3\text{-}D}} = 1.7728 \quad . \tag{3.1a}$$

At the horizontal midplane the velocity profile is parabolic with a maximum velocity of $u_0$. For the computer solutions the velocity on which the Reynolds number was based was the average velocity of a two dimensional parabolic profile for which

$$u_0 = 1.5\ U_{2\text{-}D} \tag{3.1b}$$

Therefore, the velocity for use in the Reynolds number is

$$U_{2\text{-}D} = \frac{u_0}{1.5} = 1.182\ U_{3\text{-}D} \quad . \tag{3.1c}$$

Then,

$$U_{2\text{-}D} = 1.182\ \frac{Q}{A_c} \tag{3.1d}$$

and

$$Re = \frac{1.182\ Q}{h\nu} \tag{3.1e}$$

where h is the height of the inlet channel.

As mentioned earlier the flow visualization was accomplished by injecting dye into the flow. Initially there was some concern that the needles used for injecting the dye would disturb the flow patterns. For this reason the hydrogen bubble flow visualization technique [26] was investigated. This technique involves generating hydrogen bubbles by the hydrolysis of water on a small wire placed in the flow. The size of the wire is such that the disturbance to the flow would be minimal. The hydrogen bubbles are swept off the wire and their movement indicates the flow patterns. Unfortunately it was found that for the low flow rates considered in this study the bubbles would rise and collect beneath the cover plate. It was expected that the bubbles would go back into solution, but this was not the case, and the hydrogen bubble technique was abandoned. Dye injection was then examined and it was found that the injector did not noticeably disturb the flow field.

The fluid used for the flow visualization was water. The temperature was measured using a standard mercury thermometer. The fluid properties were then taken as those of pure water at this temperature. This introduces some error into the Reynolds number determination because the water is not pure. However, the desired results are qualitative and it was felt that this error is not significant.

The dye chosen was a mixture of red and green food coloring and water, proportioned to produce a dark navy blue or black color. The dye was mixed at the time of each experiment with water taken

from the storage reservoir. This insured that the dye and the water in the flow were at the same temperature and thus would have approximately the same density.

The dye was introduced into the flow through two separate injectors. In one injector the dye was injected through a 0.032 inch O.D. by 0.020 inch I.D. tube which was held in place by soldering it into a hose fitting. The tube, which was mounted vertically, had one end bent in order that the dye would be injected horizontally and at the model midplane. This injector was mounted such that dye was introduced into the inlet channel approximately 3 inches from the test section.

The second injector was similar in construction to the first except that the tube was not bent. This injector was mounted in a side wall of the test section such that the tube lay completely in the horizontal midplane. The tube was held in place in such a way that it could be easily moved in a direction normal to the wall. This allowed visualization of recirculation streamlines over the entire recirculation region.

For both injectors a $\frac{1}{16}$ inch I.D. tygon tube was attached to the injector and extended to a fitting which was soldered to a hypodermic needle. The hypodermic needle was placed on a syringe which contained the dye. The dye could then be injected into the model in two ways. It could be injected by simply forcing the syringe plunger by hand. Alternatively, the syringe could be elevated, say by supporting it with a ringstand, and for the proper

elevation the dye would be forced into the flow through a combination of the weight of the dye and of the syringe plunger.

E. Photographic Equipment

The streamlines shown by the dye patterns were recorded on film. The main considerations were the choice of a camera and the method of lighting.

The camera chosen was a Canon Canonet QL 17. This model is a single lens, 35 mm camera, with this particular one having a 1:1.7 lens. A +3 close-up lens was used in conjunction with the camera.

The camera was mounted above the model on a horizontal support fixed to one of the pipes in the reservoir support frame. The support was an aluminum tube which formed a cantilever beam extending over the model. The height of the beam above the model was controlled by the area desired in the picture, the close-up lens used, and the footage setting on the camera. For the +3 lens, a footage setting of 15 feet, and a desired coverage of a 10" by 7" area, the height from model midplane to lens was 12¼ inches.

The lighting was furnished by a single 500 watt photoflood bulb mounted in a standard circular reflector. This was centered directly below the test section and positioned approximately 28 inches below the test section midplane. This strong beam of light was diffused by passage through a diffuser made of vellum paper. The diffuser was positioned 4 inches below the model.

F. Comments on Experimental Procedure

Use of the above equipment, excluding the photographic equipment, was rather straightforward. The photographic equipment also was not complex as long as standard directions for the respective pieces of equipment were available and followed. The general procedure for use of each piece of equipment should be apparent from the description of the equipment.

There were, however, several experimental techniques which are worthy of mention. These were as follows:

a. Care had to be exercised to insure that all the air had been removed from the model and the supply lines. This problem was alleviated by inclining the model as it filled with water. This allowed the air to rise to the bleed holes. Trapped air could be eliminated from the supply lines by making sure that the high points in these lines were points at which air could be bled.

b. The feed and outlet reservoirs interacted in their effect on the flow rate. For example, blocking one receiver would not result in all the previous flow going through the other receiver. Instead, the receiver flow rate would increase and the inlet flow rate would decrease. Thus, some manipulating was necessary to obtain the desired flow rates when changing from one combination of flow rates to another.

c. The time constants of this system were rather long. Thus, after changes in flow rates, a sufficient period of time had to be allowed for the system to come to equilibrium. For low Reynolds numbers this time period was commonly 15 minutes.

d. The injection of dye was somewhat of an art. Once a flow pattern was established, several attempts at obtaining a suitable dye pattern might be required. Also the dye patterns were not extremely stable and could easily be effected by vibration of the model or even overheating from the lighting for the camera, as mentioned earlier.

## G. Sample Result

A typical result for the dye injection studies is shown in Fig. 3.5. Here the flow had a Reynolds number of 100, which corresponds to an average inflow velocity of 0.3 inch per second. The dye was injected to illustrate the center streamline for a symmetric case.

Figure 3.5. Typical Flow Visualization

# CHAPTER IV

## DISCUSSION OF RESULTS

The numerical model developed in Chapter II was used to predict the flow fields and pressure distributions for a variety of flow situations. Variations were made in Reynolds number, receiver flows, and deflection of the inlet jet. The resulting flow and pressure distributions will be presented and discussed in this chapter. In addition, streamline photographs were obtained using the experimental apparatus discussed in Chapter III for three of the cases including asymmetric loading. These photographs will be compared to the corresponding numerical streamline predications.

One of the projected uses of the numerical model is as a design tool in obtaining characteristic curves, as mentioned in Chapter I. Generation of such a curve is described and an example presented. This is followed by discussion of the experimental observation of edgetone oscillations. The chapter concludes with several comments on numerical characteristics of the computer model itself.

### A. Flow Field Results for the Undeflected Jet

The predicted flow fields are conveniently presented as contour plots of the stream function values. Such a plot is shown in Fig. 4.1. Each solid line in Fig. 4.1 represents a line of constant

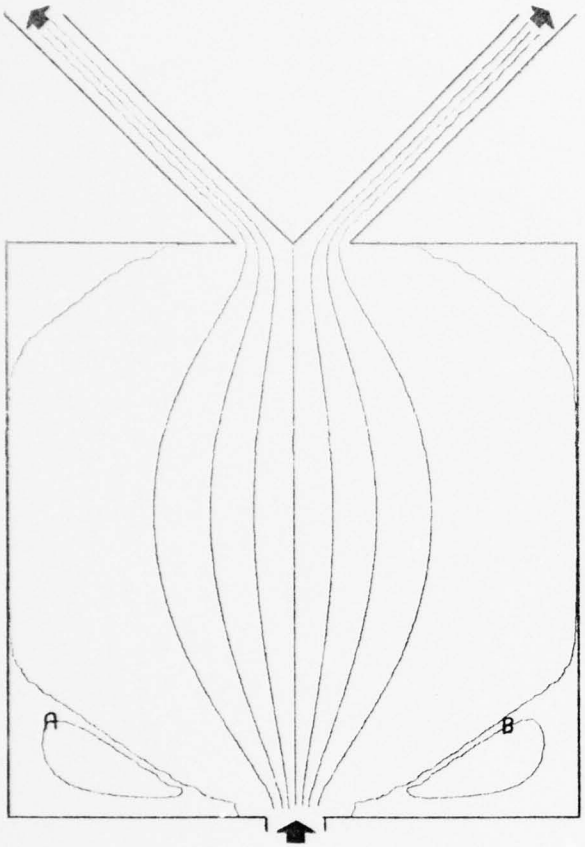


Figure 4.1. Stream Function Distribution

Re = 1 $Q_1 = 0.5\ Q_s$ $\phi = 0^o$

| Symbol | Value |
|---|---|
| A | 0.001 |
| B | -1.001 |
| C | 0.100 |
| D | -1.100 |
| E | 0.200 |
| F | -1.200 |
| G | 0.300 |
| H | -1.300 |
| I | 0.400 |
| J | -1.400 |
| 1 | -0.001 |
| 9 | -0.999 |

Table 4.1. Stream Function Values

$\psi$, i.e. a streamline. Each streamline divides the flow into separate regions since flow is tangent to a streamline. Thus, the 0 and -1.0 streamlines bound the inflow from the inlet nozzle and represent lines of separation between the flow entering the cavity and the flow which remains in the recirculation regions. In the main flow the streamlines vary by increments of 0.125. In the recirculating flow the streamlines are labeled, with the corresponding values for $\psi$ presented in Table 4.1.

As denoted by the arrow, the flow enters the amplifier through the single port in the lower boundary. For the flow shown, which has a Reynolds number of 1, the jet spreads as it crosses the cavity and, due to the strong diffusion effect at this Reynolds number, occupies most of the cavity region. The flow is almost stagnant in the upper cavity corners and in the lower corners the jet drives two small vorticies, or recirculation regions. The velocities are relatively large in the central cavity region, where the x-gradient of $\psi$ is relatively large. The velocities are much lower on the edges of the main flow and in the recirculation regions. In both cases this is indicated on Fig. 4.1 by the small spatial gradients in $\psi$ in these regions. In Fig. 4.1 one half of the flow exits through each receiver. Since the flow is initially undeflected, the stream function distribution is symmetric.

A series of such symmetric flows is shown in Fig. 4.2. In this series the Reynolds numbers are respectively 20, 100, 275, and 1000. Increasing the Reynolds number, $Ub/\nu$, corresponds to

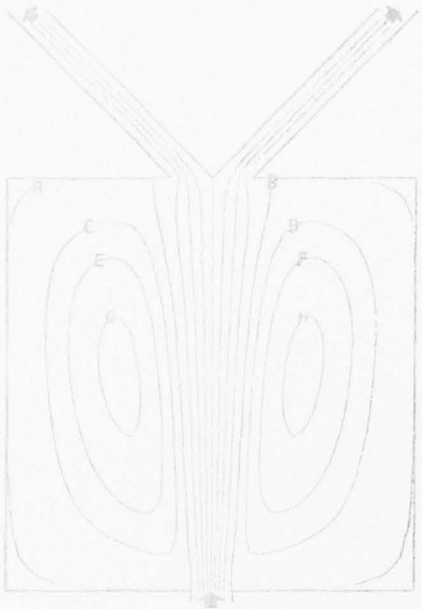

a) Re = 20

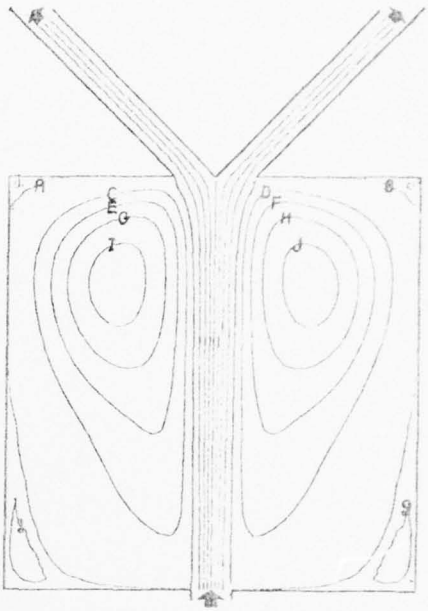

b) Re = 100

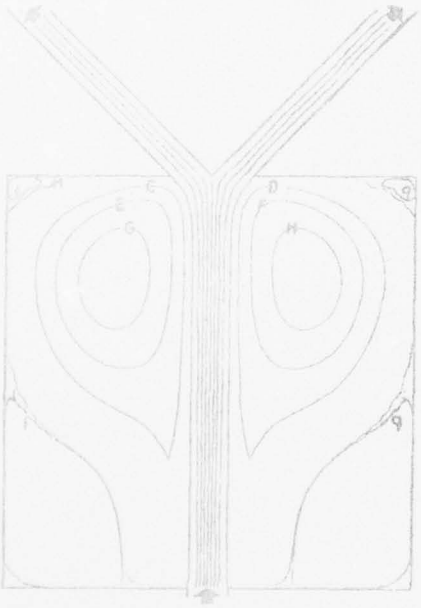

c) Re = 275

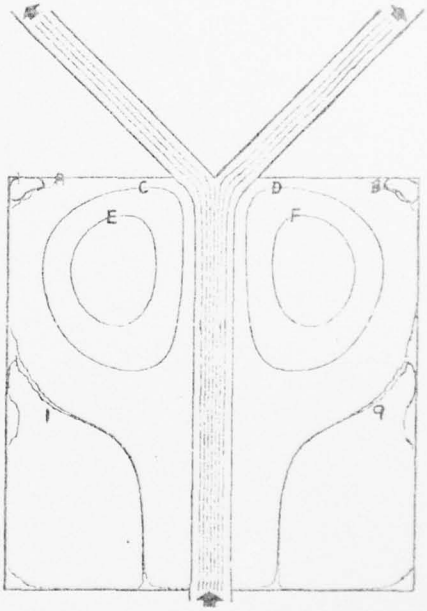

d) Re = 1000

Figure 4.2. The Effect of Reynolds Number on the Flow Field

$Q_1 = 0.5\ Q_s \quad \phi = 0^o$

increasing the average inlet velocity, U, or decreasing the kinematic viscosity, ν. Both interpretations imply that the importance of diffusive effects on the flow is reduced and that the flow becomes dominated by the convective terms in Eq.(2.6). As pointed out for Re = 1, Fig. 4.1, the inlet flow spreads to the width of the cavity region. For Re = 20 and higher, Fig. 4.2, the spread of the main flow becomes progressively less.

For Re = 20 the main flow has sufficient momentum to drive one large recirculation region in each half of the cavity. For Re = 100 the velocities in the recirculation vortex become larger and the recirculation vortex begins to drive secondary vorticies in the cavity corners. In Figs. 4.2c and 4.2d the higher momentum in the main flow is sufficient to drive progressively larger secondary vorticities, in keeping with what might be physically expected. In other words, the total momentum of the entire region is increased and the non-dimensional plots indicate the redistribution of this momentum among the recirculating vorticies.

As will be discussed in Section F, the flow pattern for Re = 1000 was not experimentally obtainable due to edgetone oscillations. It is included to show that the numerical method was stable at this relatively high value for Reynolds number. The upper bound on Reynolds number before the onset of oscillation with the particular experimental apparatus used in this study is roughly 275.

An alternate method of presenting the flow field results is to plot velocity distributions for different sections in the

amplifier. Such a plot is shown in Fig. 4.3a. This is a v-velocity profile along a line which is normal to the amplifier centerline at the $30^{th}$ node ($1 \leq i \leq 41$, $j = 30$), which corresponds to a y-distance of 7.25. The v-velocities are plotted for three Reynolds numbers (275, 100, and 20), all symmetric flows. Again the effect of increasing Reynolds numbers is clearly visible. For the higher Reynolds numbers the velocity profile has narrowed and a higher centerline velocity has been maintained. The momentum of the inlet flow has not diffused as rapidly into the sides of the cavity region.

Another effect of diffusion is visible in Fig. 4.3b. The profiles shown are the v-velocities for $1 \leq i \leq 41$ and $j = 39$, which is just before the flow impinges on the splitter and is located at a y-distance of 9.5. For the low Reynolds number profile the presence of the splitter feeds back upstream, a diffusion phenomenon, and causes the velocity profile shown, with the centerline velocity being a local minimum. This is not observed for the higher Reynolds number flows. Although a velocity reduction is observed, the domination of the flow field by convection prevents any distortion of the profile.

The fourth profile plotted on Fig. 4.3a is that for a laminar free jet. Such a jet profile might be used in conjunction with the cowl streamline method [11]. The profile is based on Schlichting's analysis of a laminar free jet [25]. The constants have been evaluated so that the profile is non-dimensional. It also has the same momentum and maximum velocity at the amplifier inlet as the numerical

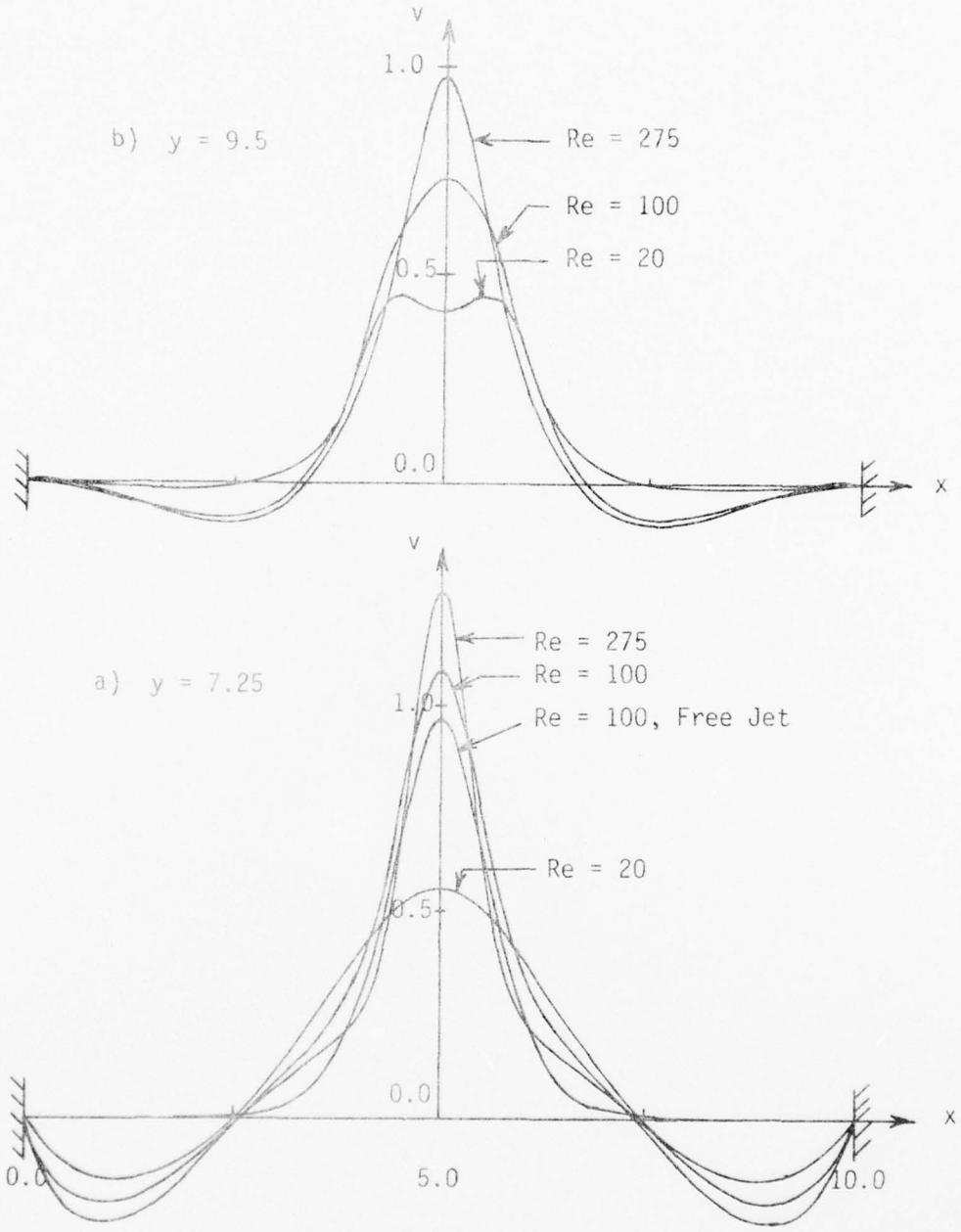


Figure 4.3. Predicted Velocity Profiles in the Cavity Region

solutions. The laminar jet profile is for a Reynolds number of 100 and thus can be compared to the Re = 100 velocity profiles from the numerical results.

It was not expected that the profiles would match, since it is assumed in the derivation of the laminar jet profile that the jet exhausts into an infinite medium and that its momentum is constant. However, the general shapes are similar, with the free jet having a lower velocity at all points in the central flow region. Thus, for the central region the momentum of the amplifier flow did not remain constant; it increased. This indicates that the positive v-velocity component of the recirculation flow tends to increase the momentum of the main flow, even though the main flow is driving the recirculation flow. Thus, the confinement of the jet by the amplifier walls concentrates the positive y-momentum flux in the central flow region.

A further comparison of velocity profiles is shown in Fig. 4.4. This plot illustrates the centerline velocity decay for the three Reynolds numbers and for the free laminar jet with Re = 100. As the Reynolds number is increased the viscous effects on the main flow are reduced, which results in the centerline velocity remaining high. Again, the laminar free jet velocity decays more rapidly than the corresponding amplifier flow velocity profile due to the effect the recirculation regions have on the main flow.

As discussed in Chapter III, an effort was made to obtain experimental verification of the predicted flow fields. Flow field photographs were obtained for two of the symmetric cases, Re = 100

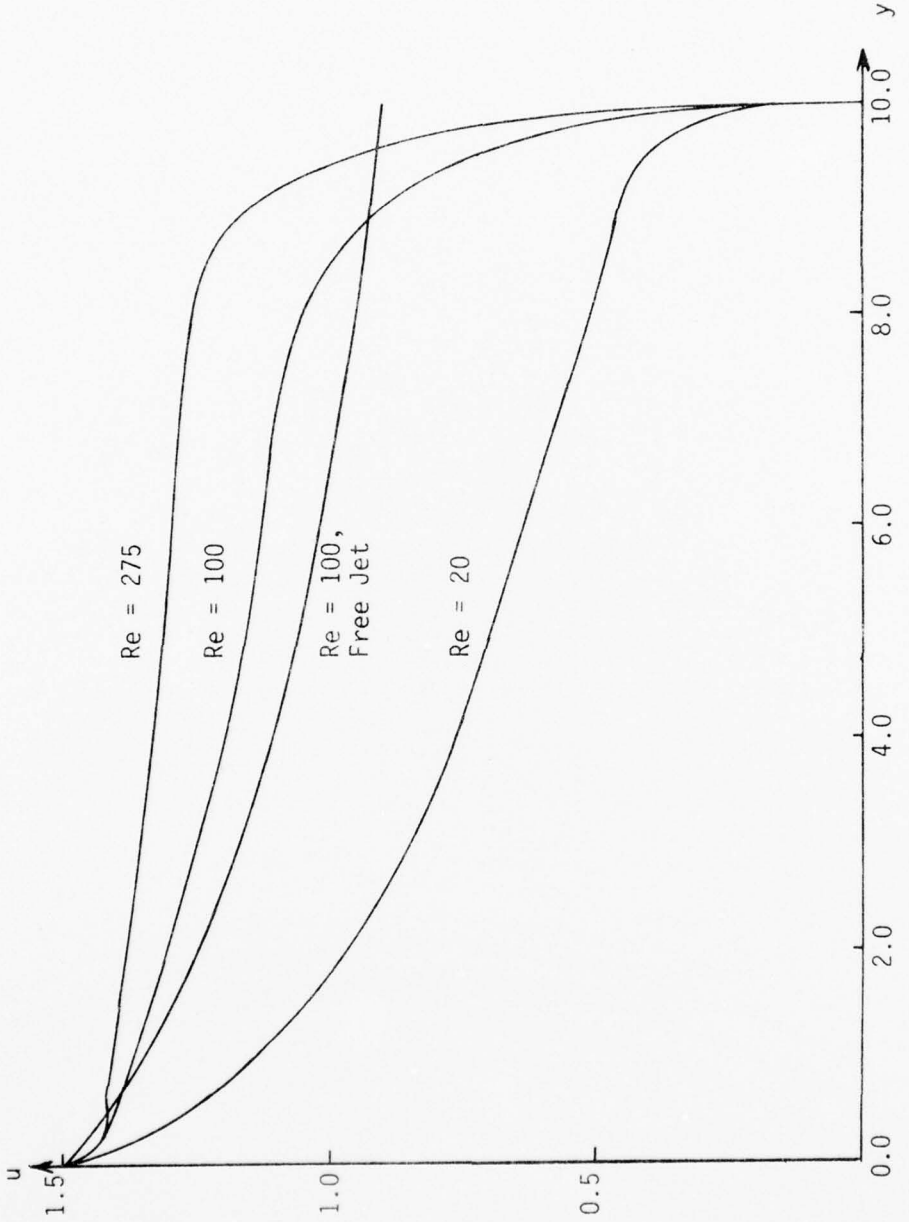


Figure 4.4. Centerline Velocity Decay

and Re = 20, and for one unsymmetric case. The latter case will be presented later in this chapter.

A photograph of the flow for Re = 100 is presented in Fig. 4.5 along with the corresponding numerically predicted streamline pattern. This visualization was obtained by injecting a large amount of dye into the cavity region, disrupting the flow pattern, and allowing the flow pattern to redevelop. Except for the large concentration of dye located on the base plate near the splitter, this technique worked well. All the dye is certainly not on the midplane, but the flow pattern is evident. The dye concentration mentioned above had settled into the lower boundary layer and had not had time to wash out when the picture was taken. The center streamline is on the midplane and slightly off center horizontally. It is a continuous stream being injected through a needle, the injection technique described in Chapter III.

A comparison between (a) and (b) of Fig. 4.5 is felt to be excellent qualitative verification of the computer flow solution. In Fig. 4.5b the boundaries of the main flow are clearly indicated, as is the flow pattern in the main recirculation region.

Details of the flow shown in Fig. 4.5b were obtained on the photographs shown in Fig. 4.6. Again, these compare well with the stream function plot in Fig. 4.5a. For Fig. 4.6 dye was injected into the cavity midplane through the needle which was extended from the left wall. This needle was repositioned between each picture to produce the different streamlines shown.

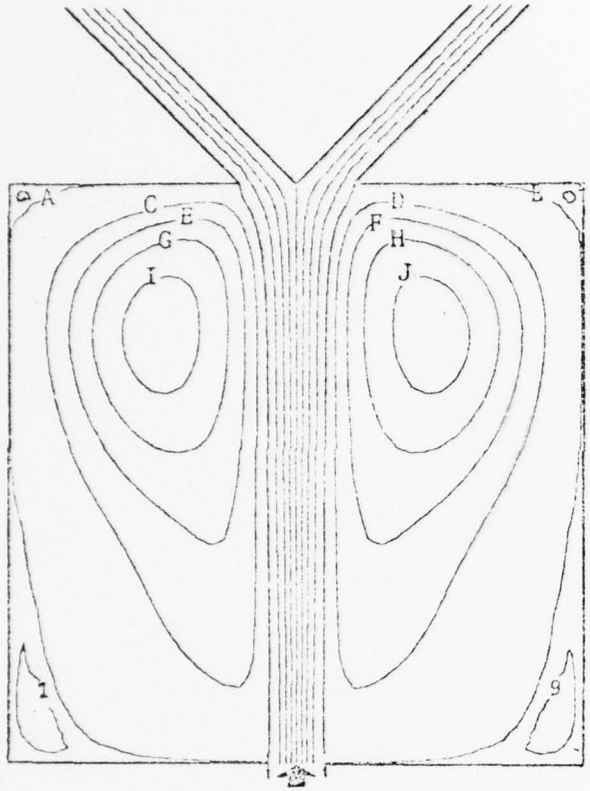


a) Numerical Results

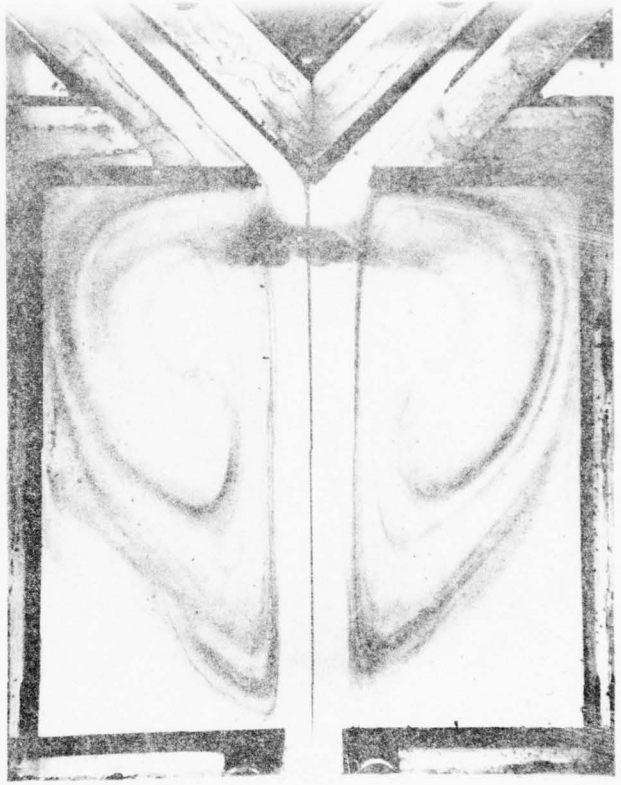

b) Flow Visualization

Figure 4.5. Comparison of Numerical and Experimental Flows

Re = 100 $Q_1 = 0.5\ Q_s$ $\phi = 0°$

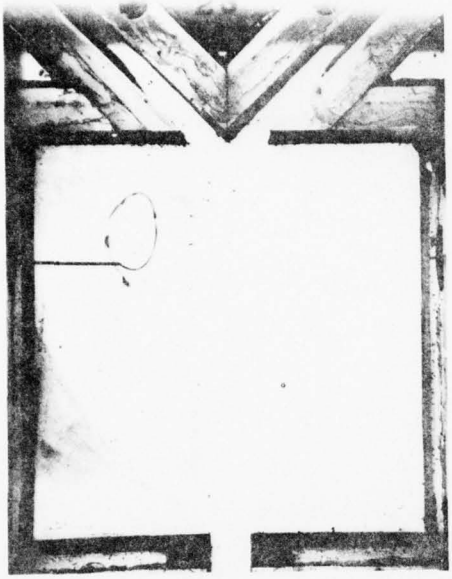

a) Central Vortex Region

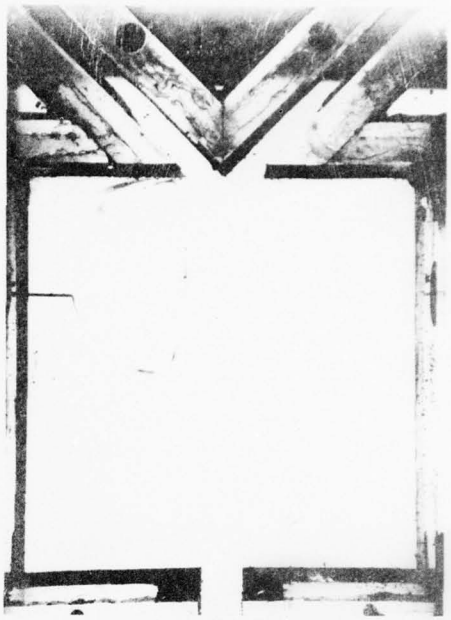

b) Main Recirculation Region

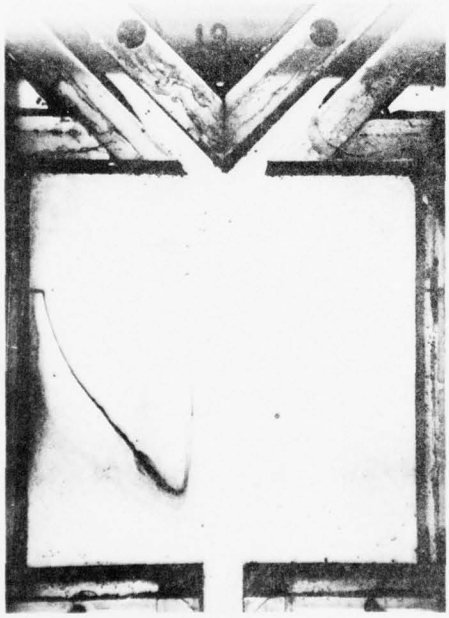

c) Lower Recirculation Region

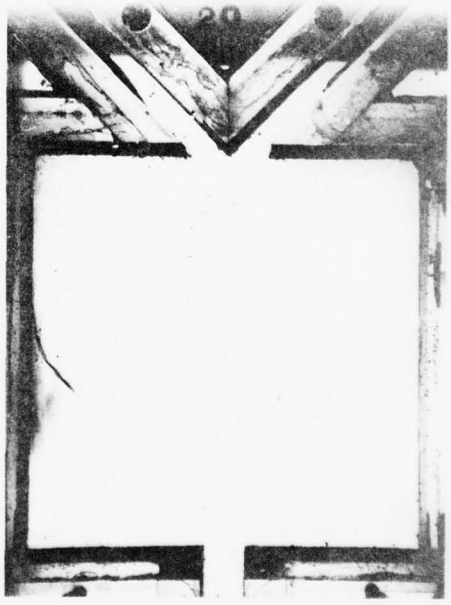

d) Wall Separation

Figure 4.6. Individual Streamlines for Re = 100

Figure 4.6a shows a central vortex streamline which completes a closed vortex loop. Figure 4.6b shows another recirculation streamline which is farther from the center of the vortex. In. Fig. 4.6c the streamline shown is in a region of very slow flow and most of the main recirculation flow moves between the position of this streamline and the center of the vortex. The streamline shown in Fig. 4.6d marks the point where the recirculation pattern separates from the wall. The flow illustrated here was extremely slow and the streamline would not extend farther into the flow field without falling into the lower boundary layer and/or diffusing. This is consistent with the low velocities indicated in Fig. 4.5a. Further details on this flow field will be presented later in conjunction with comparisons between symmetric and unsymmetric flows for Re = 100.

A comparison similar to that of Fig. 4.5 is made in Fig. 4.7 for the symmetric case with Re = 20. For the experimental model used, having b = 0.5 inches, the flow rate at this Reynolds number was extremely low, 0.12 $lb_m$/min. For reference, at this flow rate it takes 70 minutes to fill a one gallon container. The low velocities of the flow made the visualizations difficult to obtain.

In Fig. 4.7b the flow pattern in the right cavity was obtained by flooding this portion of the cavity with dye and then allowing the flow pattern to redevelop. In the left cavity region an individual streamline is shown. Due to the low velocities and slight density differences involved, this streamline began to settle toward the base plate after traveling the distance shown.

AD-A047 057 TEXAS UNIV AT AUSTIN DEPT OF MECHANICAL ENGINEERING F/G 13/7
A BASIS FOR NUMERICAL MODELING OF FLUID AMPLIFIERS
FEB 76 HEALEY, A. NICHOLSON, J. 162P
UNCLASSIFIED CONTRACT NO. DA-ARO-D-31-124-73-G115 ARO 10927.5-E N/L

2 OF 2
AD
A047 057

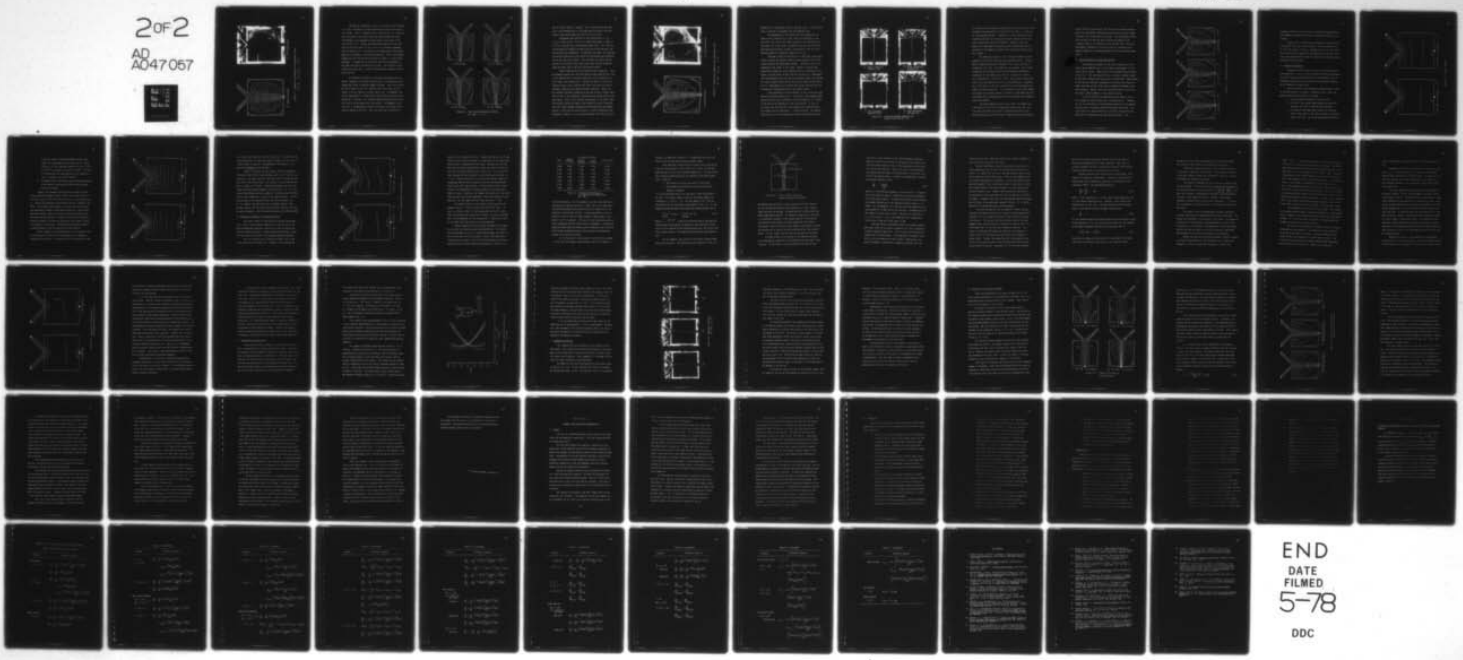

END
DATE
FILMED
5-78
DDC

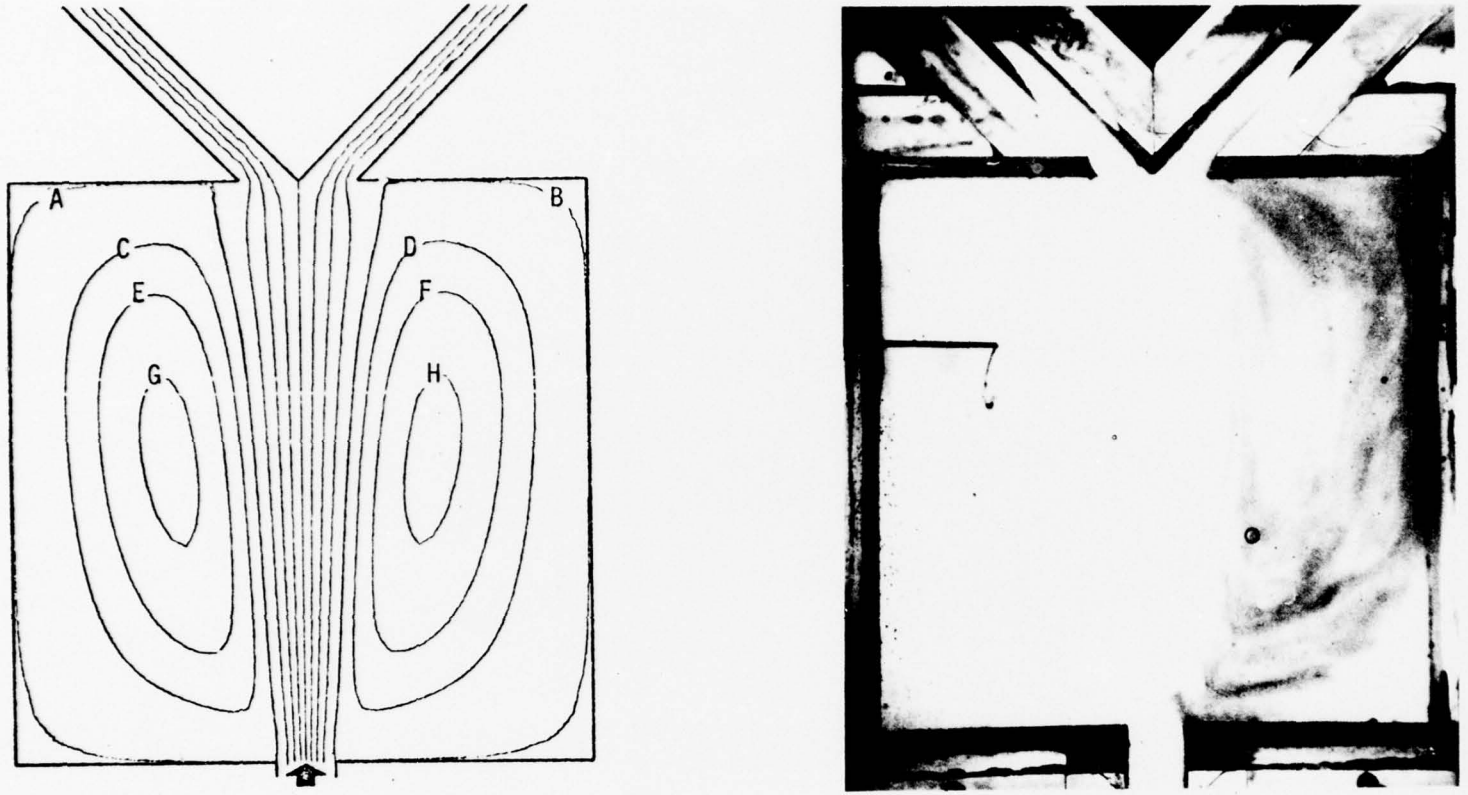


a) Numerical Results

b) Flow Visualization

Figure 4.7. Comparison of Numerical and Experimental Flows

Re = 20 $Q_1 = 0.5\ Q_s$ $\phi = 0°$

Although the streamlines in Fig. 4.7b are not as well defined as in Figs. 4.5b and 4.6, several observations about the flow field can be made. First, in comparing Figs. 4.5b and 4.7b, it is observed that the center of the vortex region has moved towards the inlet. This movement is in agreement with the contour plots shown in Fig. 4.5a and Fig. 4.7a. Second, the recirculation pattern in the right half of the cavity region in Fig. 4.7b is in qualitative agreement with the contour plot. In particular, the experimental vortex center appears to be located in the position predicted. Third, the boundary between the main flow and the recirculation region is in qualitative agreement. In comparison to the Re = 100 case, the jet boundary in the right half cavity has moved to the right. This implies a larger spread of the main flow: a result of the relative increase in diffusion at Re = 20.

As discussed in Chapter II, provisions were made in the numerical simulation for varying the flow rates in the receivers while keeping the inflow, or Reynolds number, constant. Such a series with Re = 100 is shown in Fig. 4.8. Here the flow rate in the left receiver is 0.5 $Q_s$, 0.625 $Q_s$, 0.750 $Q_s$, and 1.0 $Q_s$. The dominant feature of these plots is a progressively larger shift of the main flow boundaries to the left. This would be expected because progressively more flow is moving through the left receiver. The movement of the main flow is accompanied by a shift of the center of the main recirculation regions to the left. Also, the total mass circulating in

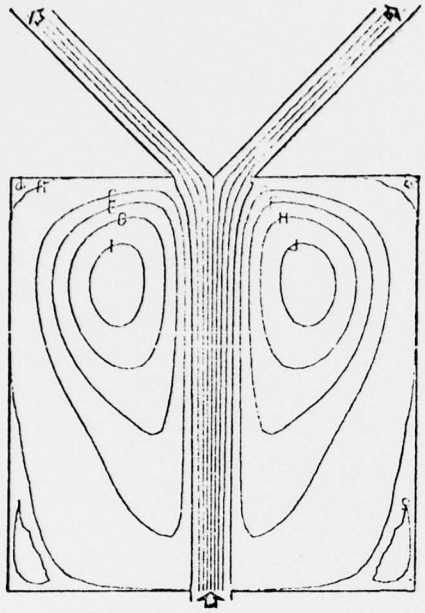

a) $Q_1 = 0.5\ Q_s$

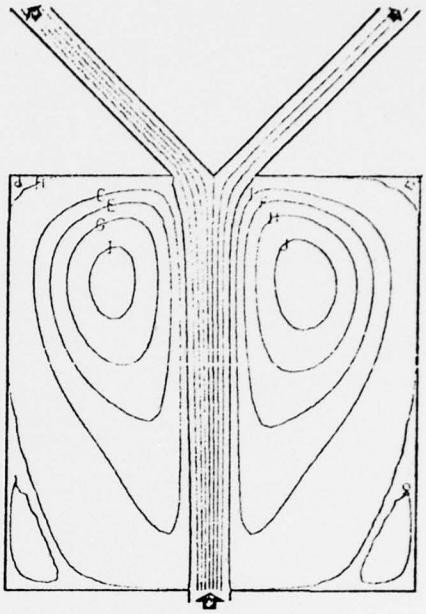

b) $Q_1 = 0.625\ Q_s$

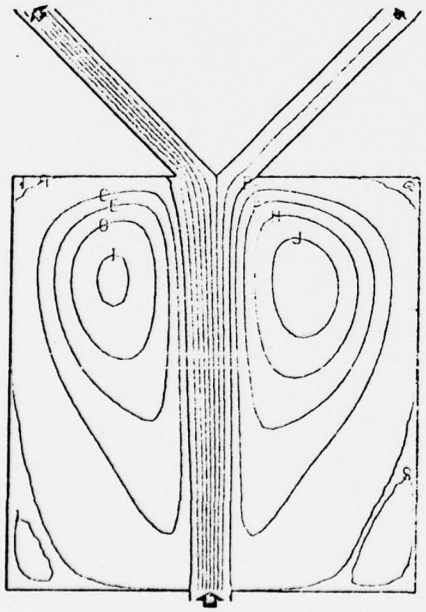

c) $Q_1 = 0.750\ Q_s$

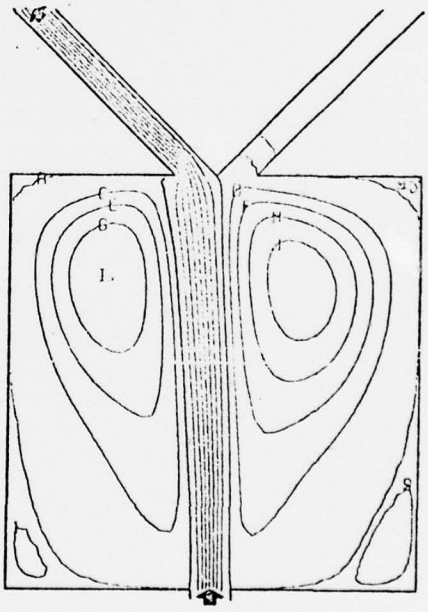

d) $Q_1 = 1.000\ Q_s$

Figure 4.8. Flow Fields with Unequal Outflows
Re = 100 $\phi = 0^{\circ}$

the left vortex region is reduced. This is indicated by the reduction in the maximum value of the stream function found in the left vortex as the series progresses from Fig. 4.8a to 4.8d.

Photographs were obtained for the blocked case, i.e. $Q_L$ = 1.0 $Q_S$, in this series. The first of these photographs is shown in Fig. 4.9, along with the corresponding contour plot. This visualization was made by flooding the region with dye and waiting until the flow patterns had redeveloped. In addition, more detail was obtained by injecting from the left wall while the flow pattern was redeveloping in the right cavity region. This resulted in a poorly defined pattern in the central vortex region and a well defined streamline along the lower edge of the main recirculation region.

Several observations can be made from this comparison. First, the boundary between the right recirculation region and the main flow is well defined and its location agrees well with the numerical results shown in the contour plot. Second, the centers of the recirculation regions can be inferred and, within the limits of such an inference, agree with the center locations predicted. Third, the well defined individual streamline in the left cavity is almost identical to one of the streamlines indicated on the contour plot for the same region. Fourth, near the main flow boundary in the lower right recirculation region the shape of the streamlines can be visualized. Again this shape compares favorably with the predicted flow pattern. Finally, a flow into the right receiver is faintly indicated on the photograph. However, it is not certain whether this flow was on the

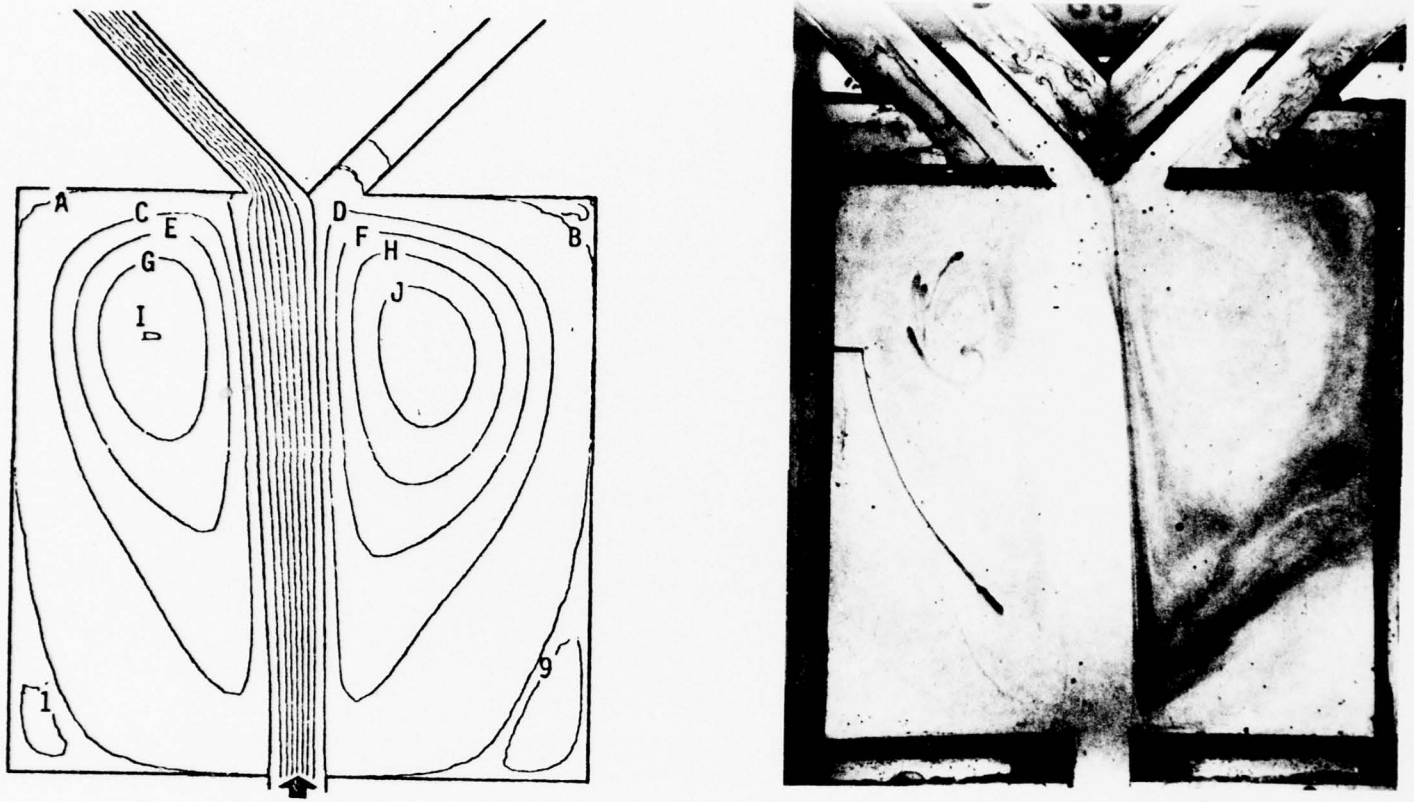


a) Numerical Result

b) Flow Visualization

Figure 4.9. Comparison of Numerical and Experimental Flows

Re = 100 $Q_1 = Q_s$ $\phi = 0°$

midplane or in the boundary layer on the base plate. If on the midplane it would be in agreement with the predicted flow.

Two photographs of flow details for the blocked case are shown in Fig. 4.10b and Fig. 4.10d. Both are streamlines in the main flow. One, Fig. 4.10b, shows the center inlet streamline and the other, Fig. 4.10d, shows a streamline very near the inlet wall. Both agree qualitatively, except as noted shortly, with the corresponding numerical streamlines shown in Fig. 4.9a.

Although it would be desirable, it is difficult to get quantitative comparisons between prediction and experiment due to both paralax problems and measurement problems. Therefore, this was not attempted to any extent in this study. However, an approximate quantitative comparison can be obtained from Fig. 4.10d because the camera is placed almost directly over the splitter tip. Measurement from the photograph indicates that the streamline enters the receiver at a point located roughly 61% of the receiver width from the splitter tip. Measurement on the contour plot locates the same point at a distance of approximately 66% of the receiver width.

Close examination of the streamline in Fig. 4.10d shows some deviation from the computer plot. In particular, the computer model predicts that the wall streamline, the zero streamline, is slightly to the left of the streamline in the visualization. In fact, in the region near the receivers the visualization streamline agrees much better with the predicted $\psi = -0.125$ streamline. For example, note the curve in the streamline just before entering the receiver.

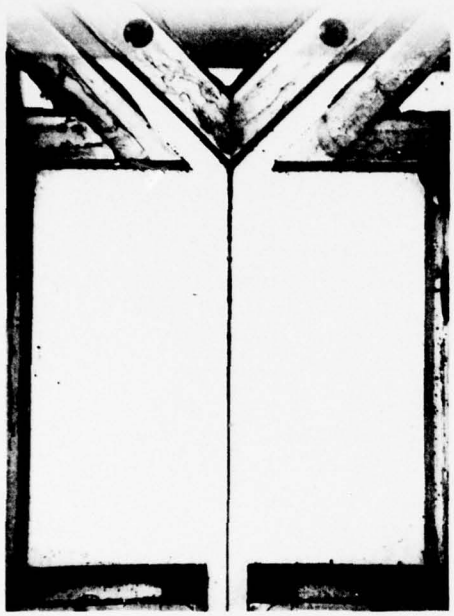

a) Center Streamline, Symmetric Flow

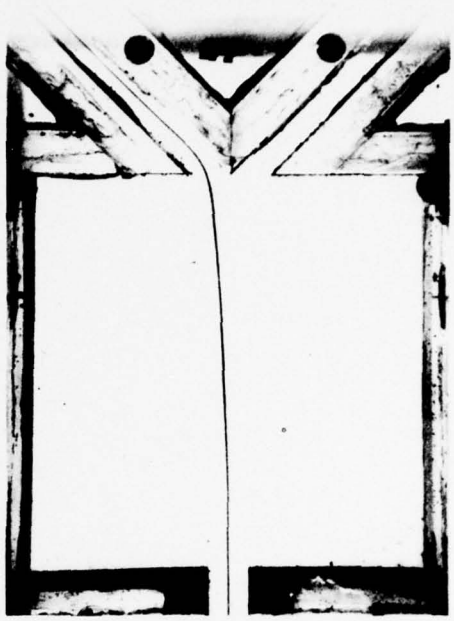

b) Center Streamline, Blocked Flow

c) Wall Streamline, Symmetric Flow

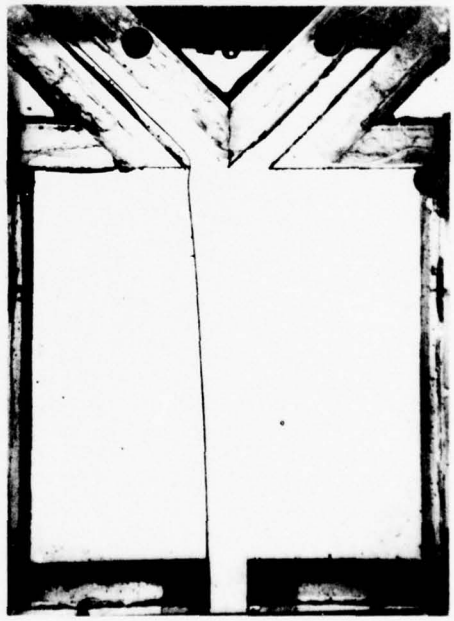

d) Wall Streamline, Blocked Flow

Figure 4.10. Comparison Between Symmetric and Blocked Flows with RE = 100

This deviation can be partially explained because the dye forming the streamline had some width as it left the inlet; that is, it was not all right against the wall. Therefore, it is not exactly the zero streamline and would not be expected to agree exactly with the computer prediction for the zero streamline. However, there does appear to be some other discrepancy and this could possibly be an indication of the numerical problem to be discussed in Section D of this chapter.

The remaining pictures in Fig. 4.10 are the details of the symmetric case with Re = 100 which were mentioned earlier. The two details shown are the center streamline, Fig. 4.10a, and the wall streamline, Fig. 4.10c. Two comparisons can be made. First, these streamlines can be compared with the corresponding experimental streamlines for the blocked case; that is, compare Fig. 4.10a to Fig. 4.10b and Fig. 4.10c to Fig. 4.10d. This clearly indicates the shift of the main flow to the left for the blocked case. Comparing Fig. 4.10c and Fig. 4.10d also indicates that the flow becomes more complex for the blocked case. In the symmetric case the wall streamline enters the receiver smoothly, with only a slight bend, while in the blocked case a pronounced bend occurs just before the streamline enters the receiver.

The second comparison which can be made is to compare Fig. 4.10a and Fig. 4.10c to the corresponding contour plot, Fig. 4.5a. The center streamline and the wall streamline agree fairly well. After entering the receiver the wall streamline does not correspond

exactly with the receiver wall, but this might be expected because, again, the experimental streamline was not exactly the zero streamline due to its finite width at the inlet. The experimental streamline also does not show the same curvature the numerical zero streamline shows as it terminates on the receiver wall. Since the experimental streamline is not exactly the zero streamline this behavior appears to correspond acceptably with that predicted numerically.

B. Flow Field Results for the Deflected Jet

As discussed in Chapter II, the initial deflection of the inlet flow was modeled as an initial angular displacement $\phi$ of the inlet velocity vector. Sample results for deflected flows are shown in Fig. 4.11. The flow modeled in Fig. 4.11a has a Reynolds number of 100, equal receiver flow rates, and a 5° deflection. Some portions of the flow are noticeably unsymmetric, particularly the lower secondary vorticies and the stream function magnitudes reached in the main vorticies. However, the effect on the main flow is small and the flow is almost symmetric in the receiver region.

In Fig. 4.11b the flow conditions are the same as in Fig. 4.11a except the initial deflection is increased to 15°. Compared to Fig. 4.11a the effect of the additional deflection is pronounced. The main flow is noticeably deflected throughout the cavity. Initially there is a strong deflection to the left and then the flow bends back to discharge through the receivers equally. The

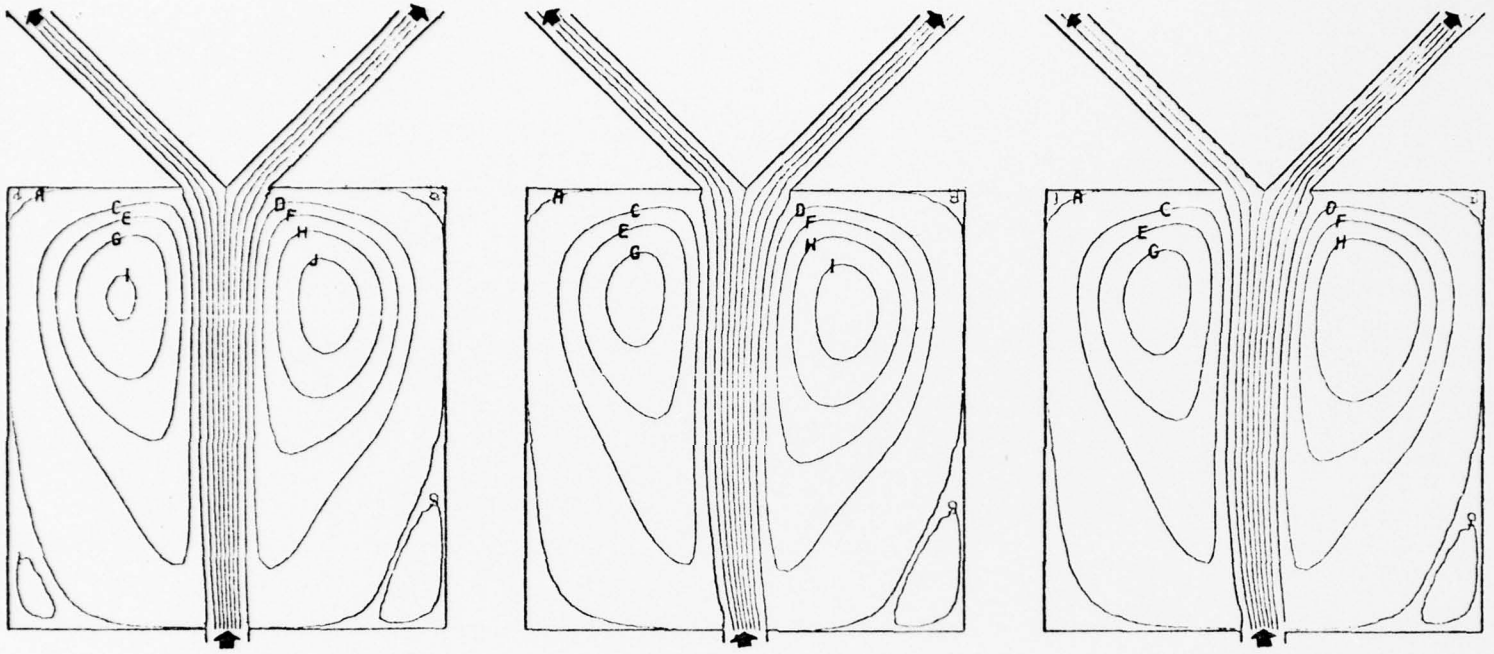


a) $Q_1 = 0.5\ Q_s$ $\phi = 5^\circ$ b) $Q_1 = 0.5\ Q_s$ $\phi = 15^\circ$ c) $Q_1 = 0.375\ Q_s$ $\phi = 15^\circ$

Figure 4.11. Deflected Flows with Re = 100

secondary vorticies in the left cavity region have disappeared and the unsymmetric character of the main recirculation region has increased.

Figure 4.11c is presented as an example of a deflected flow with unequal flow rates in the receivers. Here the deflection is 15°, Re = 100, and $Q_1 = 0.375\ Q_s$. Compared to Fig. 4.11b the effect was to increase the curvature of the streamlines in the main flow, since they must bend back farther to allow 0.625 of the flow to exit through the right receiver.

C. Pressure Field Results

Presentation of the pressure results divides conveniently into three parts. First, a series of pressure solutions corresponding to the flow cases discussed above will be presented. This is followed by discussions of the accuracy of the pressure solutions and the problem of inconsistency.

Pressure solutions are presented as contour plots of lines of constant pressure, or isobars. Referring to Fig. 4.12a, the general format of these plots is as follows:

a. The dark arrows indicate the flow direction.

b. All solid lines, except those denoting the amplifier boundary, are lines of constant static pressure.

c. The pressure magnitudes shown relate to a reference value of one, which is the value assigned to the center node of the inlet. Due to the non-dimensionalization,

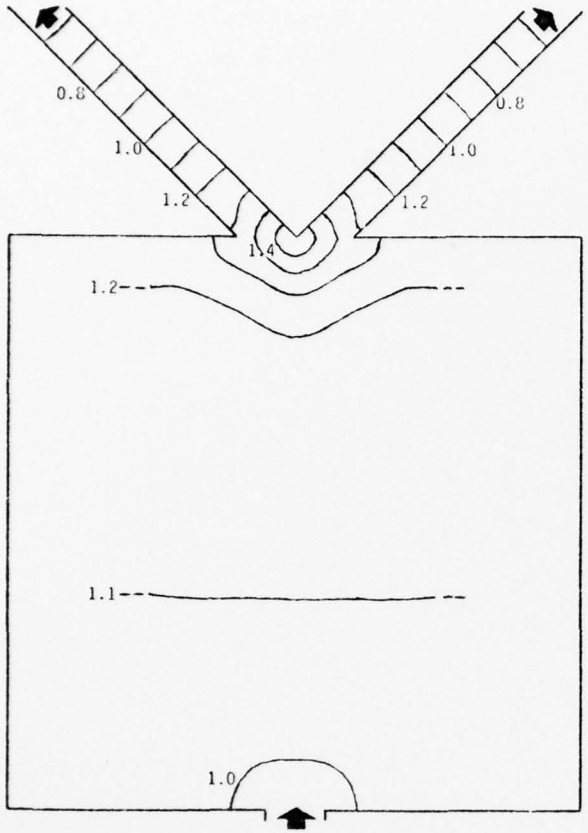


a) Re = 100 $Q_1$= 0.500 $Q_S$ $\phi$ = 0°

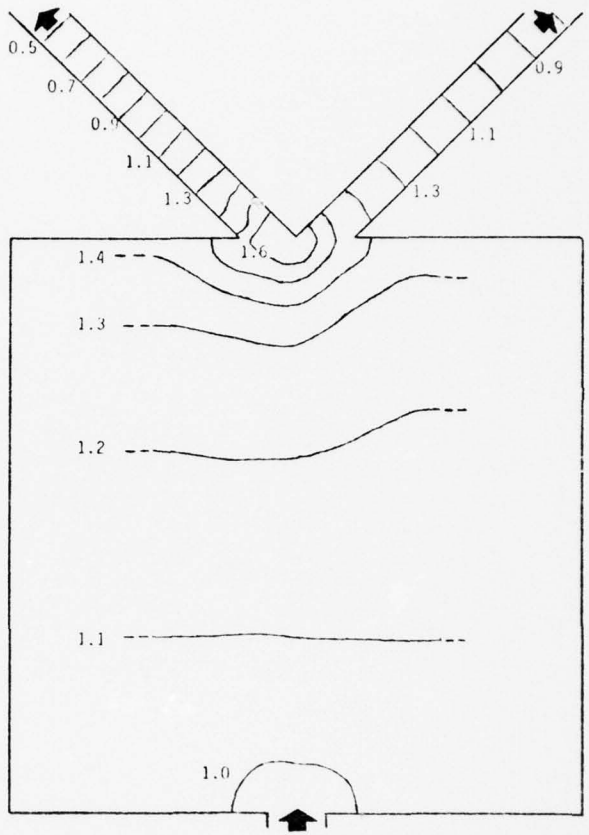


b) Re = 100 $Q_1$= 0.625 $Q_S$ $\phi$ = 0°

Figure 4.12. Pressure Results

a one unit change in magnitude between isobars corresponds to a dimensional pressure change of $\rho U^2$. Water flowing at 73°F at a Reynolds number of 100 has a $\rho U^2$ of $2.2 \times 10^{-4}$ in. of water, or $8.01 \times 10^{-6}$ lb/in$^2$. For SAE 10 oil flowing under the same conditions, this quantity is 1.22 in. of water or $4.39 \times 10^{-2}$ lb$_f$/in$^2$.

d. The dashed lines in the cavity region indicate extensions of the isobars into regions for which pressure values were not calculated.

Figures 4.12a through 4.13b are pressure fields for undeflected flows with Reynolds number of 100. Each figure differs in the ratio, $Q_1/Q_s$, of the left receiver flow, $Q_1$, to the supply flow, $Q_s$. Figure 4.12a represents the pressure field for a symmetric flow field. The pressure drops slightly as it enters the cavity region and then begins a steady increase across the cavity. The pressure magnitude, however, varies very little in the cavity region until the flow nears the splitter. As shown, in the splitter region the pressure gradients are relatively large, with the pressure building to a maximum at the splitter. The pressure then decreases equally in both receivers as the flow passes out of the amplifier.

Similar comments can be made about Figs. 4.12b through 4.13b. In each successive figure of this series more flow is channeled through the left receiver. As shown in Fig. 4.8a through Fig. 4.8d,

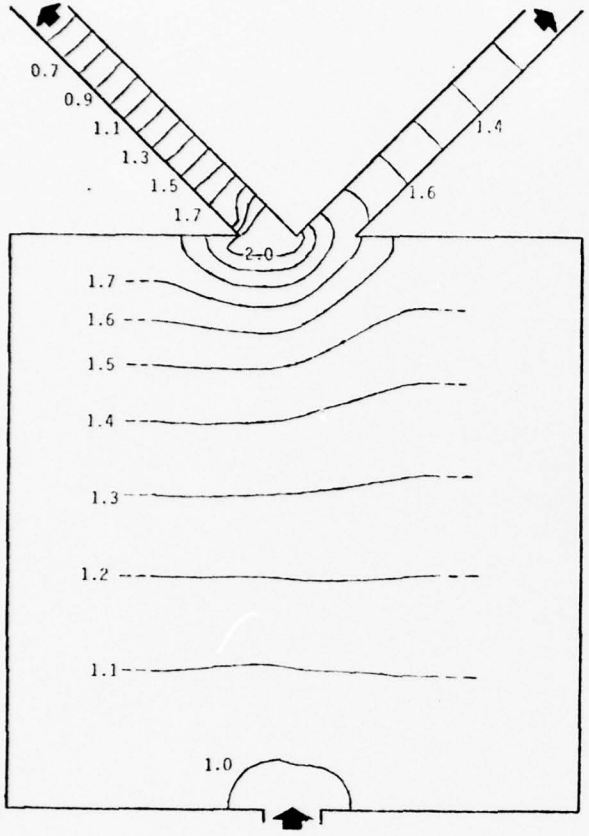


a) Re = 100 $Q_1$= 0.750 $Q_S$ $\phi$ = 0°

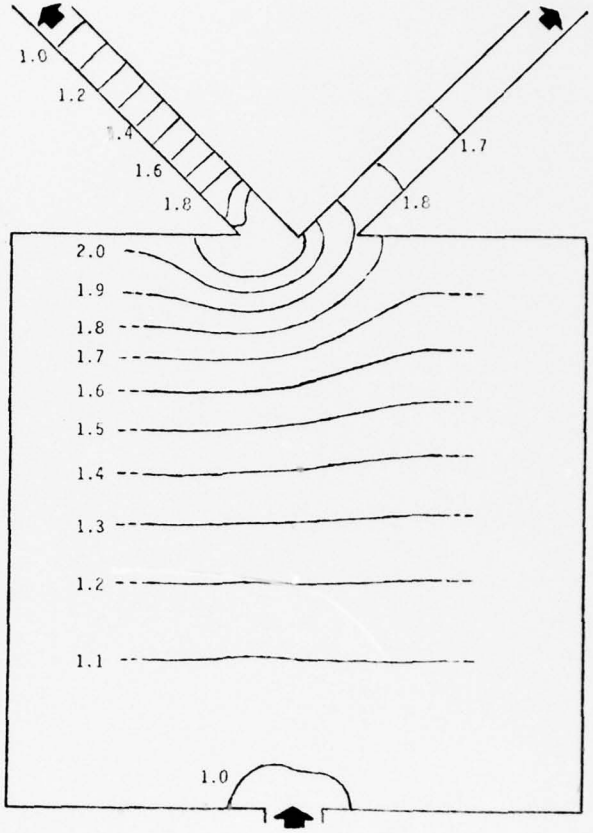


b) Re = 100 $Q_1$= 1.000 $Q_S$ $\phi$ = 0°

Figure 4.13. Pressure Results

this causes the central jet to shift to the left. The effect on the pressure solution is to move the region of highest pressure progressively farther to the left, corresponding to the location of the main jet impingement on the receivers.

Figures 4.14a and 4.14b are pressure fields for deflected flows which have Re = 100, equal outflows, and $\phi$'s of 5° and 15°, respectively. For these cases the inlet jet itself is forced into the left half of the cavity region. This results in a high pressure region, as shown in the figures. Because the outflows are equal, the isobars tend back towards symmetry at the splitter. For $\phi$ = 5° the pressure does become relatively symmetric, indicating that the effect of the initial deflection is small on the receiver region. In fact, the pressures at the receiver outlets are 0.574 and 0.563. For $\phi$ = 15°, however, the deflection has a noticeable effect in the splitter region, with the higher pressure region shifted to the left as would be expected. Here the outlet pressures are 0.594 and 0.539.

## D. Discussion of Accuracy of Pressure Solutions

The general trends of these pressure solutions seem reasonable. There is some question, however, as to the accuracy of the pressure magnitudes predicted, especially for the case having one receiver completely blocked. Several approaches were taken to evaluate the accuracy and trends of the pressure magnitudes obtained.

The first approach was to establish an upper limit on the value of pressure in the amplifier. Consider a flow entering the

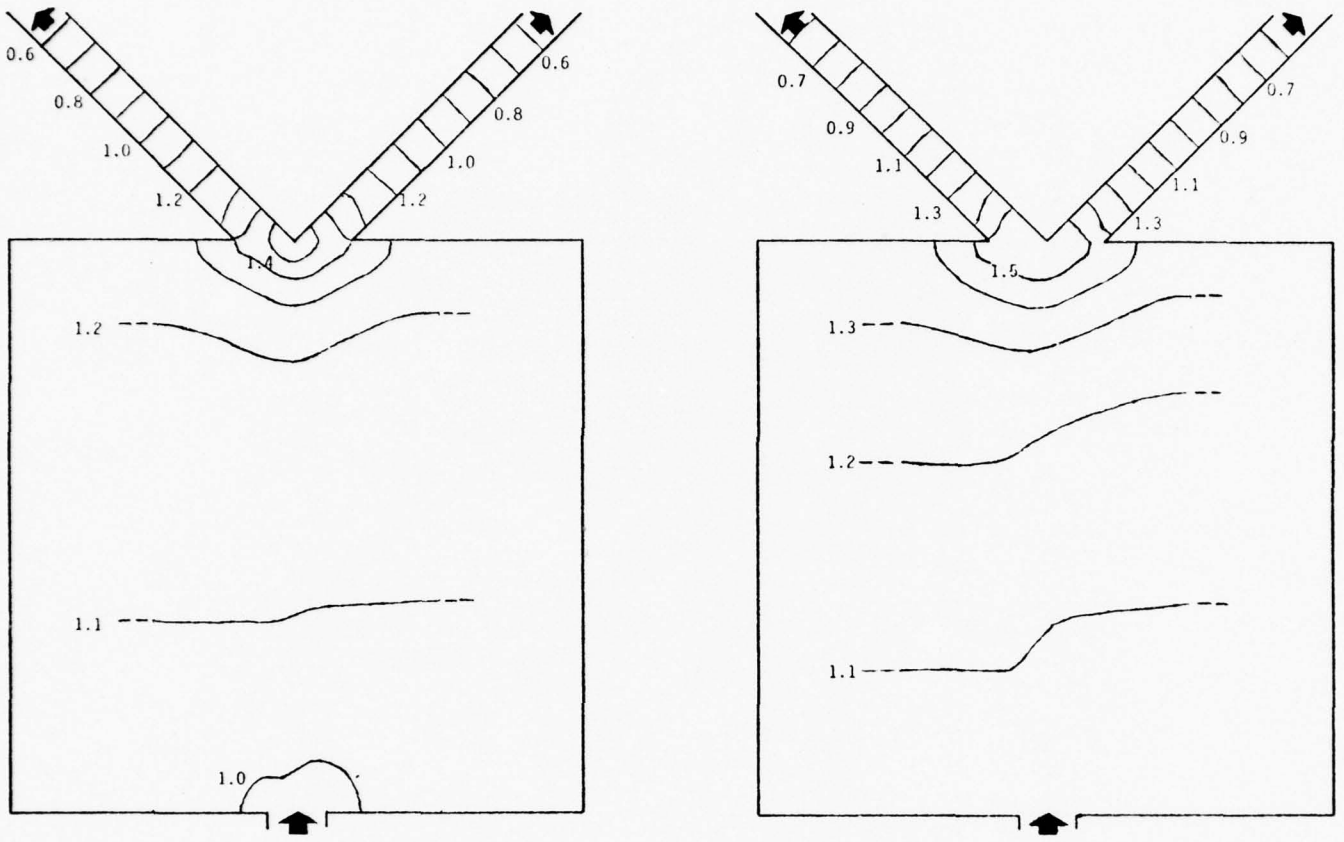


a) Re = 100 $Q_1 = 0.5\ Q_S$ $\phi = 5^o$

b) Re = 100 $Q_1 = 0.5\ Q_S$ $\phi = 15^o$

Figure 4.14. Pressure Results for Deflected Flows

amplifier with a parabolic profile. Assume that there are no viscous effects on the system, that there is no work done on the system, and that no heat is transferred to the system. Assuming that the flow moves directly across the amplifier region, the center streamline in the inlet flow would impinge on the splitter tip. At the inlet the total pressure on this streamline, in non-dimensional variables, is $p + \frac{1}{2} v^2$. Because the velocity is zero on the splitter, under the assumptions made the static pressure at the splitter would become equal to the inlet total pressure. In the absence of work or heat transfer, the introduction of viscous effects can do nothing but lower this value. Therefore, the highest total pressure in the inlet forms an upper limit on the magnitude of the static pressure in the amplifier. For this amplifier this limit would be $p = 2.125$.

The highest pressure in the receiver inlet region for the symmetric case, $p = 1.616$, certainly fits within this limit. In fact, as listed in Table 4.2, the highest pressure for all cases, except the blocked case, meets this criterion. It can be concluded then that the magnitude for the blocked case is incorrect but that for all other cases the values are at least possible.

Further examination of the pressure magnitudes can be made by using the line integral method discussed earlier. This method can be implemented easily for a straight path between the center of the inlet and the tip of the splitter. Eq.(2.9) was numerically integrated using Simpson's rule [1] with the necessary derivatives supplied through centered difference approximations involving the

| $Q_1/Q_s$ | Highest Pressure | Pressure on Splitter | | Inconsistency |
|---|---|---|---|---|
| | | Poisson Solution | Line Integral | |
| 0.000 | 3.647 | 3.340 | 1.235 | 2.039 |
| 0.250 | 2.119 | 2.093 | 1.367 | 0.446 |
| 0.375 | 1.750 | 1.750 | 1.348 | 0.002 |
| 0.500 | 1.616 | 1.616 | 1.388 | -0.171 |
| 0.625 | 1.750 | 1.750 | 1.348 | 0.002 |
| 0.750 | 2.119 | 2.093 | 1.367 | 0.446 |
| 1.000 | 3.647 | 3.340 | 1.235 | 2.039 |

Table 4.2. Pressure Solution Details.
All quantities non-dimensional.
Re = 100.

flow field solutions. For the symmetric case the value obtained for the pressure at the splitter tip is 1.388. This is 15% lower than the value predicted by the solution of Eq.(2.8), which will be referred to as the Poisson solution. As discussed earlier, error is possible in use of the line integral method. Which answer is the better is still in question. The point is that these values are certainly comparable and that either value is reasonable. It should be emphasized again that both methods utilize identical flow field solutions and any differences here are due entirely to the different methods for extracting pressures.

As the flow rate in the receivers is varied from the symmetric case, the line integral method predicts very little change in

pressure, as tabulated in Table 4.2. In comparison the values predicted by the Poisson solution become sharply larger.

Some indication of which trend is correct can be obtained by a control volume analysis of the central jet, similar to that which forms the basis for the cowl streamline method [11]. The results will only illustrate trends because of the necessary simplifying assumptions. These are

a. The viscous loss across the cavity is negligible.

b. The pressure across both the inlet and the splitter regions is constant.

It is also noted that there is no work done or heat transferred to the flow. The control volume is taken as the region between the streamlines $\psi = 0$ and $\psi = -1.0$. For the symmetric, Re = 100 case this would result in the control volume shown in Fig. 4.15. For the assumed flow the applicable non-dimensional energy equation [27] is

$$\int_{\text{inlet}} (\tfrac{1}{2} V^2 + p)\, v\,dx = \int_{\text{receiver}} (\tfrac{1}{2} V^2 + p)\, v\,dx \qquad (4.1)$$

where $V = \sqrt{v^2 + u^2}$. Using the velocities given by the numerical flow solutions and assuming the pressure at the inlet equal to one, Eq.(4.1) can be solved for the average pressure over the receiver end of the control volume. The integrals were evaluated using Simpson's rule.

For the symmetric case the end of the control volume extends across both receivers. The average pressure predicted is 0.785. For

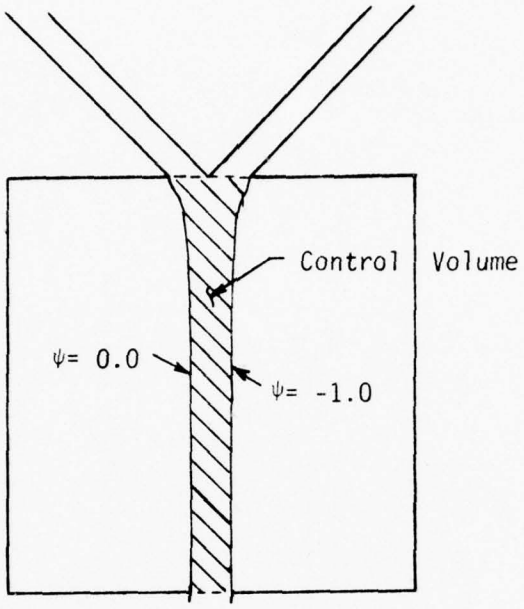


Figure 4.15. Typical Control Volume for Integral Pressure Calculations

the blocked case the control volume covers only the left receiver. For this region the predicted average pressure is 1.305. Because these pressures are averages, no comparisons will be made using the actual magnitudes predicted. The important comparison is that there is a substantial increase in the average pressure in the receiver inlet region as the outflow increases through the left receiver. This general trend is the same as that found in the Poisson solutions for pressure and is contrary to that predicted by the line integral method. In this respect then the Poisson solutions are preferred.

A further check on the accuracy of the pressure solutions can be obtained by examination of the predicted pressure drop in the receivers. At the outlet of the two receivers the flow has been

forced to be fully developed by the imposed boundary conditions. Moreover, with this restriction at the boundary the resulting flow solutions predict that the flow is fully developed over the entire last half of each receiver. Hence, this flow is fully developed flow between parallel plates, for which there is an analytic solution for the pressure drop. In terms of non-dimensional variables the pressure gradient is [27]

$$\frac{dP}{da} = - \frac{12\ (\Delta\psi)}{w^3\ Re} \tag{4.2}$$

where $\Delta\psi$ is the difference between $\psi$ on the two walls. Evaluation of Eq.(4.2) gives an analytic prediction of the pressure gradient for a given flow situation. A numerical prediction can be obtained by centered differencing of the predicted pressure values in this region. For the symmetric, Re = 100 case, Eq.(4.2) predicts a pressure gradient of -0.1697 for the left receiver. Differentiation of the numerical results gives -0.1654. Similarly for the cases of $Q_1 = 0.75\ Q_s$ and $Q_1 = 1.0\ Q_s$, the comparisons are, respectively, -0.254 versus -0.264 and -0.340 versus -0.386.

The most obvious disagreement occurs in a blocked receiver. Here there should be no pressure gradient at all, but a gradient of -0.046 is predicted numerically. This is caused by the method for compensation for inconsistency. The compensation introduces a non-zero $s_{ij}$ into the equations for this region. Nevertheless, the general agreement is good and this comparison indicates that the

Poisson solution does indeed yield the correct pressure gradients in the receivers for the given flow fields.

Because experimental pressure values were not obtained, the above comparisons form the basis for an evaluation of the pressure results. As stated, the location of the high pressure regions seems to be correct for the different cases. Also, for the symmetric case the pressure magnitudes are reasonable. As the flow conditions vary away from symmetric flow, the pressure values in the region of highest pressure change in the correct manner, i.e. they increase over the more symmetric case. However, they increase too much and for the blocked case reach magnitudes which are not physically possible. In summary, it appears that results of the numerical model are reasonable for cases in the approximate range of $0.250\ Q_s < Q_1 < 0.750\ Q_s$. Outside of this range the results are questionable.

A possible explanation for this behavior involves the wall gradients and internal derivatives of $\psi$ which are being numerically evaluated. For the symmetric case half of the flow leaves through each receiver. As the specified flow situation deviates from the symmetric case, more flow must exit through one receiver until, for the blocked case, all the flow exits through one receiver. As a result of increased flow through the same area, the gradients in stream function in the region near the splitter must necessarily become larger. Further, these gradients must be evaluated for use in the Poisson solution using finite difference approximations having the same grid spacing. Apparently, as the flow rate increases

the five grid points across each receiver are not sufficient to allow accurate determination of these gradients. When these inaccurate gradients are used in the Poisson equation, the previously discussed inaccuracies in the pressure values result.

Besides the question of inaccuracies discussed above, there remains the problem of inconsistency. A physical interpretation of inconsistency can be obtained by examining a two dimensional heat conduction problem. The appropriate equation is

$$\frac{\partial^2 T}{\partial x^2} + \frac{\partial^2 T}{\partial y^2} = - \frac{u'''}{k} \tag{4.3}$$

where T is the temperature, u''' is the internal heat generation, and k is the thermal conductivity [2]. Consider a square region with insulation on all four sides. The heat transfer across the boundaries is zero and the resulting boundary conditions are

$$\frac{\partial T}{\partial n} = 0 \quad . \tag{4.4}$$

For this Neumann problem consistency requires that the integral of the forcing function, u'''/k, over the region must equal the line integral of the normal temperature gradient on the boundary, that is,

$$\iint \frac{u'''}{k} \, dxdy = \oint \frac{\partial T}{\partial n} \, ds \quad . \tag{4.5}$$

Physically this means that whatever heat is generated in the region must either be absorbed in the region or must leave the region.

Because no heat can leave the region for the problem considered, the integral of the internal heat generation must be zero.

Other heat conduction problems can be imagined to further illustrate the concept of inconsistency. These problems are easily visualized in physical terms and, consequently, they form a convenient method for viewing inconsistency.

The physical interpretation is not nearly as simple for the pressure problem. It is not clear what is physically represented by the forcing function of Eq.(2.8), which is $2\left(\frac{\partial^2\psi}{\partial x^2}\frac{\partial^2\psi}{\partial y^2} - \frac{\partial^2\psi^2}{\partial x \partial y}\right)$. However, this function is mathematically analogous to the heat generation term in the conduction problem. Therefore, the boundary gradients on pressure must allow for this "generation." If they do not, the problem is inconsistent and is a contradiction of physical principles.

In contrast, for the corresponding difference equations a converged solution can be obtained through iteration using SOR. This assumes the convergence criterion used in this study. As pointed out in Section II-C, the numerical algorithm appears to allow for the inconsistency as it converges. The mathematical reason and explanation for this was not found but a series of numerical experiments were performed in an effort to characterize the phenomenon.

Besides the previously discussed residuals, the most interesting effect observed dealt with the convergence of an inconsistent formulation. Using a conventional convergence criterion, say

$\left|P_{ij}^{k+1} - P_{ij}^{k}\right| < \varepsilon$, with no manipulation of the pressure arrays, as in Section II-C, the solution may or may not converge. The differences between successive iterations diminish until the pressure at each point varies a fixed amount, that is, $\left|P_{ij}^{k+1} - P_{ij}^{k}\right|$ = constant. The magnitude of this change depends on the value of the inconsistency, the relaxation factor, and the grid spacing. If the inconsistency is large enough, the change will never become less than $\varepsilon$. Even if the convergence criterion is met, the solution values would still drift if the calculations were continued. Thus, consideration of inconsistency helps explain the drifting behavior noted by Roache [20] for convergence of pressure solutions. Further, it was observed that if the pressure formulation were made consistent, the solution would indeed converge and the change $\left|P_{ij}^{k+1} - P_{ij}^{k}\right|$ would go to zero.

The convergence criterion used in this study is not affected by the above problem because it forces convergence to a surface shape and is, therefore, not affected by uniform translation of the entire surface. It is felt that such a criterion is the appropriate convergence criterion for the Neumann problem.

The effect of inconsistency on different iterative solution techniques was not determined. All observations were made using point SOR as the method of solution. One other method, Jacobi's method [20,30], was attempted on a simple Neumann problem. The resulting solution exhibited an apparent standing wave propagating back and forth across the region. Based on this experience,

Jacobi's method seems inappropriate for use on the Neumann problem.

Convergence of $\nabla^2 P$ for an inconsistent formulation to the values $s_{ij} + s'$ naturally results in an incorrect relationship between values of pressure at adjoining nodes. In particular, the gradients specified as boundary conditions are not reflected in the converged solutions. This observation is also made by Young and Gregory [30].

The actual magnitude of inconsistency varies between the different solutions. For Re = 100 the symmetric case had a total inconsistency of -0.171. The effect of this inconsistency is shown rather dramatically by comparing Fig. 4.16a and Fig. 4.16b. Here isobars of equal magnitude are plotted for compensated, Fig. 4.16a, and non-compensated, Fig. 4.16b, pressure solutions based on the same flow field. It should be noted that this comparison is somewhat misleading, since the large change in the isobars was caused by a small change in the pressure values. An indication of the magnitude of change between the respective solutions is given by comparison of the value predicted for pressure at the splitter tip. These values are 1.616 for the compensated case and 1.575 for the non-compensated case.

Referring to Table 4.2, the magnitude of inconsistency becomes smaller for the case where $Q_1 = 0.625\ Q_s$ and then increases as the blocked case is approached. This follows a similar trend as

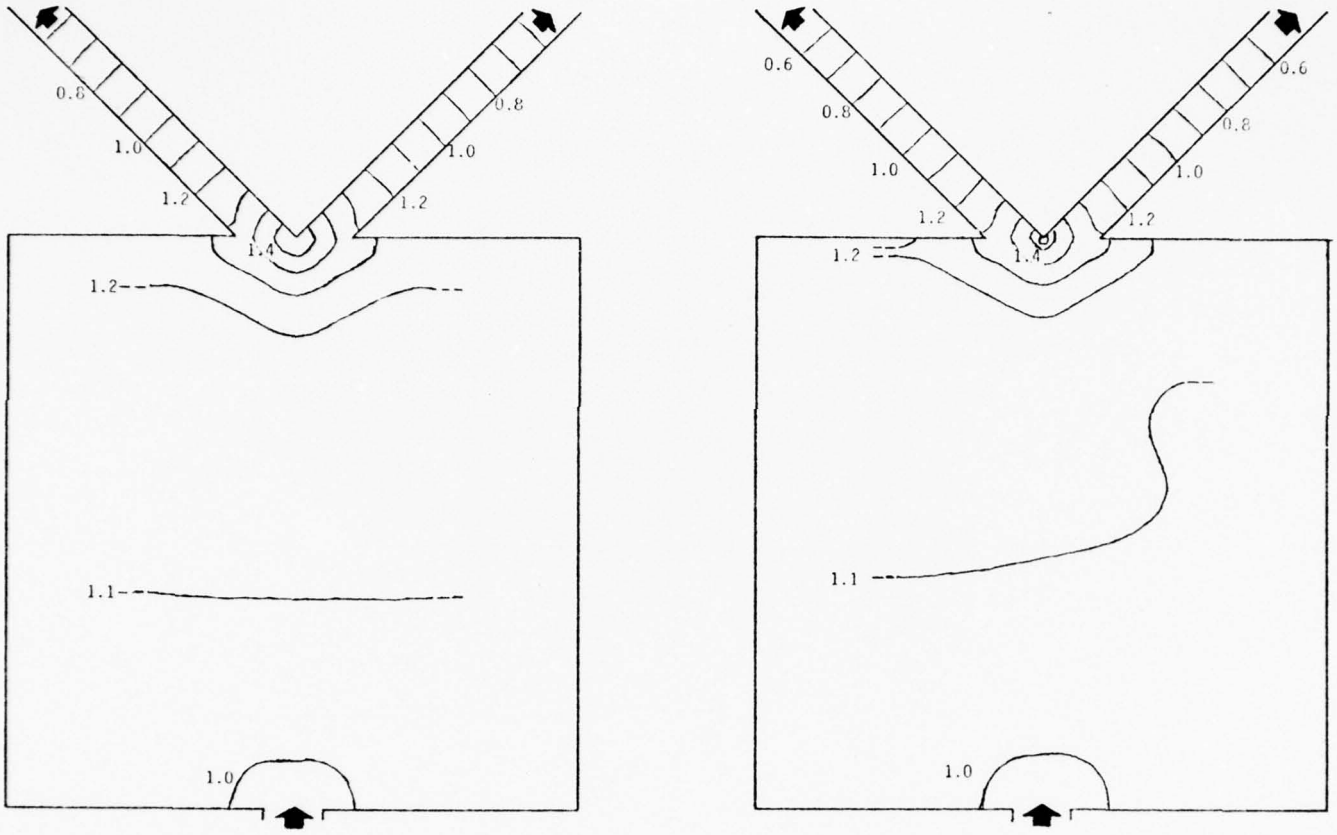


Figure 4.16. Comparison of Compensated and Non-compensated Pressure Solutions

the inaccuracy in pressure magnitudes discussed earlier and the two problems are probably related through the inaccurate resolution of gradients near the splitter.

It is felt that there are two probable causes of numerical inconsistency. Both are related to truncation error. The first, and most obvious, is the inaccuracies inherent in forming the difference approximations for the boundary gradients and the forcing functions. This is the same problem as discussed earlier as an explanation for the inaccuracy of the pressure magnitudes. Given an accurate flow solution and a means for accurate evaluation of the derivatives of $\psi$ in Eqs.(2.8) and (2.9), there would be no inconsistency problem. The flow equations are derived taking the pressure gradients into account. Therefore, if flow solutions were exact, the gradients and forcing functions would necessarily be compatible. However, this is not the case. There is some error in the flow solutions and, more significantly, there is the possibility of relatively large errors in the necessary numerical derivatives of $\psi$. Again, this is compounded when the gradients become steeper and more difficult to approximate as $Q_1$ increases. Such errors in the approximations result in a failure to satisfy the discrete consistency equation.

Although there is some error in derivative approximation throughout the region it is felt that the bulk of the inconsistency results from errors in particular regions. If the difference approximations could be improved in these areas, the inconsistency problem should be greatly alleviated.

A second possible cause of numerical inconsistency lies in the conservation properties of the basic finite difference scheme for the flow field. Second upwind differencing is designed to conserve vorticity [23]. By this it is meant that in any region the time rate of accumulation of $\zeta$ equals the net advection and diffusion of $\zeta$ across the boundaries of the region [20]. This is a property of the difference scheme and can be guaranteed by proper formulation of the difference approximations to Eq.(2.6). Other schemes are designed to conserve the vorticity squared, linear momentum, and/or kinetic energy [20]. It is speculated that there is a quantity related to pressure, which may or may not be one of the above, which also must be conserved by the differencing scheme. Possibly this quantity could be isolated and differencing schemes found in the literature, or developed, which would give the desired conservation properties.

## E. Characteristic Design Curves

Recall that for design purposes a steady flow fluidic amplifier is described by one or more characteristic curves. These can be computed from the mathematical model by selecting an inlet flow rate, or Reynolds number, and a deflection $\phi$. The flow rates in the receivers can then be varied from blocked to full flow and a flow field and resulting pressure solution obtained for each case. The pertinent pressure values at the amplifier ports can be plotted on any of the various characteristic curves described in Chapter I.

For example, the flow in one receiver can be plotted against the pressures at the outlet of the receivers, as in Fig. 4.17.

One series of solutions for positive $\phi$ will also give the results needed for negative $\phi$ due to symmetry conditions. That is, $P_1$ for the case $\phi = 15°$, and $Q_1 = 0.625\ Q_s$ is the same as $P_2$ for $\phi = -15°$, $Q_2 = 0.625\ Q_s$. Similarly, $P_1$ for the case $\phi = 0°$ and $Q_1 = 0.625\ Q_s$ is the same as $P_2$ for the case $\phi = 0°$ and $Q_2 = 0.375\ Q_s$. Thus, only eight solutions were required to generate the 15 points used in Fig. 4.17.

The accuracy of the curves plotted in Fig. 4.17 for the device in this study are questionable due to the problems in obtaining accurate pressure solutions. These were discussed in the previous section. Because of the accuracy problem only the cases with receiver flow rates between $0.250\ Q_s$ and $0.750\ Q_s$ were plotted. Even with this restriction, the trends do not seem quite right compared with physical reasoning.

For example, the double valued character around $P = 0.5$ is unlikely. Consider the curves for $P_1$. This outlet pressure is determined by the pressure in the receiver inlet, the pressure drop due to entrance effects as the flow enters the receiver, and the viscous pressure drop in the receiver. The pressure in the splitter region is expected to rise as the flow $Q_1$ increases (Section D, Chapter IV). Exactly what the entrance effects would do as the flow rate increases is uncertain. The steady state viscous pressure drop in the receivers increases linearly, as in Eq.(4.2). Using the pressure

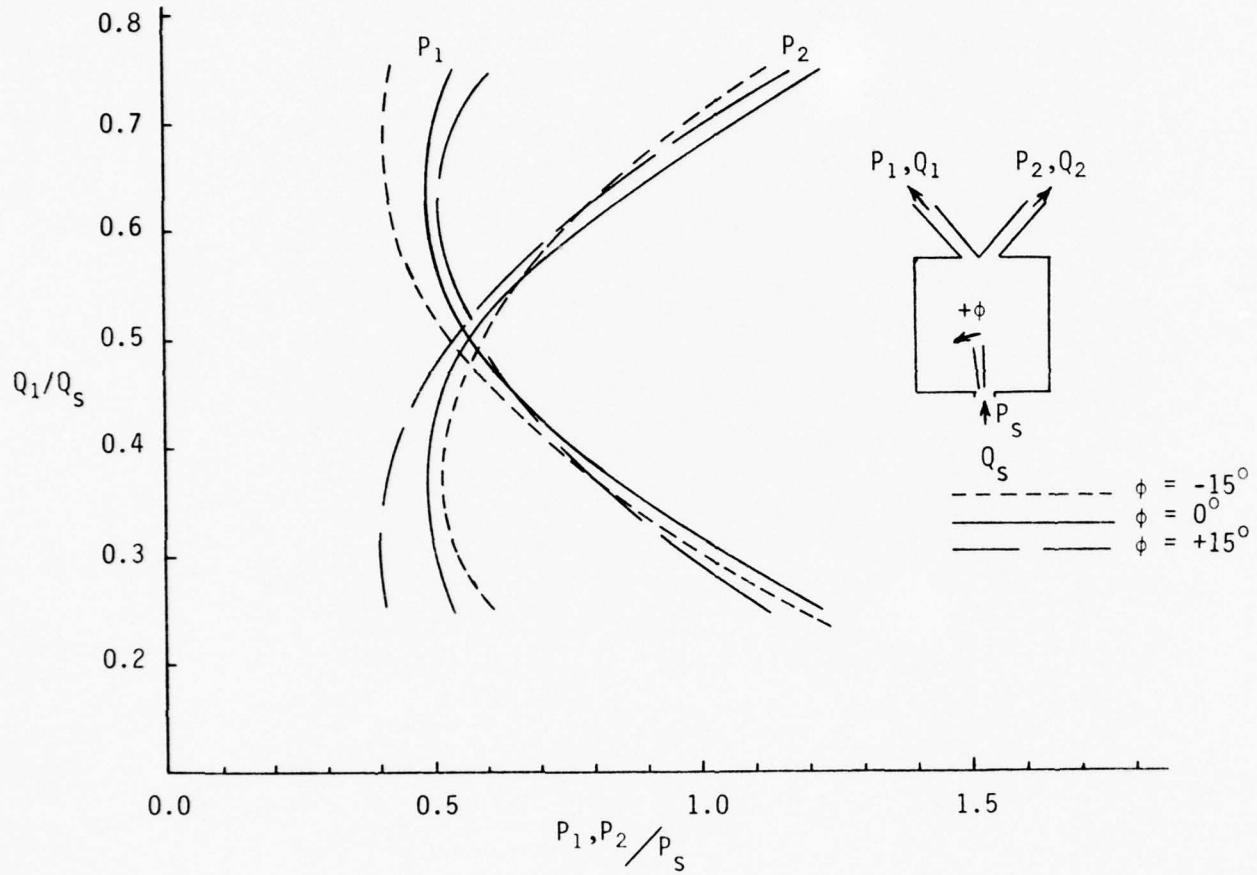


Figure 4.17. Outlet Characteristic Curve
Re = 100

gradients presented in Section D and a length of 5 units, the linear pressure drop in the receiver would increase from roughly -0.827 for the symmetric case to -1.93 for the blocked case. For this same range of flow rates the receiver inlet pressure begins around 1.6 and is bounded by an upper value of 2.125. Since entrance effects must increase the pressure drop down the receiver, it is felt that the terms producing a pressure drop in the receiver should dominate the pressure increase at the inlet and the curve for $P_1$ should continue to lower values of pressure as $Q_1$ increases.

It is also noted that the cross-over of the curves for the deflected cases at approximately P = 0.75 is questionable. Nevertheless, with refinement of the pressure solutions there is no reason why useful characteristic curves for design work could not be obtained for the geometry considered.

## F. Edgetone Oscillations

For a laminar free jet impinging on a solid object it has been noted in the literature [4,5,22] and was observed in the experiments of this study that a transverse oscillation of the jet occurs for certain flow situations. These "edgetone" or "jet-edge" oscillations are stable, periodic and two-dimensional.

An example of this oscillation observed in the present study is shown in Fig. 4.18. For this flow the left receiver is blocked and the Reynolds number is 360. Each picture in Fig. 4.18 represents

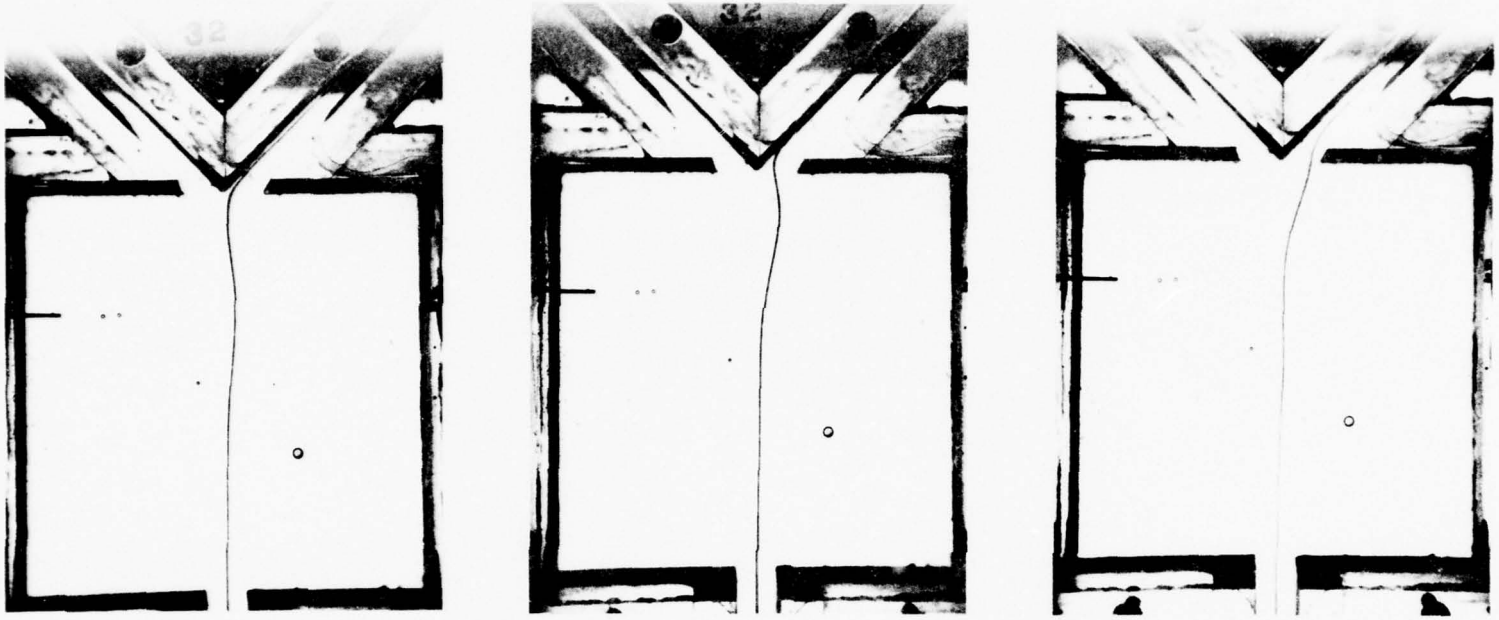

(a) (b) (c)

Figure 4.18. Edgetone Oscillation
Re = 360 $Q_1$ = 0.0

the same streamline at a different point in time. The oscillation was stable, had a constant frequency, f, of 0.22 cycles/sec, and was of relatively large amplitude.

The first signs of oscillation were experimentally observed before the Reynolds number reached 360. At Re = 290 the first signs of an oscillation were observed and when Re = 300 the oscillation was well defined. This oscillation had a slightly lower frequency, 0.19 cycle per second, and a much lower amplitude than the oscillation shown in Fig. 4.18.

As discussed by Rockwell [22], edgetone oscillations depend on the Reynolds number, the distance h the incoming jet must travel before impinging on a surface, the width b of the inlet nozzle, and the height of the cavity. The effect of cavity height is to introduce three dimensional effects which tend to retard, with respect to increasing Reynolds number, the onset of oscillation [22,25]. In his experimental work, which was highly three dimensional since the nozzle aspect ratio equaled one, Rockwell observed that no oscillations occurred in flows which had Reynolds numbers less than 1250 and a h/b ratio of 10. With the nozzle aspect ratio of 4 used in the experiments of this study the three dimensional effects are reduced and the Reynolds number at the onset of oscillation should be reduced, as was the case.

In the present study the value for the Strouhal number, fb/U, was identical for the two experimental oscillations for which f was

measured. This value was 0.0095. That it is a constant agrees with the trends presented by Rockwell [22]. The magnitude, however, is lower than that predicted by Rockwell. An extrapolation of Rockwell's results to the flow conditions of this study predict a Strouhal number value of 0.03.

Unfortunately, the edgetone oscillations were not predicted by the numerical simulation. Therefore, although the simulation is stable and will converge for higher Reynolds numbers, the results are meaningful only up to a Reynolds number of roughly 290. A probable cause of the failure of the numerical model to predict the edgetone oscillations is the handling of the outflow and inflow boundary conditions. In both cases the flow is forced to be fully developed. In effect, an oscillation cannot exist at the receiver outlet nor at the amplifier inlet. These constraints tend to suppress the development of oscillations in the flow field.

A second possible cause of this weakness in the numerical model is the artificial viscosity introduced by second upwind differencing [20,21]. Artificial viscosity refers to a completely numerical, artificial diffusion effect which is introduced by the method of differencing. This term damps out small perturbations and instabilities in the flow and could be eliminating the physical mechanism which triggers the edgetone oscillations.

## G. Discussion of the Numerical Method

During the development of the numerical model for the flow field several observations on the computational procedure itself were made beyond those mentioned earlier in this chapter. These observations will be presented in this section.

Discussion in Section D of this chapter emphasized the possible resolution problems in the splitter region. The possibility of resolution problems was considered even before these problems were discovered in the pressure solution work. Early in the study comparisons were made between solutions to the same case but with two separate grids. One grid consisted of 21 nodes in the x-direction and 29 nodes in the y-direction, giving $\Delta x = \Delta y = 0.5$. The other grid was the 41 x 57 grid used for all results presented in this report. It has $\Delta x = \Delta y = 0.25$.

For the lower Reynolds numbers the results on the different grids were very similar. For example, compare Fig. 4.19a and Fig. 4.19b, which are such a set of solutions for symmetric flow with $Re = 10$. However, for larger values of Reynolds number the results were different on the two grids. Figure 4.19c and Fig. 4.19d are examples of such a difference for symmetric, $Re = 100$ flow.

This result is reasonable when the accuracy of the difference scheme is considered. Recall that the differencing of the vorticity equation is second-order accurate on the differencing of the diffusion terms but only first-order accurate on the differencing of the

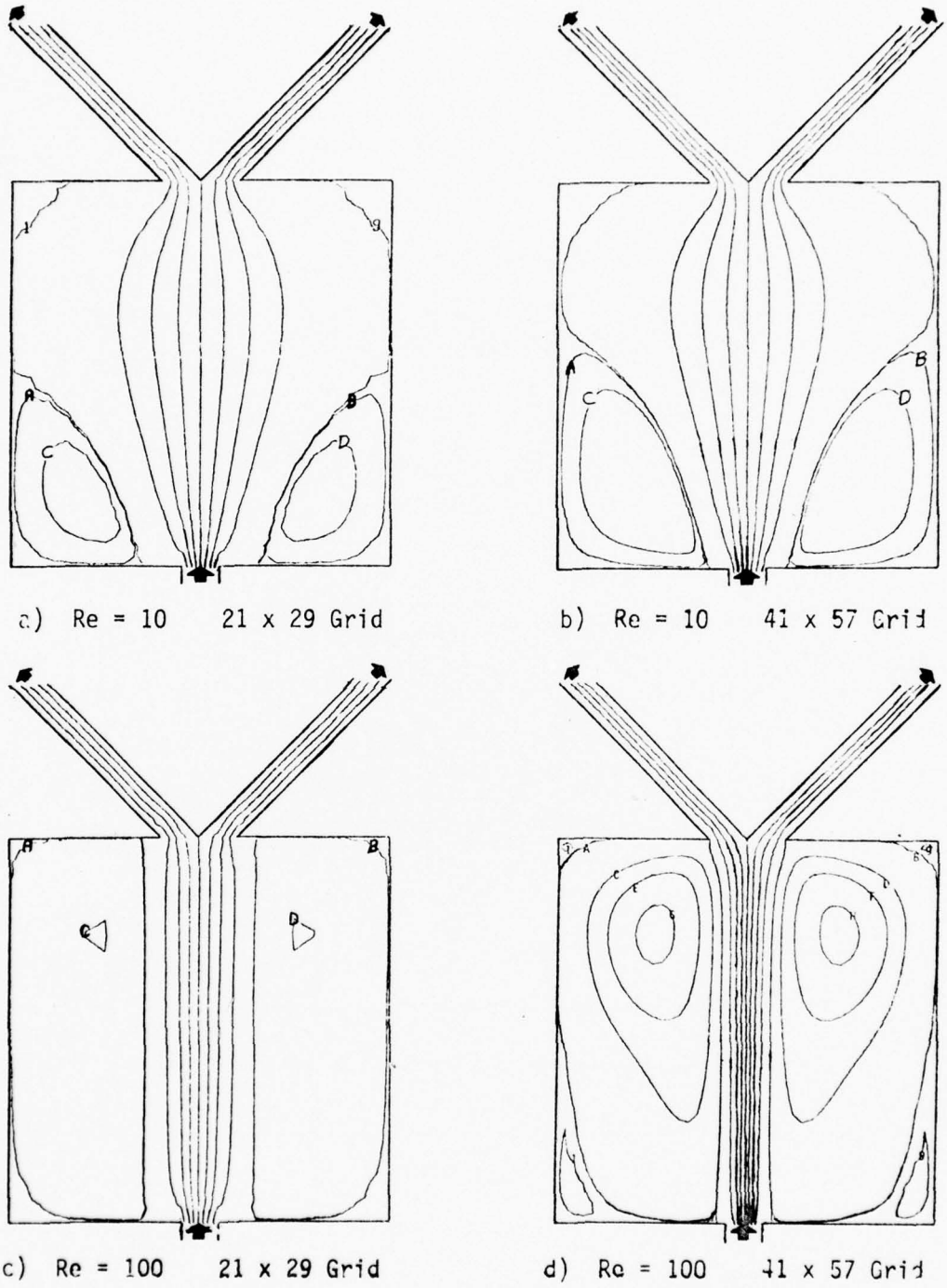


a) Re = 10 21 x 29 Grid

b) Re = 10 41 x 57 Grid

c) Re = 100 21 x 29 Grid

d) Re = 100 41 x 57 Grid

Figure 4.19. Effect of Grid Spacing on Flow Solutions

advection terms. For low Reynolds numbers the flow is diffusion dominated and the second-order accurate differencing gives similar solutions for both grids. At higher Reynolds numbers the advection terms dominate the flow field and the first-order accurate differencing is insufficient to model the process on the coarse grid. This results in the large difference between the two solutions for Re = 100.

As discussed earlier the experimental flow fields and those predicted using a 41 x 57 grid compare very well. Conversely, the pressure results indicate that regardless of the agreement between experimental and numerical flow results the grid needs refining in the splitter region to obtain good pressure solutions. Thus, further resolution studies should be aimed at examining such techniques as variable grid spacing so that extra nodes are placed near the splitter.

As is probably true in most computational fluid dynamics problems, the final numerical boundary conditions were not the same as those initially attempted. Two changes worth noting are illustrated in Fig. 4.20. All three contour plots represent converged flow fields for symmetric flow with Re = 100. Figure 4.20a is the first converged, stable solution for Re = 100 obtained in this study. In this formulation the wall vorticity in the cavity region was given by

$$\zeta_w = \frac{2\,(\psi_{w+1} - \psi_w)}{\Delta n^2} + O(\Delta n) \qquad (4.6)$$

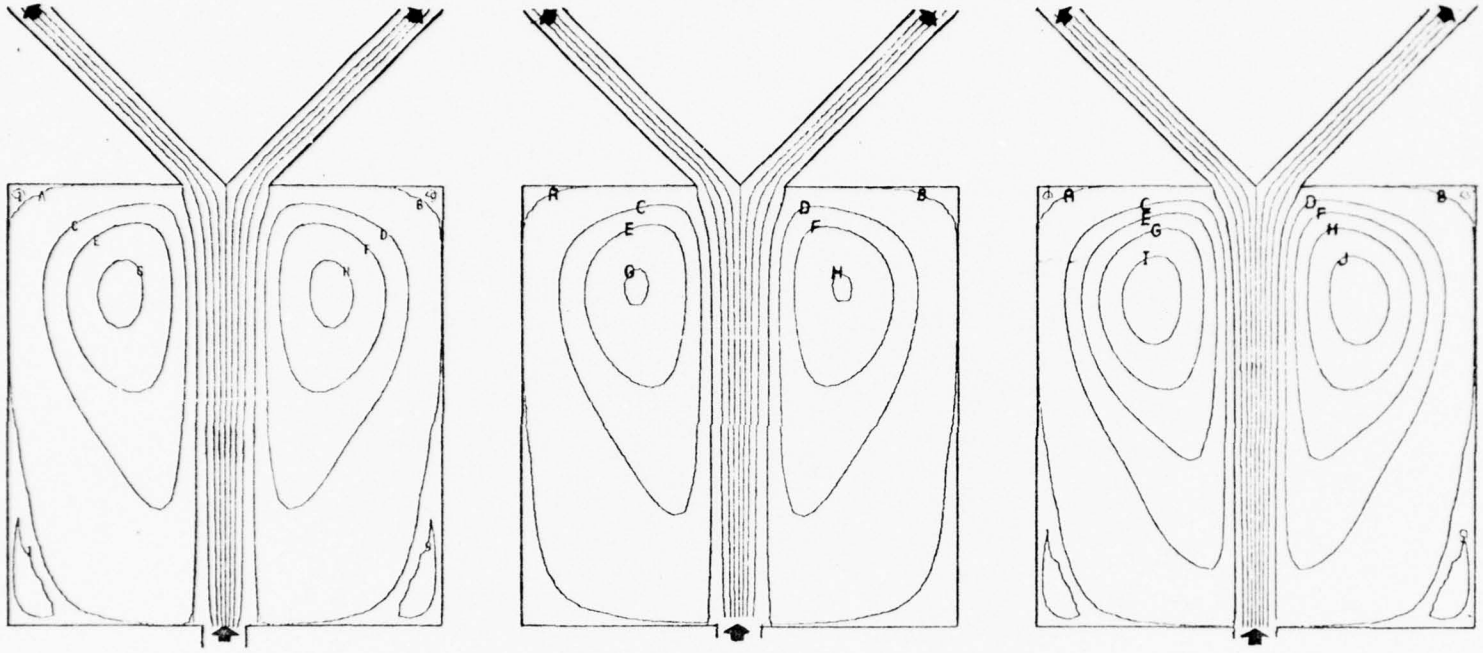

a) First Order Accurate Wall Vorticity Condition

b) Second Order Accurate Wall Vorticity Condition

c) Fixed Inlet Vorticity Values

Figure 4.20. Effect of Various Boundary Conditions on Flow Solutions

where n is the normal to the wall [20]. Note that this expression is first order accurate. This equation was also used to evaluate the vorticity at the corners of the inlet instead of setting these two values in keeping with the parabolic inlet velocity profile (Chapter II, Section C). Because the vorticity is singular at these two points, it was not initially apparent which of these alternatives to take.

The first refinement on the wall vorticity resulted in Fig. 4.20b. The formulation differs in that the second order accurate expression for wall vorticity, Eq.(2.18e), was implemented. Noticeable change occurred in the recirculation regions, with the maximum value of $\psi$ in the main recirculation region becoming smaller and the secondary recirculation region disappearing altogether. However, the general shape of the flow remained the same and, in fact, the main flow was not changed at all.

The final change, resulting in the flow field of Fig. 4.20c, was to try the other alternative for the inlet corner vorticity values. Instead of using Eq.(2.18e) these values were based on the parabolic inlet velocity profile, as in Eq.(2.20). The effect on the main jet is clearly visible. The 0.0 and -1.0 streamlines detach from the wall immediately and extend downstream. The distance between the two streamlines remains considerably less than in (b). That this formulation was the better choice for a boundary condition is confirmed by the comparisons with experimental results.

An important consideration in the use of a numerical routine as a design tool is the computational time required to obtain a converged solution as this translates directly into costs. For several reasons it is difficult to give a meaningful figure for convergence time. In particular, the same numerical routines would require varying times for convergence on different computer systems. The figures given here will all relate to the CDC 6600 system in use at The University of Texas. Even on that particular system several numbers could be used as the figure for convergence time. The time presented here is the "TM" time, which includes central processing time, peripheral processing time, and a time charge based on tape and disk usage.

As an example consider the symmetric case for flow with Re = 100. The flow field for this case converged in 756 seconds. The pressure solution then required 28 seconds.

The time required for the pressure solution varied very little for the different cases. The time for obtaining the flow field solution varied considerably for the different cases, with the variations following some general trends. As the Reynolds number increased the time required for convergence increased. For symmetric flow with Reynolds numbers of 20, 100, and 275, these times were respectively 693, 756, and 1021 seconds. Although the exact time for Re = 1000 is not available, that solution required roughly 2500 seconds.

Also, for a given Reynolds number unsymmetric flows in general required more time for convergence. Consider the effect

of unsymmetric outflow. For Re = 100 and no deflection, the symmetric case required 756 seconds while the blocked case required 1528 seconds. Likewise, with balanced outflows but with a 15° deflection of the inlet jet, the convergence time was 1058 seconds. These trends seem reasonable because the flow becomes physically more complex as the case considered becomes more unsymmetric. However, it should be noted that there were deviations from these trends.

Consider the computer time required to produce the characteristic curves shown on Fig. 4.17. The fifteen points presented on this figure required solutions to eight separate flow cases. The flow field and pressure solutions for these eight cases took a total of 6768 seconds to compute, which is an average of 846 seconds per case.

At this stage in the development of the computer model as a design tool this figure indicates that such a use might be competitive with other approaches. However, no actual analysis was made to determine what an "economic" cost for a simulation might be. It is simply noted that the actual computer time is not unduly high, especially considering the following points.

First, the computer time is directly related to the degree of convergence required of the routines, and the solutions obtained have a high degree of convergence. A short study was performed to determine the effect of the convergence of the flow field on the pressure solution. For the symmetric, Re = 100 case pressure

solutions were obtained at intermediate time steps 109, 144, and 181 in addition to the final "converged" solution at time step 204. These pressure solutions were compared to see what was the absolute change in pressure between the four times. Between time steps 109 and 144 the pressure changed significantly, with a maximum change of 0.0837 among pressure values with a magnitude around 1.0. Between steps 144 and 181 and between steps 181 and 204, however, the maximum change in pressure dropped to 0.0108 and 0.0018 respectively. Thus, it could conservatively be said that the pressure was within 2% of its final value after time step 144 in the flow field solution. This corresponds to a relative convergence criterion on vorticity of 0.008, rather than the 0.001 used in this study. It also corresponds to a 23% savings in computation time. Whether such a savings could be realized on all cases is not known, but it is strongly felt that a less stringent error criterion could be used without sacrificing significant quality in the solutions.

Second, beyond the question of a convergence criterion there is room for improvement in the convergence times in both the numerical method used and the coding of the method. Although the program was written with speed in mind, there is certainly possible improvement in this respect since it was not written by a programming specialist. Further, the use of quicker but more complex solution methods could lower convergence times. Either or both of these improvements could be made if the convergence speed became a critical factor in the use of the model as a design tool.

The final observation of this section deals with the transient behavior of the numerical solution. Recall that the time dependent vorticity transport equation was used as the basic equation for the flow field. Also recall that the n+1 boundary values on wall vorticity are calculated and used at each time step. Thus, given that the time step is kept small enough to produce accurate solutions, there is no reason that the time dependent behavior of the flow field cannot be predicted as the flow field changes from some initial state to some later state. In fact, by examining several of the intermediate flow solutions for a symmetric, Re = 1000 case it was observed that disturbances were convected through the amplifier in a time like manner.

There are, however, several reservations to acceptance of this as true transient flow. First, the inability of the model to predict the edgetone oscillations indicates that some unsteady, or transient, flow phenomena are not being modeled, as discussed in Section F. Another unresolved problem is what should be the physical interpretation of the initial conditions. For example, does using the symmetric, Re = 100 converged solution as the initial flow distribution and changing the Reynolds number from 100 to 200 correspond to a step increase in the average inflow velocity, U? Although a tempting interpretation, such an interpretation is not completely consistent with the assumptions made in deriving the basic equations. In particular, the non-dimensionalizing assumed a constant U.

Also, boundary conditions for transient response may very well change with time, which is not allowed for in the present formulation. Such problems would have to be resolved before well founded transient results could be calculated.

# CHAPTER V

## SUMMARY, CONCLUSIONS AND RECOMMENDATIONS

### A. Summary

The flow in a simplified laminar fluidic amplifier was numerically and experimentally investigated. The study divided naturally into three major parts.

The first part examined the numerical simulation of a two dimensional fluidic amplifier using finite difference techniques to predict the internal flow distributions under various operating conditions. Distributions for stream function, vorticity, and the corresponding fluid velocities were obtained by solution of finite difference formulations to the time dependent vorticity transport equation and to the stream function equation.

Appropriate boundary conditions were presented and examined for a simplified amplifier geometry. The model was developed such that flows with different Reynolds numbers, receiver outflow rates, and deflections of the inlet flow could be simulated. A variety of solutions were presented as contour plots of the stream function distributions.

The predicted flow patterns, and their changes with varying conditions, are reasonable. The numerical routines are stable, giving convergence for all cases tried, and are relatively easy to use.

They exhibit no dependence on the initial conditions with respect to stability but do have time step limitations.

In the geometry chosen the flow divides into a main flow having a varying width and one or more recirculating vortices which develop on each side of the main flow. For the lower Reynolds numbers considered the main flow diffused as it crossed the cavity and relatively weak recirculation vortices were formed. At the higher Reynolds numbers the main flow remained in a narrow region around the centerline of the amplifier. In each side of the amplifier cavity this narrow central flow drove one main recirculation vortex, which in turn drove one or more smaller vortices. A characteristic of the flow having an important implication on the pressure solutions is that the flow becomes more complex in the splitter region, i.e. the gradients of the flow variables become larger, as the deflection of the main flow increases and/or the outflow from the receivers becomes more unsymmetric.

As formulated the numerical model is capable of predicting transient flows. However, the correct interpretation of the initial flow field as an initial condition for a transient flow needs further clarification. Further, the numerical simulation does not predict the "edgetone" oscillations which were experimentally observed at higher Reynolds numbers. This is probably due to inadequate modeling of the boundary conditions and the use of a grid size too coarse to accurately detect small movements of the edge of the jet.

The second part of the work was the design, construction, and use of a large-scale experimental model of the amplifier considered in the numerical simulation. By injecting dye into water moving through this model at measured flow rates, the flow patterns were made visible and were photographed. This was done for flow rates corresponding to Reynolds numbers of 20, 100, and 290. These photographs were then compared with the appropriate predicted flow fields.

The dye patterns illustrated the dividing and center streamlines for the main flow and the flow in the recirculation regions. Dye patterns obtained for the flow having a Reynolds number of 100 were particularly clear and gave good agreement when compared with the predicted flow patterns.

The third part of this work was the computation of pressure distributions for each of the numerical flow field solutions. This involved numerical solution of a Poisson type partial differential equation with Neumann boundary conditions. Problems with compatibility between the calculated pressure gradients at the boundaries and the forcing function of the Poisson type equation were discovered. This inconsistency problem was examined and a method was presented for compensating for the inconsistency. An appropriate convergence criterion was considered. Converged pressure solutions were graphically presented as plots of lines of constant pressure. Estimates of the accuracy and possible shortcomings of the predicted pressures were presented. The pressure results were combined with the flow solutions to generate characteristic design curves.

B. Conclusions

Based on the present work certain conclusions can be drawn with regard to the flow field, the pressure field, and their simulation. These are:

1. The finite difference techniques used in this study are a viable means for modeling the steady state fluid flow in laminar fluidic devices having a relatively simple geometric design. Therefore, this work constitutes a solid basis for further work in finite difference modeling of fluidic amplifiers.
2. The experimental apparatus built in this study allows visualization of the flow patterns in large scale amplifier models. The experimental streamline patterns qualitatively confirm the numerical streamline predictions.
3. The formulation of the pressure problem as a Poisson type partial differential equation with Neumann boundary conditions is insufficient to completely specify the problem and to guarantee adequate numerical modeling of the physical process. Also needed, and often neglected in engineering formulations of the problem, is a statement of the consistency requirement.
4. The finite differencing necessary to obtain the boundary conditions and the forcing function ($s_{ij}$ of Eq.(2.27))

can lead quite easily to violation of the consistency requirement. Although the differencing is done correctly the actual magnitudes produced can cause the violation due to truncation error. Further, care must be taken with the differencing formulas selected for the $\nabla^2 P$ terms in order to insure consistency. Consistency of this differencing can be assured by the methods discussed in Chapter II, Section D. These methods will also give the actual magnitude of any inconsistency due to truncation error. The inconsistency problem can be allowed for as discussed in Chapter IV, Section D. The resulting pressure distributions appear acceptable for the symmetric case but the accuracy seems to deteriorate as the flows become unsymmetric. This is probably due to resolution problems in the splitter region where for unsymmetric flows the gradients become steep and the number of nodes is small. It should be emphasized that use of the alternative line integration method would suffer from the same resolution problems that lead to inconsistency in the Poisson pressure formulation.

5. Problems with the pressure solution produce a restriction on application, at this point in time, of the mathematical model in generating amplifier characteristic curves. Therefore, the use of the model as a design tool hinges on future refinement of the pressure solution.

6. Assuming the pressure problem can be solved, another consideration in use of the model is the cost of obtaining solutions. The computer time required to obtain a set of solutions, as discussed in Chapter IV, Section G, is not excessive, but it is not trivial either. A characteristic curve was generated for Reynolds number of 100 in 6768 seconds using the CDC 6600 system at The University of Texas at Austin.

## C. Recommendations

The most pressing need in continuation of this work is to solve the pressure difficulties encountered. Based on the work already done, it appears that insufficient accuracy in the difference approximations for certain regions of the flow field is the primary cause. Therefore, the following recommendations are made.

1. The next step in this work should be an effort to obtain higher resolution in these regions. This could be done by either the use of a grid with variable mesh size or by use of some type of grid transformation. Either approach could be designed to give a large number of nodes in the regions around the splitter and the amplifier inlet where gradients are large.
2. The above step should be implemented in two stages. The first should be examination of the chosen approach on a relatively simple flow problem. This flow should not be

that of a fluidic amplifier and should have a very simple geometry. The purpose here would be to reduce the variables which might effect the pressure and flow solutions. The effects of the grid changes on the pressure solutions, particularly on the magnitude of the inconsistency, could then be more easily examined. At the same time estimates could be obtained for what effects the changes would produce on the flow field solution. Naturally, a flow case for which a pressure solution is available for comparison to the numerical results would be desirable. The second stage would be implementing the refinement on the full amplifier model. Hopefully the programming complexity would be reduced by the experience gained in the first stage.

3. In conjunction with further work on the pressure solution it is recommended that pressure values be obtained experimentally for verifying the numerical predictions.
4. Once the pressure problem is resolved it is recommended that the potential capabilities of the model be further explored. The abilities to vary Reynolds number, outflow rates, and inlet deflection have been examined. The next step would be to examine the effects of varying the geometry of the amplifier. This might include varying the receiver widths, the receiver angles (presently 45°), or the ratio of inlet to splitter distance. Finally, the

geometry and flow of the control jets should be added to the model.

5. It is recommended that the use of the model to predict transient response be explored. In particular, interpretation of initial conditions needs to be examined. Also needed is the development of boundary conditions which would allow edgetone oscillations to exist in the flow.
6. Finally, it is suggested that boundary conditions and/or iterative procedures be developed which would allow modeling of vented amplifiers. As discussed in Chapter II such flows are complicated by the vent flows being unknown in either direction or magnitude. Unfortunately no recommendation can be made as to what boundary conditions might be used to adequately model the vented amplifier.

# APPENDIX

## Differencing for Boundary Conditions and Forcing Function for Pressure Solution

As discussed in Chapter II, in the calculations for the pressure distribution values must be obtained for $\left.\frac{\delta P}{\delta y}\right|_{i,j}$ and $\left.\frac{\delta P}{\delta x}\right|_{i,j}$ on the boundaries and for $s_{i,j}$ at all nodes in the region of interest. Boundary gradients are obtained through appropriate differencing of Eq.(2.12). Likewise, $s_{i,j}$ values are obtained by differencing of the relation given in Eq.(2.29).

Selection of appropriate difference expressions is complicated by the fact that expressions are needed for wall nodes, where differencing must be one sided, and for sharp corners, where vorticity values are discontinuous. At these points several possible choices for difference equations were available. Various combinations were tried in an effort to reduce the inconsistency of the pressure formulation. The resulting difference equations are presented in Table A.1.

Table A.1. Difference Expressions for $\frac{\delta P}{\delta x}$, $\frac{\delta P}{\delta y}$, and $s_{i,j}$

Note: Asterisk denotes multiplication

| Location | Difference Equation |
|---|---|
| **Left boundary** | |
| $i = 11,\ j = 1$ | $\frac{\delta P}{\delta x} = \frac{1}{Re} * \frac{(-\zeta_{11,3} + 4\,\zeta_{11,2} - 3\,\zeta_{11,1})}{2\Delta y}$ |
| | $\frac{\delta P}{\delta y} = \frac{-1}{Re} * \frac{(\zeta_{12,1} - \zeta_{10,1})}{2\Delta x}$ |
| $i = 11,$ $2 \leq j \leq 40$ | $\frac{\delta P}{\delta x} = \frac{1}{Re} * \frac{(\zeta_{11,j+1} - \zeta_{11,j-1})}{2\Delta y} - u_{11,j} * \frac{(u_{12,j} - u_{10,j})}{2\Delta x} - v_{11,j} * \frac{(\psi_{11,j+1} + \psi_{11,j-1} - 2\,\psi_{11,j})}{\Delta y^2}$ |
| $i = 11,\ j = 41$ | $\frac{\delta P}{\delta x} = \frac{-1}{Re} * \frac{(-\zeta_{11,39} + 4\,\zeta_{11,40} - 3\,\zeta_{11,41})}{2\Delta y}$ |
| | $\frac{\delta P}{\delta y} = \frac{-1}{Re} * \frac{(\zeta_{12,41} - \zeta_{10,41})}{2\Delta x}$ |
| **Right boundary** | |
| $i = 31,\ j = 1$ | $\frac{\delta P}{\delta x} = \frac{1}{Re} * \frac{(-\zeta_{31,3} + 4\,\zeta_{31,2} - 3\,\zeta_{31,1})}{2\Delta y}$ |
| | $\frac{\delta P}{\delta y} = \frac{-1}{Re} * \frac{(\zeta_{32,1} - \zeta_{30,1})}{2\Delta x}$ |

Table A.2. (continued)

| Location | Difference Equation |
|---|---|
| $i = 31$, $2 \leq j < 40$ | $\frac{\delta P}{\delta x} = \frac{1}{Re} * \frac{(\zeta_{31,j+1} - \zeta_{31,j-1})}{2\Delta y} - u_{31,j} * \frac{(u_{32,j} - u_{30,j})}{2\Delta x} - v_{31,j} * \frac{(\psi_{31,j+1} + \psi_{31,j-1} - 2\psi_{11,j})}{\Delta y^2}$ |
| $i = 31$, $j = 41$ | $\frac{\delta P}{\delta x} = \frac{-1}{Re} * \frac{(-\zeta_{31,39} + 4\zeta_{31,40} - 3\zeta_{31,41})}{2\Delta y}$ |
| | $\frac{\delta P}{\delta y} = \frac{-1}{Re} * \frac{(\zeta_{32,41} - \zeta_{30,41})}{2\Delta x}$ |
| Lower cavity boundary | |
| $12 \leq i \leq 18$, $24 \leq i \leq 30$, $j = 1$ | $\frac{\delta P}{\delta y} \approx \frac{-1}{Re} * \frac{(\zeta_{i+1,1} - \zeta_{i-1,1})}{2\Delta x}$ |
| $i = 19$, $j = 1$ | $\frac{\delta P}{\delta y} \approx \frac{-1}{Re} * \frac{(-\zeta_{21,1} + 4\zeta_{20,1} - 3\zeta_{19,1})}{2\Delta x}$ |
| $i = 20$, $j = 1$ | $\frac{\delta P}{\delta y} \approx \frac{-1}{Re} * \frac{(\zeta_{21,1} - \zeta_{19,1})}{2\Delta x} + u_{20,1} * \frac{(\psi_{21,1} + \psi_{19,1} - 2\psi_{20,1})}{\Delta x^2} + v_{20,1} * \frac{(-2u_{19,1} - 3u_{20,1} + 6u_{21,1} - u_{22,1})}{6\Delta x}$ |

Table A.2. (continued)

| Location | Difference Equation |
|---|---|
| $i = 21,\ j = 1$ | $\frac{\delta P}{\delta y} = \frac{-1}{Re} * \frac{(\zeta_{22,1} - \zeta_{20,1})}{2\Delta x} + u_{21,1} * \frac{(\psi_{22,1} + \psi_{20,1} - 2\psi_{21,1})}{\Delta x^2} + v_{21,1} * \frac{(u_{19,1} - 6u_{20,1} + 3u_{21,1} + 2u_{22,1})}{6\Delta x}$ |
| $i = 22,\ j = 1$ | $\frac{\delta P}{\delta y} = \frac{-1}{Re} * \frac{(\zeta_{23,1} - \zeta_{21,1})}{2\Delta x} + u_{22,1} * \frac{(\psi_{23,1} + \psi_{21,1} - 2\psi_{22,1})}{\Delta x^2} + v_{21,1} * \frac{(-2u_{19,1} + 9u_{20,1} - 18u_{21,1} + 11u_{22,1})}{6\Delta x}$ |
| $i = 23,\ j = 1$ | $\frac{\delta P}{\delta y} = \frac{1}{Re} \frac{(-\zeta_{21,1} + 4\zeta_{22,1} - 3\zeta_{23,1})}{2\Delta x}$ |
| Upper Cavity Boundary | |
| $12 \leq i \leq 16$, $26 \leq i \leq 30$, $j = 41$ | $\frac{\delta P}{\delta y} = \frac{-1}{Re} * \frac{(\zeta_{i+1,41} - \zeta_{i-1,41})}{2\Delta x}$ |
| $i = 17,\ j = 41$ | $\zeta^A_{17,41} = \frac{1}{2\Delta y^2} * (-7\psi_{17,41} + 8\psi_{17,40} - \psi_{17,39})$ |
| | $\left.\frac{\delta P}{\delta x}\right\|_- = \frac{-1}{Re} * \frac{(-\zeta_{17,39} + 4\zeta_{17,40} - 3\zeta^A_{17,41})}{2\Delta y}$ |

Table A.2. (continued)

| Location | Difference Equation |
|---|---|
| | $\left.\frac{\delta P}{\delta y}\right\|_{-} = \frac{1}{Re} * \frac{(-\zeta_{15,41} + 4\zeta_{16,41} - 3\zeta^{A}_{17,41})}{2\Delta x}$ |
| | $\zeta^{B}_{17,41} = \left(\frac{2.0}{\Delta x^2}\right) * (\psi_{18,41} + \psi_{17,42} - 2\psi_{17,41})$ |
| | $\left.\frac{\delta P}{\delta x}\right\|_{+} = \frac{1}{Re} * \frac{(-\zeta_{17,43} + 4\zeta_{17,42} - 3\zeta^{B}_{17,41})}{2\Delta y}$ |
| | $\left.\frac{\delta P}{\delta y}\right\|_{+} = \frac{-1}{Re} * \frac{(-\zeta_{19,41} + 4\zeta_{18,41} - 3\zeta^{B}_{17,41})}{2\Delta x}$ |
| i = 21, j = 41 | $\zeta^{A}_{21,41} = \frac{2}{\Delta x^2} * (\psi_{20,41} + \psi_{21,40} - 2\psi_{21,41})$ |
| | $\left.\frac{\delta P}{\delta x}\right\|_{-} = \frac{-1}{Re} * \frac{(-\zeta_{21,39} + 4\zeta_{21,40} - 3\zeta^{A}_{21,41})}{2\Delta y}$ |
| | $\left.\frac{\delta P}{\delta y}\right\|_{-} = 2 * \left(\frac{\psi_{20,40} - \psi_{22,40}}{2\Delta x}\right)^2$ |
| | $\zeta^{B}_{21,41} = \frac{2}{\Delta x^2} * (\psi_{22,41} + \psi_{21,40} - 2\psi_{21,41})$ |
| | $\left.\frac{\delta P}{\delta x}\right\|_{+} = \frac{-1}{Re} * \frac{(-\zeta_{21,39} + 4\zeta_{21,40} - 3\zeta^{B}_{21,41})}{2\Delta y}$ |
| i = 25, j = 41 | $\zeta^{A}_{25,41} = \frac{2}{\Delta x^2} * (\psi_{24,41} + \psi_{25,42} - 2\psi_{25,41})$ |
| | $\left.\frac{\delta P}{\delta y}\right\|_{+} = \frac{1}{Re} * \frac{(-\zeta_{23,41} + 4\zeta_{24,41} - 3\zeta^{A}_{25,41})}{2\Delta x}$ |

Table A.2. (continued)

| Location | Difference Equation |
|---|---|

$$\left.\frac{\delta P}{\delta x}\right|_{-} = \frac{1}{Re} * \frac{(-\zeta_{25,43} + 4\,\zeta_{25,42} - 3\,\zeta^{A}_{25,41})}{2\Delta y}$$

$$\zeta^{B}_{25,41} = \frac{1}{2\Delta y^{2}} * (-7\,\psi_{25,41} + 8\,\psi_{25,40} - \psi_{25,39})$$

$$\left.\frac{\delta P}{\delta y}\right|_{-} = \frac{-1}{Re} * \frac{(-\zeta_{27,41} + 4\,\zeta_{26,41} - 3\,\zeta^{B}_{25,41})}{2\Delta x}$$

$$\left.\frac{\delta P}{\delta x}\right|_{+} = \frac{-1}{Re} * \frac{(-\zeta_{25,39} + 4\,\zeta_{25,40} - 3\,\zeta^{B}_{25,41})}{2\Delta y}$$

Left receiver

$42 \leq j \leq 44$

w = i value for wall node

Left wall

$$\frac{\delta P}{\delta x} = \frac{1}{Re} * \frac{(-\zeta_{w,j+2} + 4\,\zeta_{w,j+1} - 3\,\zeta_{w,j})}{2\Delta y}$$

$$\frac{\delta P}{\delta y} = \frac{-1}{Re} * \frac{(-\zeta_{w+2,j} + 4\,\zeta_{w+1,j} - 3\,\zeta_{w,j})}{2\Delta x}$$

Right wall

$$\frac{\delta P}{\delta x} = \frac{-1}{Re} * \frac{(-\zeta_{w,j-2} + 4\,\zeta_{w,j-1} - 3\,\zeta_{w,j})}{2\Delta y}$$

$$\frac{\delta P}{\delta y} = \frac{1}{Re} * \frac{(-\zeta_{w-2,j} + 4\,\zeta_{w-1,j} - 3\,\zeta_{w,j})}{2\Delta x}$$

$45 \leq j \leq 56$

Left wall

$$\frac{\delta P}{\delta x} = -\frac{\delta P}{\delta y} = \frac{-1}{Re} * \frac{(\zeta_{w,j} - \zeta_{w+1,j+1})}{2\Delta x}$$

Table A.2. (continued)

| Location | Difference Equation |
|---|---|
| Right wall | $\frac{\delta P}{\delta x} = -\frac{\delta P}{\delta y} = \frac{-1}{Re} * \frac{(\zeta_{w-1,j-1} - \zeta_{w,j})}{2\Delta x}$ |
| $j = 57,\ i = 2$ | $\left.\frac{\delta P}{\delta x}\right\|_{2,57} = \left.\frac{\delta P}{\delta x}\right\|_{2,56}$ |
| | $\left.\frac{\delta P}{\delta y}\right\|_{2,57} = \left.\frac{\delta P}{\delta y}\right\|_{2,56}$ |
| $j = 57,$ $3 \leq i \leq 4$ | $\left.\frac{\delta P}{\delta y}\right\|_{i,57} = \left.\frac{\delta P}{\delta y}\right\|_{2,57}$ |
| $j = 57,\ i = 4$ | $\left.\frac{\delta P}{\delta x}\right\|_{4,57} = \left.\frac{\delta P}{\delta x}\right\|_{5,56}$ |
| | $\left.\frac{\delta P}{\delta y}\right\|_{4,57} = \left.\frac{\delta P}{\delta y}\right\|_{5,56}$ |
| Right receiver | |
| $42 \leq j \leq 44$<br>w = i value for wall node | |
| Left wall | $\frac{\delta P}{\delta x} = \frac{-1}{Re} * \frac{(-\zeta_{w,j-2} + 4\zeta_{w,j-1} - 3\zeta_{w,j})}{2\Delta y}$ |
| | $\frac{\delta P}{\delta y} = \frac{-1}{Re} * \frac{(-\zeta_{w+2,j} + 4\zeta_{w+1,j} - 3\zeta_{w,j})}{2\Delta x}$ |
| Right wall | $\frac{\delta P}{\delta x} = \frac{1}{Re} * \frac{(-\zeta_{w,j+2} + 4\zeta_{w,j+1} - 3\zeta_{w,j})}{2\Delta y}$ |

Table A.2. (continued)

| Location | Difference Equation |
|---|---|
| | $\frac{\delta P}{\delta y} = \frac{1}{Re} * \frac{(-\zeta_{w-2,j} + 4\zeta_{w-1,j} - 3\zeta_{w,j})}{2\Delta x}$ |
| $45 \leq j \leq 56$ | |
| Left wall | $\frac{\delta P}{\delta x} = \frac{\delta P}{\delta y} = \frac{1}{Re} * \frac{(\zeta_{w,j} - \zeta_{w+1,j-1})}{2\Delta x}$ |
| Right wall | $\frac{\delta P}{\delta x} = \frac{\delta P}{\delta y} = \frac{1}{Re} * \frac{(\zeta_{w-1,j+1} - \zeta_{w,j})}{2\Delta x}$ |
| $j = 57,\ i = 37$ | $\left.\frac{\delta P}{\delta x}\right\|_{37,57} = \left.\frac{\delta P}{\delta x}\right\|_{36,56}$ |
| | $\left.\frac{\delta P}{\delta y}\right\|_{37,57} = \left.\frac{\delta P}{\delta y}\right\|_{36,56}$ |
| $j = 57,$ $38 \leq i \leq 39$ | $\left.\frac{\delta P}{\delta y}\right\|_{i,57} = \left.\frac{\delta P}{\delta y}\right\|_{37,57}$ |
| $j = 57,\ i = 40$ | $\left.\frac{\delta P}{\delta x}\right\|_{40,57} = \left.\frac{\delta P}{\delta x}\right\|_{40,56}$ |
| | $\left.\frac{\delta P}{\delta y}\right\|_{40,57} = \left.\frac{\delta P}{\delta y}\right\|_{40,56}$ |

Table A.2. (continued)

| Location | Difference Equation |
|---|---|
| For all wall points | $s_{i,j} = 0$ |
| $20 \leq i \leq 22$, $j = 1$ | $s_{i,j} = 2.0 * \left[ \frac{(\psi_{i+1,1} + \psi_{i-1,1} - 2\psi_{i,1})}{\Delta x^2} * \frac{1}{\Delta y^2} * (2\psi_{i,1} - 5\psi_{i,2} + 4\psi_{i,3} - \psi_{i,4}) - \left( \frac{u_{i+1,1} - u_{i-1,1}}{2\Delta x} \right)^2 \right]$ |
| $11 \leq i \leq 31$, $2 \leq j \leq 40$ | $s_{i,j} = 2.0 * \left[ \frac{(\psi_{i+1,j} + \psi_{i-1,j} - 2\psi_{i,j})}{\Delta x^2} * \frac{(\psi_{i,j+1} + \psi_{i,j-1} - 2\psi_{i,j})}{\Delta y^2} - \left( \frac{u_{i+1,j} - u_{i-1,j}}{2\Delta x} \right)^2 \right]$ |
| All non-wall points<br>$41 \leq j \leq 56$<br>Left receiver | $s_{i,j} = 2.0 * \left[ \frac{(\psi_{i-1,j+1} + \psi_{i+1,j-1} - 2\psi_{i,j})}{2\Delta x^2} * \left( \zeta_{i,j} - \frac{(\psi_{i-1,j+1} + \psi_{i+1,j-1} - 2\psi_{i,j})}{2\Delta x^2} \right) - \left( \frac{(\psi_{i-1,j} - \psi_{i,j-1}) - (\psi_{i,j+1} - \psi_{i+1,j})}{2\Delta x^2} \right)^2 \right]$ |

Table A.2. (continued)

| Location | Difference Equation |
|---|---|
| Right receiver | $s_{i,j} = 2.0 * \left[ \frac{(\psi_{i+1,j+1} + \psi_{i-1,j-1} - 2\psi_{i,j})}{2\Delta x^2} * \left( \zeta_{i,j} - \frac{(\psi_{i+1,j+1} + \psi_{i-1,j-1} - 2\psi_{i,j})}{2\Delta x^2} \right) - \left( \frac{(\psi_{i,j+1} - \psi_{i-1,j}) - (\psi_{i+1,j} - \psi_{i,j-1})}{2\Delta x^2} \right)^2 \right]$ |
| Left receiver | |
| $j = 57$ | $s_{i,57} = s_{i+1,56}$ |
| Right receiver | |
| $j = 57$ | $s_{i,57} = s_{i-1,56}$ |

# BIBLIOGRAPHY


1. Arden, Bruce W., and Astill, Kenneth N., Numerical Algorithms: Origins and Applications, Addison-Wesley Publishing Company, Inc., 1970.

2. Arpaci, Vedat S., Conduction Heat Transfer, Addison-Wesley Publishing Company, Inc., 1966.

3. Belsterling, Charles A., Fluidic Systems Design, John Wiley and Sons, Inc., 1971.

4. Brackenridge, J. Bruce, "Transverse Oscillations of a Liquid Jet. I," Journal of the Acoustical Society of America, Vol. 32, No. 10, October 1960, pp. 1237-1242.

5. Brackenridge, J. Bruce, and Nyborg, Wesley L., "Transverse Oscillations of a Liquid Jet. II," Journal of the Acoustical Society of America, Vol. 33, No. 8, August 1961, pp. 1078-1084.

6. Briley, W. Roger, "A Numerical Study of Laminar Separation Bubbles Using the Navier-Stokes Equations," United Aircraft Research Laboratories, Report J 11D614-1, July 1970.

7. Douglas, Jim, "On the Numerical Integration of $\partial^2 u/\partial x^2 + \partial^2 u/\partial y^2 = \partial u/\partial t$ by Implicit Methods," J. Soc. Indust. Appl. Math., Vol. 3, No. 1, March 1955, pp. 42-65.

8. Fanning, A. E., and Mueller, T. J., "On the Solution of a Neumann Problem for an Inhomogeneous Laplace Equation," Journal of Computational Physics, Vol. 13, 1973, pp. 450-454.

9. Han, L. S., "Hydrodynamic Entrance Lengths for Incompressible Laminar Flow in Rectangular Ducts," Transactions ASME, Journal of Applied Mechanics, Vol. 27, Series E, No. 3, September 1960, pp. 403-409.

10. Healey, A. J., "Guest Editorial," Transactions ASME, Journal of Dynamic Systems, Measurement, and Control, Vol. 95, Series G, No. 2, June 1973, pp. 105-107.

11. Healey, A. J., and Reynolds, W. J., "Static Output Characteristics of a Beam Deflection Fluid Amplifier," Technical Report, The University of Texas at Austin, Dept. of Mech. Engineering, December 1972.

12. Healey, A. J., and Shipp, E. M., "Vent Length Effects on a Proportional Fluid Amplifier," Technical Report, The University of Texas at Austin, Dept. of Mech. Engineering, September 1973.

13. Manion, Francis M., and Mon, George, "Design and Staging of Laminar Proportional Amplifiers," Fluerics Report 33, Harry Diamond Laboratories, Washington, D.C., September 1972.

14. Masliyah, Jacob H., and Epstein, Norman, "Numerical Study of Steady Flow Past Spheroids," J. Fluid Mech., Vol. 44, Part 3, 1970, pp. 493-512.

15. Mitchell, A. R., Computational Methods in Partial Differential Equations, J. Wiley and Sons, Inc., 1969.

16. O'Brien, R. A., "Commercial Applications of Fluidics," Transactions ASME, Journal of Dynamic Systems, Measurement, and Control, Vol. 95, Series G, No. 2, June 1973, pp. 108-110.

17. Peaceman, D. W., and Rachford, H. H., "The Numerical Solution of Parabolic and Elliptic Differential Equations," J. Soc. Indust. Appl. Math., Vol. 3, No. 1, March 1955, pp. 28-41.

18. Pearson, Carl E., "A Computational Method for Viscous Flow Problems," J. Fluid Mech., Vol. 21, Part 4, 1965, pp. 611-622.

19. Richards, C. G., and Chavez, S. P., "Numerical Study of the Coanda Effect," Technical Report No. AFWL-TR-69-141, Air Force Weapons Laboratory, Kirtland AFB, NM, December 1969.

20. Roache, Patrick J., Computational Fluid Dynamics, Hermosa Publishers, 1972.

21. Roache, Patrick J., "On Artificial Viscosity," Journal of Computational Physics, Vol. 10, 1972, pp. 169-184.

22. Rockwell, D. O., "Transverse Oscillations of a Jet in a Jet-Splitter System," Transactions ASME, Journal of Basic Engineering, Vol. 94, Series D, No. 3, September 1972, pp. 675-681.

23. Runchal, A. K., Spalding, D. B., and Wolfshtein, M., "Numerical Solution of the Elliptic Equations for Transport of Vorticity, Heat, and Matter in Two-Dimensional Flow," High-Speed Computing in Fluid Dynamics, The Physics of Fluids Supplement II, 1969, pp. 21-28.

24. Sarpkaya, Turgut, "On the Art of Advancing the Science of Fluidics," Transactions ASME, Journal of Dynamic Systems, Measurement, and Control, Vol. 95, Series G, No. 2, June 1973, pp. 110-113.

25. Schlichting, Hermann, Boundary Layer Theory, McGraw-Hill Book Co., New York, N.Y., 1968.

26. Schraub, F. A., Kline, S. J., Henry, J., Runstadler, P. W., Littell, A., "Use of Hydrogen Bubbles for Quantitative Determination of Time-Dependent Velocity Fields in Low-Speed Water Flows," Transactions ASME, Journal of Basic Engineering, Vol. 87, Series D, No. 2, June 1965, pp. 429-444.

27. Shames, Irving H., Mechanics of Fluids, McGraw-Hill Book Co., Inc., 1962.

28. Thoman, D., and Szewczyk, A. A., "Time Dependent Viscous Flow Over a Circular Cylinder," The Physics of Fluids Supplement II, 1969, pp. 76-87.

29. Young, D. M., Iterative Solution of Large Linear Systems, Academic Press, 1971.

30. Young, David M., and Gregory, Robert Todd, A Survey of Numerical Mathematics, Vol. II, Addison-Wesley Publishing Company, Inc., 1973.